Washington University in St. Louis
Washington University Open Scholarship

All Theses and Dissertations (ETDs)

Winter 1-1-2012

Three-Dimensional Photoacoustic Computed Tomography: Imaging Models and Reconstruction Algorithms

Kun Wang
Washington University in St. Louis

Follow this and additional works at: https://openscholarship.wustl.edu/etd

Recommended Citation

Wang, Kun, "Three-Dimensional Photoacoustic Computed Tomography: Imaging Models and Reconstruction Algorithms" (2012). *All Theses and Dissertations (ETDs)*. 1024.
https://openscholarship.wustl.edu/etd/1024

This Dissertation is brought to you for free and open access by Washington University Open Scholarship. It has been accepted for inclusion in All Theses and Dissertations (ETDs) by an authorized administrator of Washington University Open Scholarship. For more information, please contact digital@wumail.wustl.edu.

Washington University in St. Louis

School of Engineering and Applied Science

Department of Biomedical Engineering

Dissertation Examination Committee:
Mark Anastasio, Chair
Joseph Culver
James Miller
Robert Pless
Lihong Wang
Lan Yang

Three-Dimensional Photoacoustic Computed Tomography: Imaging Models and Reconstruction Algorithms

by

Kun Wang

A dissertation presented to the Graduate School of Arts & Sciences
in partial fulfillment of the requirements for the degree of

DOCTOR OF PHILOSOPHY

December 2012
Saint Louis, Missouri

copyright by

Kun Wang

2012

Contents

List of Figures

List of Tables

Acknowledgments

I would like to thank my advisor Professor Mark A. Anastasio for his mentorship and friendship. His high standard of scientific excellence has shaped me as a good researcher in the field of medical imaging.

I would like to thank all my committee members for their help, especially Professor Lihong V. Wang. I benefited greatly from many deep discussions with him and his researchers. I would like to thank Dr. Alexander A. Oraevsky, Dr. Sergey A. Ermilov and Mr. Richard Su, from TomoWave Laboratories, Houston, TX, for building an amazing system on which I have been able to test my algorithms. I would also like to thank Professor Xiaochuan Pan and Professor Emil Y. Sidky for their stimulating conversations that inspired the work in Chapter 5.

I would like to thank everyone who taught and helped me during my studies from Chicago to St. Louis, including Professor Vincent Turitto, Professor Miles Wernick, Professor Frank Yin, Ms. Catherine D'Amico and Ms. Karen Teasdake.

I appreciate my former labmates Dr. Jin Zhang, Dr. Daxin Shi and Dr. Yin Huang for their unreserved help when I started the journey in Dr. Anastasio's group. I thank Dr. Robert W. Schoonover, Mr. Chao Huang, Dr. Jun Xia, Dr. Xiaofeng Niu, Mr. Qiaofeng Xu, and Mr. Wenyuan Qi for their many discussions and collaborations.

I am most grateful for the love and support of my parents and my sister during my time in graduate school and through my whole life.

Kun Wang

Washington University in Saint Louis
December 2012

ABSTRACT OF THE DISSERTATION

Three-Dimensional Photoacoustic Computed Tomography: Imaging Models and Reconstruction Algorithms

by

Kun Wang

DOCTOR OF PHILOSOPHY in Biomedical Engineering

Washington University in St. Louis, December 2012

Research Advisor: Professor Mark Anastasio

Photoacoustic computed tomography (PACT), also known as optoacoustic tomography, is a rapidly emerging imaging modality that holds great promise for a wide range of biomedical imaging applications. Much effort has been devoted to the investigation of imaging physics and the optimization of experimental designs. Meanwhile, a variety of image reconstruction algorithms have been developed for the purpose of computed tomography. Most of these algorithms assume full knowledge of the acoustic pressure function on a measurement surface that either encloses the object or extends to infinity, which poses many difficulties for practical applications. To overcome these limitations, iterative image reconstruction algorithms have been actively investigated. However, little work has been conducted on imaging models that incorporate the characteristics of data acquisition systems. Moreover, when applying to experimental data, most studies simplify the inherent three-dimensional wave propagation as two-dimensional imaging models by introducing heuristic assumptions on the

transducer responses and/or the object structures. One important reason is because three-dimensional image reconstruction is computationally burdensome. The inaccurate imaging models severely limit the performance of iterative image reconstruction algorithms in practice. In the dissertation, we propose a framework to construct imaging models that incorporate the characteristics of ultrasonic transducers. Based on the imaging models, we systematically investigate various iterative image reconstruction algorithms, including advanced algorithms that employ total variation-norm regularization. In order to accelerate three-dimensional image reconstruction, we develop parallel implementations on graphic processing units. In addition, we derive a fast Fourier-transform based analytical image reconstruction formula. By use of iterative image reconstruction algorithms based on the proposed imaging models, PACT imaging scanners can have a compact size while maintaining high spatial resolution. The research demonstrates, for the first time, the feasibility and advantages of iterative image reconstruction algorithms in three-dimensional PACT.

Chapter 1

Introduction

The goals of this dissertation are to develop accurate imaging models and to investigate advanced image reconstruction algorithms for photoacoustic computed tomography (PACT). Two features distinguish this dissertation from previous studies of PACT image reconstruction: (i) a continuous-to-discrete (C-D) imaging model is introduced to describe practical PACT imaging systems; and (ii) all reconstruction algorithms are developed in the context of wave propagation in three-dimensional (3D) space. These features not only lead to successful applications of advanced image reconstruction algorithms to experimentally measured data, but also establish a framework of developing more accurate imaging models to further facilitate PACT image reconstruction. In this chapter, the motivations of this dissertation are presented.

1.1 Background and Motivation

Photoacoustic imaging (PAI) is a rapidly emerging imaging technique that holds great promise for biomedical applications [68, 112, 51]. PAI is a hybrid technique that exploits the photoacoustic effect for signal generation. It seeks to combine the high optical-absorption contrast of tissues with the high spatial resolution of ultrasonic methods. Accordingly, PAI can be viewed either as an ultrasound mediated optical imaging modality or an ultrasound modality that exploits optical-absorption image contrast [119]. Since the 1990s there have been numerous fundamental studies of photoacoustic imaging of biological tissues [79, 114, 51, 83, 80, 65, 30], and the development of PAI continues to progress at a tremendous rate [119, 68, 50, 51, 48, 38, 54, 122, 27].

The image formation principles are briefly reviewed as follows. When a short laser pulse is used to irradiate an object (i.e., biological tissues), the photoacoustic effect results in the emission of acoustic signals that can be measured outside the object by use of wide-band ultrasonic transducers. The objective of PAI is to produce an image that represents a map of the spatially variant absorbed optical energy density of the tissues from knowledge of the measured acoustic signals. To accomplish this, two forms of implementations have been proposed: direct imaging and computed tomography [119, 112]. The direct imaging method usually employs focused ultrasonic transuducers to detect photoacoustic wavefield along a scanning trajectory and directly forms images by stacking the measured signals in space according to the scanning trajectory. Dark-field confocal photoacoustic microscopy (PAM) is an extraordinary successful example of the direct imaging implementation [66, 131]. Alternatively, the computed tomography method often employs unfocused ultrasonic transducers to sense the photoacoustic wavefield and forms the image of the absorbed optical energy density distribution with the aid of reconstruction algorithms. In the literature, this implementation is often referred to as photoacoustic computed tomography (PACT) [113, 122], optoacoustic tomography (OAT) [84, 68, 15], or thermoacoustic tomography (TAT) if microwave energy is employed instead of optical energy [51, 121]. This dissertation is devoted to the modeling and image reconstruction algorithm development for the purpose of computed tomography. However, the modeling techniques also apply to direct imaging to guide the development of post-processing methods.

From a physical perspective, the image reconstruction problem in PACT can be interpreted as an inverse source problem [5]. A variety of analytic image reconstruction algorithms have been developed for PACT with canonical measurement apertures assuming point-like ultrasound transducers [119, 121, 34, 122, 35, 55, 56, 94, 41] and integrating detectors [38, 18, 19, 128]. All known analytic reconstruction algorithms that are mathematically exact and numerically stable require complete knowledge of the photoacoustic wavefield on a measurement aperture that either encloses the entire object or extends to infinity. In many potential applications of PACT, it is infeasible to acquire such measurement data. Because of this, iterative, or more generally, optimization-based, reconstruction algorithms for PACT are being developed actively [84, 86, 1, 2, 127, 133, 89, 27, 105, 37, 44, 17, 16, 110] that provide the opportunity for accurate image reconstruction from incomplete measurement

data. Iterative reconstruction algorithms also allow for accurate modeling of physical non-idealities in the data such as those introduced by acoustic inhomogeneity and attenuation, or the response of the imaging system.

1.2 Overview of the Dissertation

The dissertation opens with a discussion of the imaging models of PACT in Chapter 2. The purpose of this chapter is to place the specialized field of PACT within the broader context of imaging science.

Chapter 3 derives a novel Fourier transform-based image reconstruction formula for PACT. This reconstruction formula yields a straightforward numerical implementation that is stable and is two orders of magnitude more computationally efficient than 3D filtered backprojection algorithms.

Chapter 4 proposes a framework to construct discrete-to-discrete PACT imaging models that incorporate the characteristics of ultrasonic transducers. Based on the discrete-to-discrete imaging models, the transducer diffraction effects can be compensated for by use of iterative image reconstruction algorithms.

Chapter 5 investigates two iterative image reconstruction algorithms in PACT. This chapter highlights the regularization strategy that employs a total-variation-norm of the images as the objective penalty. This regularization strategy can potentially reduce the amount of data required with minimal sacrifice in image quality.

Chapter 6 discribes the parallel implementations of the filtered backprojection and iterative image reconstruction algorithms. These parallelization strategies are designed for the use of graphics processing units and are useful for a wide range of PACT image reconstruction algorithms.

A summary of the dissertation and closing remarks are presented in Chapter 7.

Chapter 2

Photoacoustic Computed Tomography Imaging Models

2.1 PACT Imaging Models in Their Continuous Forms

A schematic of a general PACT imaging geometry is shown in Fig. 2.1. A short laser pulse is employed to irradiate an object and the thermoacoustic effect results in the generation of a pressure wavefield $p(\mathbf{r}, t)$. The pressure wavefield propagates out of the object and is measured by use of ultrasonic transducers located on a measurement aperture $S \subset \mathbb{R}^3$, which is a two-dimensional (2D) surface that partially or completely surrounds the object. The coordinate $\mathbf{r}^s \in S$ will denote a particular transducer location. When the object possesses

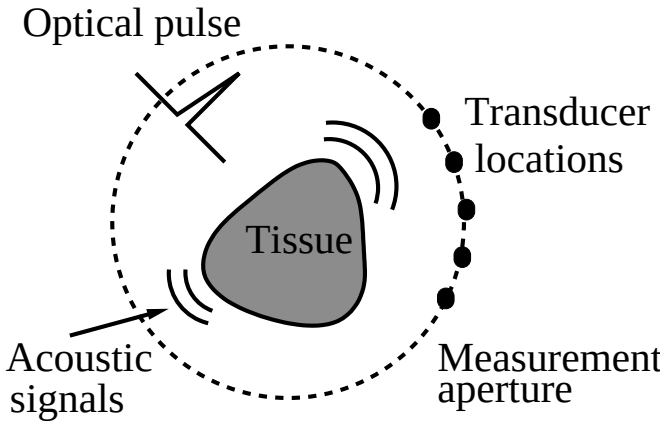

Figure 2.1: A schematic of the PACT imaging geometry.

homogeneous acoustic properties that match a uniform and lossless background medium,

and the duration of the irradiating optical pulse is negligible (acoustic stress confinement is satisfied), the pressure wavefield $p(\mathbf{r}^s, t)$ at a measurement location $\mathbf{r}^s$ can be expressed [119] as:

$$p(\mathbf{r}^s, t) = \frac{\beta}{4\pi C_p} \int_V d\mathbf{r}\, A(\mathbf{r}) \frac{d}{dt} \frac{\delta\left(t - \frac{|\mathbf{r}^s - \mathbf{r}|}{c_0}\right)}{|\mathbf{r}^s - \mathbf{r}|} \equiv \mathcal{H}_{\mathrm{CC}} A(\mathbf{r}), \tag{2.1}$$

where c_0 is the (constant) speed-of-sound in the object and background medium. The function $A(\mathbf{r})$ is compactly supported, bounded and non-negative, and the integration in Eqn. (2.1) is performed over the object's support volume V. We introduce the operator notation $\mathcal{H}_{\mathrm{CC}}$ to represent the continuous-to-continuous (C-C) mapping from $A(\mathbf{r})$ to $p(\mathbf{r}^s, t)$. Equation (2.1) represents a canonical imaging model for PACT.

The imaging model in Eqn. (2.1) can be expressed in an alternate but mathematically equivalent form as

$$g(\mathbf{r}^s, t) = \int_V d\mathbf{r}\, A(\mathbf{r})\, \delta\left(c_0 t - |\mathbf{r}^s - \mathbf{r}|\right), \tag{2.2}$$

where the integrated data function $g(\mathbf{r}^s, t)$ is related to $p(\mathbf{r}^s, t)$ as

$$p(\mathbf{r}^s, t) = \frac{\beta}{4\pi C_p} \frac{\partial}{\partial t}\Big(\frac{g(\mathbf{r}^s, t)}{t}\Big). \tag{2.3}$$

Note that $g(\mathbf{r}^s, t)$ represents a scaled version of the acoustic velocity potential [114, 1]. Equation (2.2) represents a spherical Radon transform [34, 75], and indicates that the integrated data function describes integrals over concentric spherical surfaces of radii $c_0 t$ that are centered at the receiving transducer location $\mathbf{r}^s$.

The inverse problem in PACT is to determine an estimate of $A(\mathbf{r})$ from knowledge of the measured $p(\mathbf{r}^s, t)$. Conventional image reconstruction algorithms assume that the full knowledge of the pressure wavefield $p(\mathbf{r}^s, t)$ is available, in which case a variety of exact reconstruction formulae have been proposed [119, 121, 34, 122, 35, 55, 56, 94, 41]. In Chapter 3, a novel exact reconstruction formula will be proposed, which is also based on the continuous imaging model Eqn. (2.1).

2.2 Continuous-to-Discrete (C-D) Imaging Models

In practice, the acoustic wavefield is sensed by use of either piezoelectric transducers [115, 15, 52] or optical transducers [82, 85, 36] placed at a finite number of detecting locations. At each detecting location, the acoustic wavefield is converted to an electrical signal that is subsequently sampled and recorded by use of a data acquisition system. Therefore, it is natural to introduce a vector $\mathbf{u} \in \mathbb{R}^M$ to denote the lexicographically ordered measurement data, where $M = QK$ with Q and K the number of detecting locations and the number of temporal samples respectively. Various physical models have been proposed to characterize the behavior of ultrasonic transducers [67, 90, 49, 117], thus formulating the relation between $\mathbf{u}$ and $p(\mathbf{r}^s, t)$. In Chapter 4, an impulse response method [102, 63, 97, 91, 40, 116, 29] will be employed to characterize the transducers' behavior. This section provides a generic mathematical description that formulates the practical PACT image system as a C-D mapping from $A(\mathbf{r})$ to $\mathbf{u}$.

Mathematically, a C-D version of Eqn. (2.1) can be obtained by introducing a discretization operator $\mathcal{D}_{\sigma\tau}$ [9, 104]:

$$\mathbf{u} = \mathcal{D}_{\sigma\tau}\mathcal{H}_{\mathrm{CC}}A(\mathbf{r}) \equiv \mathcal{H}_{\mathrm{CD}}A(\mathbf{r}), \tag{2.4}$$

where $\mathcal{D}_{\sigma\tau}$ characterizes the temporal and spatial sampling characteristics of the ultrasonic transducer. Assuming a linear sampling process, $\mathcal{D}_{\sigma\tau}$ can be defined as

$$[\mathbf{u}]_{qK+k} = [\mathcal{D}_{\sigma\tau}p(\mathbf{r}^s, t)]_{qK+k} \equiv \int_{-\infty}^{\infty} dt\, \tau_k(t) \int_S d\mathbf{r}^s\, p(\mathbf{r}^s, t)\sigma_q(\mathbf{r}^s), \tag{2.5}$$

where $q = 0, 1, \ldots, Q-1$ is the index that specifies the q-th transducer located on the measurement aperture S, $k = 0, 1, \ldots, K-1$ is the index of each time sample, and $[\mathbf{u}]_{qK+k}$ denotes the $(qK+k)$-th element of $\mathbf{u}$. The functions $\sigma_q(\mathbf{r}^s)$ and $\tau_k(t)$ describe the spatial and temporal *sampling apertures*, respectively. They are determined by the sampling properties of ultrasonic transducers. For example, in the ideal case, where both apertures are described by Dirac delta functions, the k-th temporal sample recorded by the q-th transducer is equivalent to the value of the pressure function at time $k\Delta_t$ and location $\mathbf{r}_q^s$, i.e,

$$[\mathbf{u}]_{qK+k} = p(\mathbf{r}_q^s, k\Delta_t), \tag{2.6}$$

where Δ_t is the temporal sampling interval.

On substitution from Eqn. (2.1) to Eqn. (2.5), the C-D imaging model can be explicitly expressed as

$$[\mathbf{u}]_{qK+k} = \int_V d\mathbf{r}\ A(\mathbf{r})\, h_{qK+k}(\mathbf{r}), \tag{2.7}$$

where the point response function $h_{qK+k}(\mathbf{r})$ is defined as

$$h_{qK+k}(\mathbf{r}) \equiv \frac{\beta}{4\pi C_p} \int_{-\infty}^{\infty} dt\ \tau_k(t) \int_S d\mathbf{r}^s\ \sigma_q(\mathbf{r}^s) \frac{d}{dt} \frac{\delta(t - \frac{|\mathbf{r}^s - \mathbf{r}|}{c_0})}{|\mathbf{r}^s - \mathbf{r}|}. \tag{2.8}$$

By use of the singular value decomposition of the C-D operator in Eqn. (2.7), a pseudoinverse solution can be computed numerically to estimate $A(\mathbf{r})$ [9].

2.3 Discrete-to-Discrete (D-D) Imaging Models

When iterative image reconstruction algorithms are employed, a finite dimensional representation of $A(\mathbf{r})$ [9] is required. In Section 2.3.1, we review some finite dimensional representations that have been employed in PACT. In Section 2.3.2, computer-simulation studies are conducted to demonstrate the effects of error in the object representation.

2.3.1 Finite-Dimensional Object Representations

An N-dimensional representation of $A(\mathbf{r})$ can be described as

$$A^a(\mathbf{r}) = \sum_{n=0}^{N-1} [\boldsymbol{\alpha}]_n \psi_n(\mathbf{r}), \tag{2.9}$$

where the superscript a indicates that $A^a(\mathbf{r})$ is an approximation of $A(\mathbf{r})$. The functions $\{\psi_n(\mathbf{r})\}_{n=0}^{N-1}$ are called expansion functions and the corresponding expansion coefficients form an N-dimensional vector denoted by $\boldsymbol{\alpha}$. The goal of iterative image reconstruction algorithms is to estimate $\boldsymbol{\alpha}$ for a fixed choice of the expansion functions $\{\psi_n(\mathbf{r})\}_{n=0}^{N-1}$.

The most commonly employed expansion functions are uniform image voxels

$$\psi_n(x,y,z) = \begin{cases} 1, & \text{if} \quad |x-x_n|, |y-y_n|, |z-z_n| \leq \Delta_s/2 \\ 0, & \text{otherwise} \end{cases} \tag{2.10}$$

where $\mathbf{r}_n = (x_n, y_n, z_n)$ specify the coordinates of the n-th grid point of a uniform Cartesian grid of spacing Δ_s. In PACT, spherical expansion functions of the form

$$\psi_n(x,y,z) = \begin{cases} 1, & \text{if} \quad |\mathbf{r}-\mathbf{r}_n| \leq \Delta_s/2 \\ 0, & \text{otherwise} \end{cases} \tag{2.11}$$

have also proven to be useful [47, 27, 105, 110]. The merit of this kind of expansion function is that the acoustic wave generated by each voxel can be calculated analytically. This facilitates determination of the system matrix utilized by iterative image reconstruction methods, as discussed below. Numerous other effective choices for the expansion functions [58] exist including wavelets or other sets of functions that can yield sparse object representations [89].

In addition to an infinite number of choices for the expansion functions, there are an infinite number of ways to define the expansion coefficients $\boldsymbol{\alpha}$. Some common choices include

$$[\boldsymbol{\alpha}]_n = \int_V d\mathbf{r}\, \psi_n(\mathbf{r}) A(\mathbf{r}), \tag{2.12}$$

or

$$[\boldsymbol{\alpha}]_n = \int_V d\mathbf{r}\, \delta(\mathbf{r}-\mathbf{r}_n) A(\mathbf{r}). \tag{2.13}$$

For a given N, different choices of $\{\psi_n\}_{n=0}^{N-1}$ and $\boldsymbol{\alpha}$ will yield object representations that possess different representation errors

$$\delta A(\mathbf{r}) = A(\mathbf{r}) - A^a(\mathbf{r}). \tag{2.14}$$

An example of the effects of such representation errors on iterative reconstruction methods is provided in Section 2.4.

2.3.2 D-D Imaging Models

Discrete-to-discrete imaging models are required for iterative image reconstruction. These can be obtained systematically by substitution of a finite-dimensional object representation into the C-D imaging model in Eqn. (2.4):

$$\mathbf{u}^a = \mathcal{H}_{CD}\mathbf{A}^a(\mathbf{r}) = \sum_{n=0}^{N-1}[\boldsymbol{\alpha}]_n \mathcal{H}_{CD}\{\psi_n(\mathbf{r})\} \equiv \mathbf{H}\boldsymbol{\alpha}, \tag{2.15}$$

where the D-D operator $\mathbf{H}$ is commonly referred to as the system matrix. Note that the data vector $\mathbf{u}^a \neq \mathbf{u}$, due to the fact that a finite-dimensional approximate object representation was employed. In other words, $\mathbf{u}^a$ represents an approximation of the measured data. The system matrix $\mathbf{H}$ is of dimension $QK \times N$, and each element of $\mathbf{H}$, denoted by $[\mathbf{H}]_{qK+k,n}$, is defined by

$$[\mathbf{H}]_{qK+k,n} = \int_V d\mathbf{r}\, \psi_n(\mathbf{r}) h_{qK+k}(\mathbf{r}) \equiv [\mathcal{D}_{\sigma\tau}\big\{p_n(\mathbf{r}^s, t)\big\}]_{qK+k}, \tag{2.16}$$

where $h_{qK+k}(\mathbf{r})$ is defined in Eqn. (2.8) and

$$p_n(\mathbf{r}^s, t) = \frac{\beta}{4\pi C_p}\int_V d\mathbf{r}\, \psi_n(\mathbf{r}) \frac{d}{dt}\frac{\delta(t - \frac{|\mathbf{r}^s - \mathbf{r}|}{c_0})}{|\mathbf{r}^s - \mathbf{r}|}. \tag{2.17}$$

Equation (2.16) provides a clear two-step procedure for computing the system matrix. First, $p_n(\mathbf{r}^s, t)$ is computed. Physically this represents the pressure data, in its continuous form, received by an ideal point transducer when the absorbing object corresponds to $\psi_n(\mathbf{r})$. Secondly, a discretization operator is applied that samples the ideal data and degrades it by the transducer response. Alternatively, the elements of the system matrix can be measured experimentally by scanning an object whose form matches the expansion functions through the object volume and recording the resulting electrical signal at each transducer location $\mathbf{r}_q^s$, for each value of n (location of expansion function), at time intervals $k\Delta_t$. For the case of spherical expansion elements, this approach was implemented in [28].

This two step approach for determining $\mathbf{H}$ can be formulated as

$$\mathbf{H} = \mathbf{S} \circ \mathbf{H}_0, \tag{2.18}$$

where, '$\circ$' denotes an element-wise product. Each element of $\mathbf{H}_0$ is defined as

$$[\mathbf{H}_0]_{qK+k,n} = p_n(\mathbf{r}_q^s, k\Delta_t). \tag{2.19}$$

The $QK \times N$ matrix $\mathbf{S}$ can be interpreted as a sensitivity map whose elements are defined as

$$[\mathbf{S}]_{qK+k,n} = \frac{[\mathcal{D}_{\sigma\tau}\{p_n(\mathbf{r}^s, t)\}]_{qK+k}}{p_n(\mathbf{r}_q^s, k\Delta_t)}. \tag{2.20}$$

Numerical Example: Impact of Representation Error on Simulated Pressure Data

Consider a uniform sphere of radius $R = 5$mm as the optical absorber (acoustic source) that is centered at $\mathbf{r}$. Assuming Dirac delta (i.e., ideal) temporal and spatial sampling, the pressure data were computed at a measurement location $\mathbf{r}^s$ that was 65-mm away from the center of the sphere by use of C-D and D-D imaging models. For the uniform sphere, the pressure waveform can be computed analytically as

$$p(\mathbf{r}^s, k\Delta_t) = \begin{cases} \frac{\beta c_0^2}{2C_p|\mathbf{r}^s - \mathbf{r}|}(|\mathbf{r}^s - \mathbf{r}| - c_0 k\Delta_t), & \text{if } \left|c_0 k\Delta_t - |\mathbf{r}^s - \mathbf{r}|\right| \leq R \\ 0, & \text{otherwise} \end{cases}, \tag{2.21}$$

where Δ_t is the sampling interval. The pressure possesses an 'N'-shape waveform shown as the dashed red curve in Fig. 2.2. Finite dimensional object representations of the object were obtained according to Eqn. (2.9) with $\psi_n(\mathbf{r})$ corresponding to the uniform spheres described in Eqn. (2.11). The expansion coefficients were computed according to Eqn. (2.12) scaled by a factor of $6/\pi$. Two approximate object representations were considered. The first representation employed $N = 256^3$ spherical expansion functions of radius 0.04-mm while the second employed $N = 64^3$ expansion functions of radius 0.16-mm. The resulting pressure signals are shown as Fig. 2.2, where the speed of sound $c_0 = 1.521$-mm/μs, and $\Delta_t = 0.05$-μs. As expected, the error in the computed pressure data increases as the voxel size is increased. In practice, this error would represent a data inconsistency between the measured data and the assumed D-D imaging model, which can result in image artifacts as demonstrated by the example below.

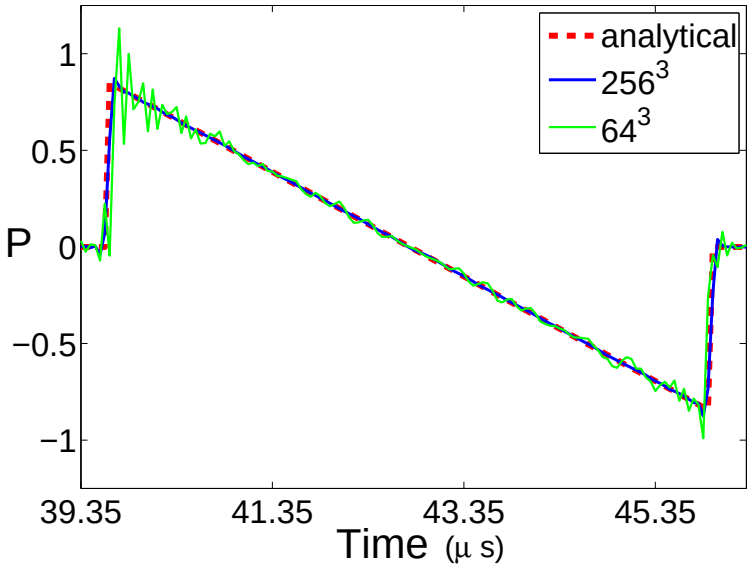

Figure 2.2: Pressure data generated by continuous imaging model (red dash) and discrete imaging model using $256 \times 256 \times 256$ voxels (blue solid) and $64 \times 64 \times 64$ voxels (green solid).

2.4 Iterative Image Reconstruction

Once the system matrix $\mathbf{H}$ is determined, as described in the previous section, an estimate of $A(\mathbf{r})$ can be computed in two distinct steps. First, from knowledge of the measured data and system matrix, Eqn. (2.15) is inverted to estimate the expansion coefficients $\boldsymbol{\alpha}$. Secondly, the estimated expansion coefficients are employed with Eqn. (2.9) to determine the finite-dimensional approximation $A^a(\mathbf{r})$. Each of steps introduces errors into the final estimate of $A(\mathbf{r})$. In the first step, due to noise in the measured data $\mathbf{u}^a$, modeling errors in $\mathbf{H}$, and/or if $\mathbf{H}$ is not of full rank, the true values of coefficients $\boldsymbol{\alpha}$ cannot generally be determined. The estimated $\boldsymbol{\alpha}$ will therefore depend on the definition of the approximate solution and the particular numerical algorithm used to determine it. Even if $\boldsymbol{\alpha}$ could somehow be determined exactly, the second step would introduce error due to the approximate finite-dimensional representation of $A(\mathbf{r})$ employed. This error is influenced by the choice of N and $\psi_n(\mathbf{r})$, and is object dependent.

Due to the large size of $\mathbf{H}$, iterative methods are often employed to estimate $\boldsymbol{\alpha}$. Iterative approaches offer a fundamental and flexible way to incorporate *a prior* information regarding the object, to improve the accuracy of the estimated $\boldsymbol{\alpha}$. A vast literature on iterative image reconstruction methods exists [69, 7, 31, 33] which we leave to the reader to explore. Examples of applications of iterative reconstruction methods in PACT are described in references [84, 1, 2, 132, 4, 27, 105, 110]. A numerical example demonstrating how object representation error can affect the accuracy of iterative image reconstruction is provided next.

Numerical Example: Influence of Representation Error on Image Accuracy

We assume focused transducers are employed that receive only acoustic pressure signals transmitted from the imaging plane, and therefore the three-dimensional (3D) spherical Radon transform image model is degraded to a 2D circular mean model. A 2D phantom comprised of uniform disks possessing different gray levels, radii, and locations, was assumed to represent $A(\mathbf{r})$. The radius of the phantom was 1.0 in arbitrary units. A finite-dimensional representation $A^a(\mathbf{r})$ was formed according to Eqn. (2.9) with $N = 256^2$ and $\psi_n(\mathbf{r})$ chosen to be conventional pixels described by a 2D version of Eqn. (2.10). The expansion coefficients $[\boldsymbol{\alpha}]_n$ were computed by use of Eqn. (2.13). Figure 2.3 displays the computed expansion coefficient vector $\boldsymbol{\alpha}$ that has been reshaped into a 256×256 for display purposes.

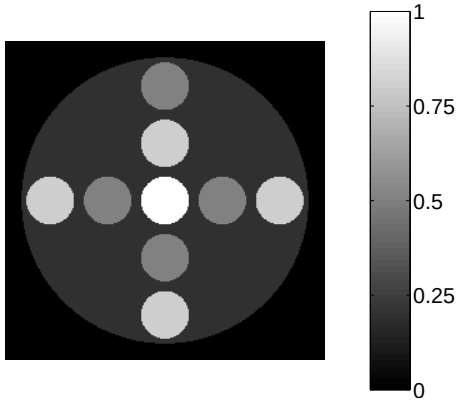

Figure 2.3: The 2D numerical phantom $\boldsymbol{\alpha}$ representing the object function $A(\mathbf{r})$

.

A circular measurement aperture S of radius 1.2 that enclosed the object was employed. At each of 360 uniformly spaced transducer locations $\{\mathbf{r}_q^s\}_{q=0}^{Q-1}$ on the measurement circle, simulated voltage data $\mathbf{u}$ were computed from the integrated data $\mathbf{g}$ by use of the formula

$$[\mathbf{u}]_{qK+k} = \frac{\beta}{4\pi C_p c_0}\left[\frac{g_{[qK+k+1]}/(k+1) - g_{[qK+k-1]}/(k-1)}{2\Delta_t^2}\right]. \tag{2.22}$$

Here, we assume idealized sampling apertures, i.e, the meaured voltage signals are equivalent to the values of the pressure function. Two versions of the voltage data were computed, corresponding to the cases where $\mathbf{g}$ was computed analytically or by use of the assumed D-D imaging model. These simulated voltage data are denoted by $\mathbf{u}_{ana}$ and $\mathbf{u}_{num}$ respectively. At each transducer location, 300 temporal samples were computed. Accordingly, the voltage vector $\mathbf{u}^a$ was a column vector of length 360×300.

The conjugate gradient algorithm was employed to find the least squares estimate $\hat{\boldsymbol{\alpha}}$,

$$\hat{\boldsymbol{\alpha}} = \arg\min_{\boldsymbol{\alpha}} \|\mathbf{u} - \mathbf{H}\boldsymbol{\alpha}\|^2, \tag{2.23}$$

where $\mathbf{u} = \mathbf{u}_{ana}$ or $\mathbf{u}_{num}$. For the noiseless data, the images reconstructed from $\mathbf{u}_{ana}$ and $\mathbf{u}_{num}$ after 150 iterations are shown as Fig. 2.4-(a) and (b), respectively. The image reconstructed from the data $\mathbf{u}_{num}$ is free of significant artifacts and is nearly identical to the original object. This is expected because the finite-dimensional object representation was used to produce the simulated measurement data and establish the system matrix, and therefore the system of equations in Eqn. (2.15) is consistent. Generating simulation data in this way would constitute an "inverse crime". Conversely, the image reconstructed from the data $\mathbf{u}_{ana}$ contained high-frequency artifacts due to the fact that the system of equations in Eqn. (2.15) is inconsistent. The error in the reconstructed images could be minimized by increasing the dimension of the approximate object representation. This simple example demonstrates the importance of carefully choosing a finite-dimensional object representation in iterative image reconstruction.

2.5 Summary

Photoacoustic computed tomography is a rapidly emerging biomedical imaging modality that possesses many challenges for image reconstruction. In this chapter, the continuous imaging models that relate the measured photoacoustic wavefields to the sought-after optical absorption distribution were described in their continuous form. We also described generic methodologies to construct numerical imaging models for the use of iterative image reconstruction algorithms.

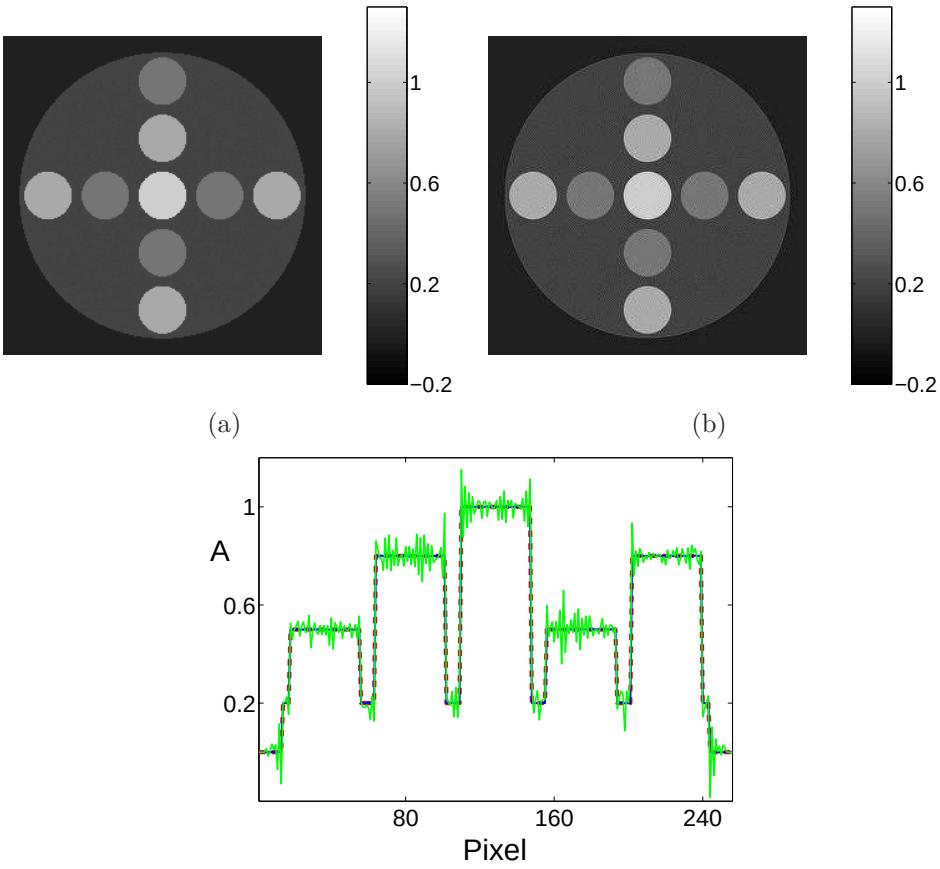

Figure 2.4: Images reconstructed by the least squares conjugate gradient algorithm from voltage data obtained by (a) numerical image model and (b) analytical imaging model. (c) Vertical profiles through the center of subfigure(a)(solid blue), subfigure(b)(solid green), and Fig. 2.3(dashed red).

Chapter 3

A Simple Fourier Transform-Based Reconstruction Formula for PACT

3.1 Introduction

A variety of image reconstruction algorithms have been proposed for PACT [121, 34, 122, 35, 55, 41, 56, 94, 101]. While iterative image reconstruction methods hold great value due to their ability to incorporate accurate models of the imaging physics and the instrument response [84, 127, 133, 89, 105, 37, 44, 17, 16, 110], they can lead to long reconstruction times, even when accelerated by use of modern computing hardware such as graphics processing units [110]. This is especially problematic in three-dimensional (3D) implementations of PACT, in which reconstruction times can be excessively long. Almost all experimental studies of PACT to date have employed analytic image reconstruction algorithms. Even if an iterative image reconstruction algorithm is to be employed, it is often useful to employ an analytic reconstruction algorithm to obtain a preliminary image that can initialize the iterative algorithm and thereby accelerate its convergence.

Most analytic reconstruction algorithms for PACT with a spherical measurement aperture and point-like transducers have been formulated in the form of filtered backprojection (FBP) algorithms. These algorithms possess a large computational burden, requiring $O(N^5)$ floating point operations to reconstruct a 3D image of dimension N^3. Image reconstruction algorithms based on the time-reversal principle and finite-difference schemes require $O(N^4)$ operations [19]. Fast reconstruction algorithms for spherical measurement apertures that

require only $O(N^3 logN)$ operations have been proposed [56, 94]. However, numerical implementations of these formulas require computation of special functions and multidimensional interpolation operations in Fourier space, which require special care to avoid degradation in reconstructed image accuracy. It is well-known that the temporal frequency components of the pressure data recorded on a spherical surface are related to the Fourier components of the sought-after object function [5]. However, to date, a simple reconstruction algorithm based on this relationship, i.e., one that does not require series expansions involving special functions or multi-dimensional interpolations, has yet to be developed.

In this chapter, we derive a novel reconstruction formula for two-dimensional (2D) and 3D PACT employing circular and spherical measurement geometries, respectively. The mathematical forms of the reconstruction formulae are the same in both dimensions and are surprisingly simple compared with existing Fourier-domain reconstruction formulae for spherical and circular measurement geometries. The reconstruction formulae are mathematically exact and describe explicitly how the spatial frequency components of the sought-after object function are determined by the temporal frequency components of the measured pressure data. Their discrete implementations require only discrete Fourier transform, one-dimensional interpolation, and summation operations. A preliminary computer-simulation study is conducted to corroborate the validity of the reconstruction formula.

3.2 Derivation of the Reconstruction Formula

We consider the canonical PACT imaging model in which the object and surrounding medium are assumed to possess homogeneous and lossless acoustic properties and the object is illuminated by a laser pulse with negligible temporal width. Point-like, unfocused, ultrasonic transducers are assumed. We also assume that the effects of the acousto-electric impulse responses of the transducers have been deconvolved [105, 110] from the measured voltage signals so that the measured data can be interpreted as pressure signals. The 3D problem is addressed where $p(\mathbf{r}, t)$ denotes the photoacoustically-induced pressure wavefield at location $\mathbf{r} \in \mathbb{R}^3$ and time $t \geq 0$. However, the analysis and reconstruction formula that follows remains valid for the 2D case. The imaging physics is described by the photoacoustic wave

equation [68, 112, 51]:

$$\nabla^2 p(\mathbf{r}, t) - \frac{1}{c_0^2} \frac{\partial^2 p(\mathbf{r}, t)}{\partial^2 t} = 0, \tag{3.1}$$

subject to the initial conditions:

$$p(\mathbf{r}, t)\Big|_{t=0} = \frac{\beta c_0^2}{C_p} A(\mathbf{r}); \quad \frac{\partial p(\mathbf{r}, t)}{\partial t}\Big|_{t=0} = 0, \tag{3.2}$$

where ∇^2 denotes the 3D Laplacian operator and $A(\mathbf{r})$ is the object function to be reconstructed that is contained within the volume V. Physically, $A(\mathbf{r})$ represents the distribution of absorbed optical energy density. The constant quantities β, c_0, and C_p denote the thermal coefficient of volume expansion, speed-of-sound, and the specific heat capacity of the medium at constant pressure, respectively.

Let $p(\mathbf{r}^s, t)$ denote the pressure data recorded at location $\mathbf{r}^s \in S$ on a spherical surface S of radius R^s that encloses V. The continuous form of the imaging model that relates the measurement data to object function can be expressed as [24]:

$$p(\mathbf{r}^s, t) = \mathcal{H}_{\text{CC}} A \equiv \frac{\beta c_0^2}{C_p (2\pi)^3} \int_\infty d\mathbf{k}\, \hat{A}(\mathbf{k}) \cos(c_0 k t) e^{\hat{\imath}\mathbf{k}\cdot\mathbf{r}^s}, \tag{3.3}$$

where $\mathbf{k} \in \mathbb{R}^3$ is the spatial frequency vector conjugate to $\mathbf{r}$, $k \equiv |\mathbf{k}|$, and $\hat{A}(\mathbf{k})$ is the 3D Fourier transform of $A(\mathbf{r})$. We adopt the Fourier transform convention

$$\hat{A}(\mathbf{k}) = \mathcal{F}_3 A(\mathbf{r}) \equiv \int_\infty d\mathbf{r} A(\mathbf{r}) e^{-\hat{\imath}\mathbf{k}\cdot\mathbf{r}} \tag{3.4a}$$

$$A(\mathbf{r}) = \mathcal{F}_3^{-1} \hat{A}(\mathbf{k}) \equiv \frac{1}{(2\pi)^3} \int_\infty d\mathbf{k} \hat{A}(\mathbf{k}) e^{\hat{\imath}\mathbf{k}\cdot\mathbf{r}}. \tag{3.4b}$$

The imaging model in Eqn. (3.3) can be interpreted as a mapping $\mathcal{H}_{\text{CC}} : O \to D$ between infinite dimensional vector spaces that contain the object and data functions. We will define O as the vector space of bounded and smooth functions that are compactly supported within the volume V. It can be shown that Eqn. (3.3) is equivalent to Eqn. (2.1) [23].

Let the infinite set of functions $\{\gamma_\mu(\mathbf{r})\}$, indexed by μ, represent an orthonormal basis for O. The object function $A(\mathbf{r})$ can be represented as

$$A(\mathbf{r}) = \int_\infty d\mu \, \langle A, \gamma_\mu \rangle \gamma_\mu(\mathbf{r}), \tag{3.5}$$

where the inner product in O is defined as

$$\langle A, \gamma_\mu \rangle \equiv \int_V d\mathbf{r} A(\mathbf{r}) \gamma_\mu(\mathbf{r}) = \frac{1}{(2\pi)^3} \int_\infty d\mathbf{k} \, \hat{A}(\mathbf{k}) \hat{\gamma}_\mu(\mathbf{k}), \tag{3.6}$$

$\hat{\gamma}_\mu(\mathbf{k}) = \mathcal{F}_3 \gamma_\mu(\mathbf{r})$, and the quantity on the right-hand side of Eqn. (3.6) follows from fact that the Fourier transform is an isometry. A trace identity (see Eqn. (1.7) in reference [34] for the 3D case and Eqn. (1.16) in [35] for the 2D case) can be employed to relate the inner products in the spaces O and D as:

$$\langle A, \gamma_\mu \rangle = \frac{2C_p^2}{R^s \beta^2 c_0^2} \int_0^\infty dt \int_S d\mathbf{r}^s \, t \, p(\mathbf{r}^s, t) v_\mu(\mathbf{r}^s, t), \tag{3.7}$$

where

$$v_\mu(\mathbf{r}^s, t) = \mathcal{H}_{\mathrm{CC}} \gamma_\mu = \frac{\beta c_0^2}{C_p (2\pi)^3} \int_\infty d\mathbf{k} \, \hat{\gamma}(\mathbf{k}) \cos(c_0 k t) e^{\hat{\imath} \mathbf{k} \cdot \mathbf{r}^s}, \tag{3.8}$$

and the right-hand side of Eqn. (3.7) defines a scaled version of the inner product in D.

On substitution from Eqn. (3.8) into Eqn. (3.7), one obtains

$$\langle A, \gamma_\mu \rangle = \frac{1}{(2\pi)^3} \int_\infty d\mathbf{k} \, \hat{y}(\mathbf{k}) \hat{\gamma}_\mu(\mathbf{k}), \tag{3.9}$$

where

$$\hat{y}(\mathbf{k}) \equiv \frac{2C_p}{R^s \beta} \int_S d\mathbf{r}^s e^{\hat{\imath} \mathbf{k} \cdot \mathbf{r}^s} \int_0^\infty dt \, t p(\mathbf{r}^s, t) \cos(c_0 k t). \tag{3.10}$$

Comparison of Eqns. (3.6) and (3.9) reveals that $\hat{A}(\mathbf{k}) = \hat{y}(\mathbf{k})$. By evaluating the Fourier cosine transform that is present in the right-hand side of Eqn. (3.10), a reconstruction formula for determining $\hat{A}(\mathbf{k})$ can therefore be expressed as

$$\hat{A}(\mathbf{k}) = \frac{2C_p}{R^s \beta} \int_S d\mathbf{r}^s e^{\hat{\imath} \mathbf{k} \cdot \mathbf{r}^s} \mathrm{Re}\Big\{ \mathcal{F}_1 \big\{ tp(\mathbf{r}^s, t) \big\} (\mathbf{r}^s, \omega) \big|_{\omega = c_0 k} \Big\}, \tag{3.11}$$

where $\mathcal{F}_1$ denotes the one-dimensional (1D) Fourier transform with respect to time t and 'Re' denotes the operation that takes the real part of quantity in the brackets. Subsequently, $A(\mathbf{r})$ is determined as $\mathcal{F}_3^{-1}\hat{A}(\mathbf{k})$.

Equation (3.11) represents a novel reconstruction for PACT and is the key result of this chapter. Unlike previously proposed Fourier-domain reconstruction formulae [74, 56, 94], Eqn. (3.11) has a simple form and does not involve series expansions utilizing special functions. The reconstruction formula reveals that the measured data $p(\mathbf{r}^s, t)$ determine the 3D Fourier components of the $A(\mathbf{r})$ via a simple process that involves the following four steps: (1) Compute the 1D temporal Fourier transform of the modified data function $tp(\mathbf{r}^s, t)$; (2) Isolate the real-valued component of this quantity corresponding to temporal frequency $\omega = c_0 k$; (3) Weight this value by the plane-wave $e^{i\mathbf{k}\cdot\mathbf{r}^s}$; and (4) Sum the contributions, formed in this way, corresponding to every measurement location $\mathbf{r}^s \in S$. This reveals the components of $\hat{A}(\mathbf{k})$ residing on a sphere of radius $\frac{k}{c_0}$ are determined by the 1D Fourier transform of $tp(\mathbf{r}^s, t)$ corresponding to temporal frequency ω. In this sense, Eqn. (3.11) can be interpreted as an implementation of the Fourier Shell Identity [5]. Finally, the form of Eqn. (3.11) remains unchanged in the 2D case, where $\mathbf{r}^s, \mathbf{k} \in \mathbb{R}^2$ and S is a circle that encloses the object.

A discrete implementation of Eqn. (3.11) possesses low computational complexity and desirable numerical properties. The 1D fast Fourier transform (FFT) can be employed to approximate the action of $\mathcal{F}_1$ and only a 1D interpolation is required to determine the value of the Fourier transformed data function corresponding to temporal frequency $\omega = c_0 k$, where k corresponds to the magnitude of vectors $\mathbf{k}$ that specify a 3D Cartesian grid. From the values of $\hat{A}(\mathbf{k})$ determined on this grid, the 3D FFT algorithm can be employed to estimate values of $A(\mathbf{r})$. If the object is represented on a $N \times N \times N$ grid and the number of transducer locations and time samples are both $\mathcal{O}(N)$, the computational complexity is limited by the 3D FFT algorithm, i.e., $\mathcal{O}(N^2 \log N)$ in 2D and $\mathcal{O}(N^3 \log N)$ in 3D.

3.3 Computer-Simulation Studies

Images were reconstructed on a uniform 2D grid of spacing 0.1-mm by use of a discretized form of Eqn. (3.11) coupled with the 2D inverse FFT algorithm. In order to reconstruct images of dimension 256×256, samples of $\hat{A}(\mathbf{k})$ were determined on a uniform 2D grid of

dimension 512×512 with a sampling interval of $(0.1 \times 256)^{-1}$-mm^{-1}. The samples of the data function $tp(\mathbf{r}^s, t)$ were zero-padded by a factor of 8 prior to estimating its 1D Fourier transform by use of the FFT algorithm. From these data, nearest neighbor 1D interpolation was employed to determine the values of the term in brackets in Eqn. (3.11) corresponding to $\omega = c_0 k$ for the sampled locations $\mathbf{k}$.

The images reconstructed from the noiseless and noisy data sets are shown in Fig. 3.1-(b) and (c). Profiles corresponding to the central rows of these images are shown in Fig. 3.2. These results confirm that the proposed reconstruction algorithm can reconstruct images with high fidelity from noise-free measurement data. Although, a systematic investigation of the noise propagation properties of the proposed algorithm is beyond the scope of this Note, Figs. 3.1-(c) and 3.2-(b) suggest that its performance is robust in the presence of noise. This is to be expected, since all operations involved in the implementation of Eqn. (3.11) are numerically stable.

3.4 Summary

In summary, we have derived a Fourier-based reconstruction formula for PACT employing circular and spherical measurement apertures. The formula is mathematically exact and possesses a surprisingly simple form compared with existing Fourier-domain reconstruction formulae. The formula yields a straightforward numerical implementation that is stable and is two orders of magnitude more computationally efficient than 3D filtered backprojection algorithms. The proposed formula serves as an alternative to existing fast Fourier-based reconstruction formulae. A systematic comparison of the proposed reconstruction formula with existing formulae by use of experimental data remains an important topic for future studies.

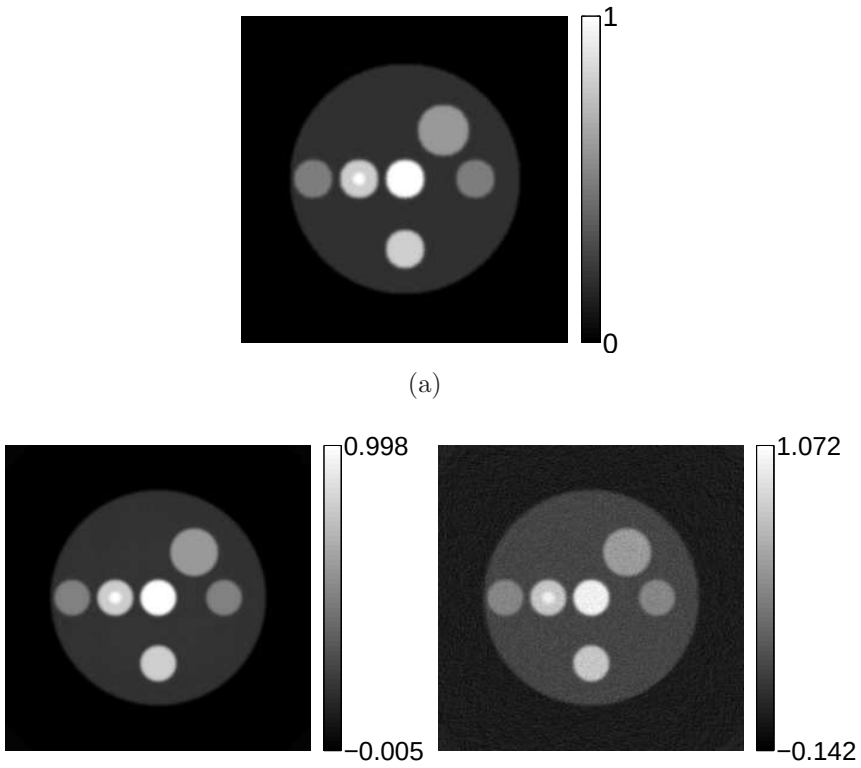

(a)

(b)

(c)

Figure 3.1: The numerical phantom is shown in subfigure (a). Images reconstructed by use of the proposed reconstruction algorithm from noiseless and noisy data are shown in subfigures (b) and (c), respectively.

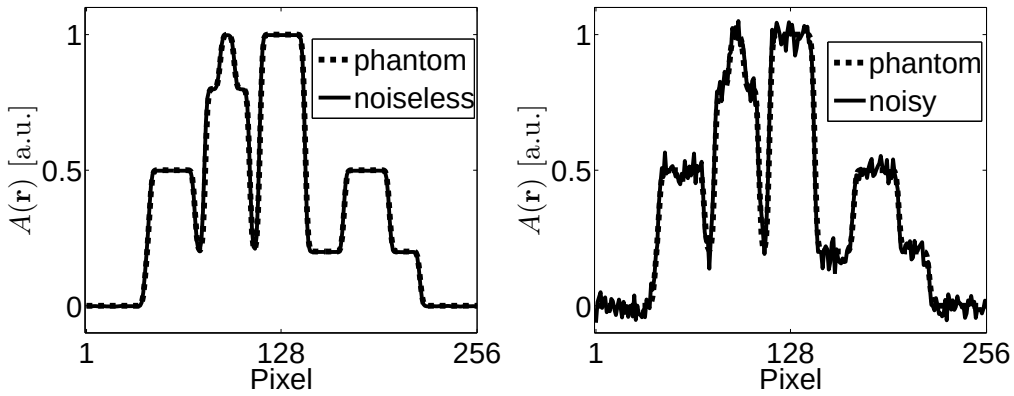

(a) (b)

Figure 3.2: Profiles corresponding to the central rows of the images shown in Fig. 3.1-(b) (subfigure(a)) and Fig. 3.1-(c) (subfigure(b)). The solid line in subfigure (a), which corresponds to the image reconstructed from noiseless data, almost completely overlaps with the profile through the numerical phantom.

Chapter 4

An Imaging Model Incorporating Ultrasonic Transducer Properties for 3D PACT

4.1 Introduction

A variety of analytical [121, 34, 122, 35, 55, 41, 56, 94, 101] and iterative [1, 27, 84, 133] PACT image reconstruction algorithms have been developed. Many of these algorithms are based on a spherical Radon transform image model and assume that point-like ultrasonic transducers are employed for data-acquisition. This assumption is appropriate when the size of the transducer's detecting surface is sufficiently small and/or the object-to-transducer distance is sufficiently large. However, the use of small transducers and/or large scanning distances is undesirable because the signal-to-noise ratio of the recorded photoacoustic signals will be degraded [125]. When the characteristics of the transducer are not accounted for in the image reconstruction algorithm, the spatial resolution of the resulting images can be significantly degraded and image distortions can be present.

An ultrasonic transducer in receive-mode can be characterized by its acousto-electric impulse response and spatial impulse response [40, 29]. Their effects on the spatial resolution of the reconstructed images in PACT have been studied previously [70, 5, 51, 25]. The explicit nature of the spatial resolution degradation depends on the measurement geometry, but it is generally spatially variant and, therefore, not modeled as a linear shift-invariant system. Several data-space deconvolution procedures have been proposed [121, 60, 111] for mitigating

the effects of the transducer response on the PACT measurement data. A discrete imaging model that took account of the transducer properties was proposed in [60]. However, specific details about how the object and spatial impulse response were not provided.

It is worth noting that several groups have proposed alternative ultrasound transducer technologies to circumvent the need to numerically compensate for transducer effects in the reconstruction algorithm. For example, virtual point detectors have been investigated [125, 61, 59]. Integrating ultrasound detectors [38, 81] are also being actively explored. Despite these efforts, the majority of current PACT implementations utilize conventional piezoelectric ultrasonic transducer technologies. The use of conventional ultrasound transducers also facilitates hybrid ultrasound-PACT imaging in which the same transducer is utilized for both the traditional ultrasound imaging and for the PACT [53, 130, 3, 64].

In this chapter, a general PACT imaging model that incorporates the physical response of an ultrasound transducer is introduced and investigated. The imaging model is presented in its continuous-to-discrete and discrete-to-discrete forms. Our primary focus is on the discrete-to-discrete model and its application to iterative image reconstruction. By use of computer-simulated and experimental PACT measurement data, we demonstrate that use of the new imaging model in an iterative reconstruction method can improve the spatial resolution of the reconstructed images as compared to those reconstructed assuming point-like ultrasound transducers. The singular value decomposition of the imaging model is computed to investigate how incorporation of the transducer responses in the imaging model will affect the numerical stability of the image reconstruction problem.

The remainder of the chapter is organized as follows. In Section 4.2 we briefly review the impulse response method that will be employed to numerically model the ultrasound transducer response. By use of the impulse response method, continuous-to-discrete and discrete-to-discrete PACT image models that incorporate the acousto-electric and spatial impulse responses of a non-ideal ultrasound transducer are established in Section 4.3. Numerical studies that involve computer-simulated and experimental PACT measurement data are described in Section 4.4, in which an iterative image reconstruction algorithm is utilized with the new discrete-to-discrete imaging model. In Section 4.5, we compare the spatial resolution of the reconstructed images with those reconstructed assuming point-like ultrasound transducers. The article concludes with a summary in Section 4.6.

4.2 Background: Characterization of Transducer Behavior

Two modeling issues are involved in the characterization of transducer behavior. One is to model how the mechanical force is converted to electrical signals when acting on the transducer surface, or the reverse. The energy transformation process can be parametrically modeled by use of equivalent electric circuit methods [67, 90, 49, 117] or numerically simulated by use of finite element methods [57, 8, 77] . Another modeling issue is to model the diffraction effects of the transducer. A typical example is to calculate the transient radiation resulting from a transducer of finite aperture size. The diffraction effects can be investigated by use of the finite element methods [57, 8, 77] or impulse response method [102, 63, 97, 91, 40, 116, 29] . Below, we briefly review the impulse response method developed in the ultrasound literature.

The impulse response method has been developed to calculate the transient velocity potential at a field point resulting from a specified velocity motion of an ultrasonic transducer of finite aperture size. The transducer is treated as a piston mounted in a rigid infinite planar baffle. By use of the Green's function method, the time-dependent velocity potential $\phi(\mathbf{r}, t)$ can be expressed as [97]:

$$\phi(\mathbf{r}, t) = \frac{1}{2\pi} \int_S d\mathbf{r}^s \frac{v(t - |\mathbf{r}^s - \mathbf{r}|/c_0)}{2\pi|\mathbf{r}^s - \mathbf{r}|}, \tag{4.1}$$

where c_0 is the (constant) speed of sound and S denotes the piston area, $\mathbf{r}^s \in S$, and $v(t)$ is the piston velocity that is assumed to be uniform over S. By use of the convolution property of Dirac delta function, Eqn. (4.1) can be reformulated as

$$\phi(\mathbf{r}, t) = v(t) *_t h^s(\mathbf{r}, t), \tag{4.2}$$

where '$*_t$' denotes linear convolution with respect to time coordinate and $h^s(\mathbf{r}, t)$ is defined as

$$h^s(\mathbf{r}, t) = \int_S d\mathbf{r}^s \frac{\delta(t - |\mathbf{r}^s - \mathbf{r}|/c_0)}{2\pi|\mathbf{r}^s - \mathbf{r}|}. \tag{4.3}$$

The function $h^s(\mathbf{r}, t)$ is referred to as the spatial impulse response (SIR) in the literature [102, 63, 97, 91, 40, 116, 29] . A variety of algorithms have been proposed to estimate the

SIR for transducers of various shapes [100, 118, 88, 45]. The technique that converts the surface integral to a temporal convolution is referred to as the impulse response method.

4.3 Discrete PACT Imaging Models that Incorporate Transducer Response

As discussed in Section 2.2, a practical PACT imaging system is properly described as a continuous-to-discrete (C-D) imaging model. In this section, we propose a C-D imaging model that incorporates the characteristics of ultrasonic transducers. Also, we construct a discrete-to-discrete (D-D) imaging model to approximate the C-D model for the use of iterative image reconstruction algorithms.

4.3.1 C-D Imaging Models

A C-D imaging model that incorporates transducer characteristics can be derived from a physical perspective. Let $\mathbf{u} \in \mathbb{R}^M$ denote a vector whose elements are the measured electrical voltage signals arranged in a lexicographical order. Here $M = QK$ with Q and K the number of detecting locations and the number of temporal samples respectively. We will use $[\mathbf{u}]_m$ to denote the m-th element of $\mathbf{u}$. The PACT data acquisition system can be modeled as [29, 105, 110]

$$[\mathbf{u}]_{qK+k} = h^e(t) *_t \frac{1}{S_q} \int_{S_q} d\mathbf{r}^s \, p(\mathbf{r}^s, t)\Big|_{t=k\Delta_t}, \tag{4.4}$$

where $p(\mathbf{r}^s, t)$ is the photoacoustic wavefield defined by Eqn. (2.1), $S_q \subset S$ is the surface area of the q-th transducer, Δ_t is the temporal sampling interval, and '$*_t$' denotes linear convolution with respect to time coordinate. Here the surface inetgral over S_q characterizes the diffraction effect of the transducer. The transducer energy transformation process is assumed to be a linear shift-invariant system whose transfer function is referred to as acousto-electric impulse response (EIR) [29] denoted by $h^e(t)$. On substitution of Eqn. (2.1) into Eqn.

(4.4), a C-D imaging model that incorporates transducer characteristics can be expressed as:

$$[\mathbf{u}]_{qK+k} = h^e(t) *_t \frac{1}{S_q}\int_{S_q} d\mathbf{r}^s \, \frac{\beta}{4\pi C_p}\int_V d\mathbf{r}\, A(\mathbf{r}) \frac{d}{dt}\frac{\delta\left(t-\frac{|\mathbf{r}^s-\mathbf{r}|}{c_0}\right)}{|\mathbf{r}^s-\mathbf{r}|}\Bigg|_{t=k\Delta_t}. \tag{4.5}$$

Equation (4.5) can be interpreted in the framework of the generic C-D imaging model described in Chapter 2 with a special choice of the spatial and temporal sampling aperture functions. To show this, we define the spatial sampling aperture $\sigma_q(\mathbf{r}^s)$ as

$$\sigma_q(\mathbf{r}^s) = \begin{cases} 1/S_q, & \text{if} \quad \mathbf{r}^s \in S_q \\ 0, & \text{otherwise} \end{cases}. \tag{4.6}$$

Also, we define the temporal sampling aperture $\tau_k(t)$ to be associated with the EIR as

$$\tau_k(t) = h^e(k\Delta_t - t). \tag{4.7}$$

On substitution from Eqns. (4.6) and (4.7) into Eqn. (2.8), one obtains an explicit expression of the C-D imaging model as

$$[\mathbf{u}]_{qK+k} = \int_V d\mathbf{r}\; A(\mathbf{r})\, h_{qK+k}(\mathbf{r}), \tag{4.8}$$

where the point response function $h_{qK+k}(\mathbf{r})$ is defined as

$$h_{qK+k}(\mathbf{r}) = \frac{\beta}{4\pi C_p S_q} h^e(t) *_t \int_{S_q} d\mathbf{r}^s \, \frac{d}{dt}\frac{\delta(t-\frac{|\mathbf{r}^s-\mathbf{r}|}{c_0})}{|\mathbf{r}^s-\mathbf{r}|}. \tag{4.9}$$

It is obvious that Eqns. (4.8) and (4.9) are equivalent to Eqn. (4.5).

4.3.2 D-D Imaging Models

Following the generic methodologies discussed in Chapter 2, an N-dimensional representation of $A(\mathbf{r})$ is introduced as

$$A^a(\mathbf{r}) = \sum_{n=0}^{N-1} [\boldsymbol{\alpha}]_n \psi_n(\mathbf{r}). \tag{4.10}$$

We employed the spherical expansion functions [58, 47] defined by

$$\psi_n(\mathbf{r}) = \begin{cases} 1, & \text{if} \quad |\mathbf{r} - \mathbf{r}_n| \leq \Delta_s/2 \\ 0, & \text{otherwise} \end{cases}, \tag{4.11}$$

where $\mathbf{r}_n = (x_n, y_n, z_n)$ specify the coordinates of the n-th grid point of a uniform Cartesian grid of spacing Δ_s. The coefficient vector $\boldsymbol{\alpha}$ is defined as

$$[\boldsymbol{\alpha}]_n = \frac{V_{\text{cube}}}{V_{\text{voxel}}} \int_V d\mathbf{r}\ \psi_n(\mathbf{r}) A(\mathbf{r}), \tag{4.12}$$

where V_{cube} and V_{voxel} are the volumes of a cubic voxel of dimension Δ_s and a sphere of diameter Δ_s, respectively.

On substitution from Eqn. (4.10) into Eqn. (4.8), one obtains a D-D imaging model

$$\mathbf{u}^a = \mathbf{H}\boldsymbol{\alpha}, \tag{4.13}$$

where $\mathbf{u}^a$ is an approximation of $\mathbf{u}$. The system matrix $\mathbf{H}$ is of dimension $M \times N$ and its elements are given by

$$[\mathbf{H}]_{qK+k,n} = \frac{\beta}{4\pi C_p S_q} h^e(t) *_t \int_{S_q} d\mathbf{r}^s \int_V d\mathbf{r}\ \psi_n(\mathbf{r}) \frac{d}{dt} \frac{\delta(t - \frac{|\mathbf{r}^s - \mathbf{r}|}{c_0})}{|\mathbf{r}^s - \mathbf{r}|} \bigg|_{t=k\Delta_t}. \tag{4.14}$$

For the choice of expansion functions as Eqn. (4.11), it can be verified that

$$\begin{aligned} \frac{\beta}{2C_p} \int_V d\mathbf{r}\ \psi_n(\mathbf{r}) \frac{d}{dt} \frac{\delta(t - \frac{|\mathbf{r}^s - \mathbf{r}|}{c_0})}{|\mathbf{r}^s - \mathbf{r}|} =& -\frac{\beta c_0^3 \pi (t - \frac{|\mathbf{r}^s - \mathbf{r}_n|}{c_0})}{C_p |\mathbf{r}^s - \mathbf{r}_n|} \Big[H(t - \frac{|\mathbf{r}^s - \mathbf{r}_n|}{c_0} + \frac{\Delta_s}{2c_0}) \\ & - H(t - \frac{|\mathbf{r}^s - \mathbf{r}_n|}{c_0} - \frac{\Delta_s}{2c_0}) \Big] \\ =& \frac{p_0(t)}{|\mathbf{r}^s - \mathbf{r}|} *_t \delta(t - \frac{|\mathbf{r}^s - \mathbf{r}_n|}{c_0}), \end{aligned} \tag{4.15}$$

where $H(t)$ is Heaviside step function. The function $p_0(t)$ has an 'N'-shape profile defined as

$$p_0(t) = -\frac{\beta c_0^3 \pi}{C_p} t \Big[H(t + \frac{\Delta_s}{2c_0}) - H(t - \frac{\Delta_s}{2c_0}) \Big] \tag{4.16}$$

The second equality in Eqn. (4.15) was inspired by the impulse response method discribed in Section 4.2, which converts the surface integral in Eqn. (4.14) to a temporal convolution. On substitution from Eqn. (4.15) into Eqn. (4.14), one obtains

$$[\mathbf{H}]_{qK+k,n} = p_0(t) *_t h^e(t) *_t \frac{1}{S_q} h_q^s(\mathbf{r}_n, t)\Big|_{t=k\Delta_t}, \tag{4.17}$$

where $h_q^s(\mathbf{r}_n, t)$ is the SIR defined in Eqn. (4.3) by setting the integral surface to be S_q. Because a variety of methods have been proposed to calculate the SIR in the ultrasound literature [40, 97, 63] , conversion from Eqn. (4.14) to Eqn. (4.17) will facilitate the numerical implementation of the system matrix $\mathbf{H}$.

4.4 Descriptions of Numerical Studies

Numerical studies that employed computer-simulated and experimental PACT measurement data were conducted, as described below, to investigate the use of the proposed D-D imaging model for image reconstruction.

4.4.1 Implementation of the System Matrix

The EIR is determined by the physical properties of the ultrasonic transducer and is more conveniently determined by experiments. In this study, we employed a specific EIR that was measured as described in [22]. A variety of SIR models have been proposed [40, 97, 63] and utilized in studies of PACT [6, 29]. In our numerical studies, we adopted the SIR model

that, for a square transducer of dimension a, is specified as [29]

$$h_q^s(\mathbf{r}_n,t)=\begin{cases}\frac{c_0}{2\pi a^2\sin\theta|\mathbf{r}_n-\mathbf{r}_q^s|}\left[(\frac{\sin\phi}{\cos\phi}+\frac{\cos\phi}{\sin\phi})\frac{c_0}{\sin\theta}(t-\frac{|\mathbf{r}_n-\mathbf{r}_q^s|}{c_0})+\frac{a}{2}(\frac{1}{\cos\phi}+\frac{1}{\sin\phi})\right], & \\ \qquad\qquad\qquad\qquad\qquad\qquad\qquad\qquad \text{for } -t_A\le t<-t_B, \\ \frac{c_0}{2\pi a\sin\theta\cos\phi|\mathbf{r}_n-\mathbf{r}_q^s|}, & \text{for } -t_B\le t<t_B, \\ \frac{c_0}{2\pi a^2\sin\theta|\mathbf{r}_n-\mathbf{r}_q^s|}\left[-(\frac{\sin\phi}{\cos\phi}+\frac{\cos\phi}{\sin\phi})\frac{c_0}{\sin\theta}(t-\frac{|\mathbf{r}_n-\mathbf{r}_q^s|}{c_0})+\frac{a}{2}(\frac{1}{\cos\phi}+\frac{1}{\sin\phi})\right], & \\ \qquad\qquad\qquad\qquad\qquad\qquad\qquad\qquad \text{for } t_B\le t<t_A, \\ 0, & \text{otherwise}\end{cases} \tag{4.18}$$

with

$$t_A=\frac{a}{2c_0}\sin\theta(\cos\phi+\sin\phi), \tag{4.19a}$$

$$t_B=\frac{a}{2c_0}\sin\theta(\cos\phi-\sin\phi), \tag{4.19b}$$

where $\mathbf{r}_q^s$ denotes the location of the center of the q-th transducer, θ and ϕ are functions of both $\mathbf{r}_n$ and $\mathbf{r}_q^s$. As indicated in Fig. 4.1, for each pair of locations $\mathbf{r}_n$ and $\mathbf{r}_q^s$, we defined a local coordinate system whose origin o' was located at $\mathbf{r}_q^s$ and z'-axis was normal to the transducer plane. The direction of the incident wavefield $\hat{\mathbf{k}}$ was defined as

$$\hat{\mathbf{k}}(\mathbf{r}_q^s,\mathbf{r}_n)=\frac{\mathbf{r}_q^s-\mathbf{r}_n}{|\mathbf{r}_q^s-\mathbf{r}_n|}. \tag{4.20}$$

Its projection on the transducer plane was chosen as the x'-axis. The angle θ was the angle between $\hat{\mathbf{k}}$ and z'-axis and $\phi=\min(\phi_1,\phi_2)$, where ϕ_1 and ϕ_2 were the two angles between x'-axis and the transducer's two edges. Equation (4.18) was derived under the farfield assumption, i.e., $|\mathbf{r}_n-\mathbf{r}^s|\approx(\mathbf{r}_n-\mathbf{r}^s)\cdot\mathbf{r}_n/|\mathbf{r}_n|$, for $\mathbf{r}^s\in S_q$.

To obtain the system matrix $\mathbf{H}$, in principle, we need to implement the two continuous convolutions in Eqn. (4.17). However, only discrete samples of $h^e(t)$ are available in practice. Also, the quantity $\frac{1}{S_q}h_q^s(\mathbf{r}_n,t)*_t p_0(t)\equiv l_q(\mathbf{r}_n,t)$ is broadband in temporal frequency space, which may result in strong aliasing if direct temporal sampling was applied. Consequently, an anti-aliasing filter was applied to $l_q(\mathbf{r}_n,t)$ and the first convolution operation in Eqn.

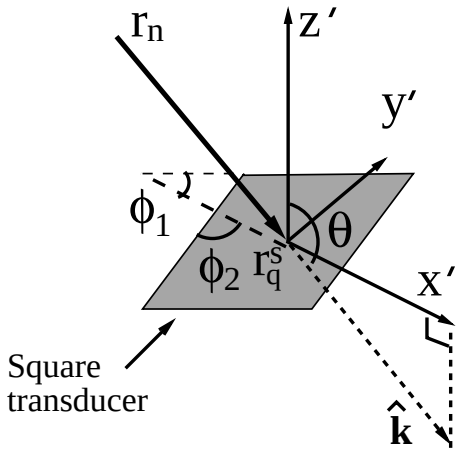

Figure 4.1: Illustration of the dependence of two incident angles θ (elevation) and ϕ (azimuth) on the locations of the photoacoustic source $\mathbf{r}_n$ and the transducer $\mathbf{r}_q^s$. The transducer possesses a flat square detecting surface.

(4.17) was approximated by a discrete convolution as

$$\big[\mathbf{H}\big]_{qK+k,n} \approx \Delta_t \sum_{k'=0}^{K-1} h^e\big((k-k')\Delta_t\big) l'_q(\mathbf{r}_n, k'\Delta_t), \tag{4.21}$$

where $l'_q(\mathbf{r}_n, k\Delta_t)$ is a discrete approximation of $l_q(\mathbf{r}_n, t)$. Additional details regarding implementation of the system matrix are provided in Appendix-A.

To investigate the effects of EIR and SIR seperately, in the following discussion, we denote the comprehensive system matrix by $\mathbf{H}$. Meanwhile, we construct another three system matrices: $\mathbf{H}_0$ that assumes ideal point-like transducers, $\mathbf{H}_e$ that only incorporates the EIR effect, and $\mathbf{H}_s$ that only incorporates the SIR effect. More specifically, these system matrices are defined as

$$[\mathbf{H}_0]_{qK+k,n} = p_0(t) *_t \frac{\delta(t - |\mathbf{r}^s - \mathbf{r}_n|/c_0)}{2\pi|\mathbf{r}^s - \mathbf{r}_n|}\Big|_{t=k\Delta_t}, \tag{4.22a}$$

$$[\mathbf{H}_e]_{qK+k,n} = p_0(t) *_t h^e(t) *_t \frac{\delta(t - |\mathbf{r}^s - \mathbf{r}_n|/c_0)}{2\pi|\mathbf{r}^s - \mathbf{r}_n|}\Big|_{t=k\Delta_t}, \tag{4.22b}$$

$$[\mathbf{H}_s]_{qK+k,n} = p_0(t) *_t \frac{1}{S_q} h_q^s(\mathbf{r}_n, t)\Big|_{t=k\Delta_t}. \tag{4.22c}$$

4.4.2 Eigenanalysis of the System Matrix

To investigate how incorporation of the transducer SIR in the imaging model will affect the numerical stability of the image reconstruction problem, we computed the eigenspectrum of the Hessian matrix $\mathbf{H}_s^\dagger \mathbf{H}_s$. We considered an imaging geometry consisting of 90 square ultrasonic transducers of dimension a that were uniformly distributed on a ring of radius R^s. This geometry is depicted in in Fig. 4.2-(a), and was utilized to image thin 3D objects in the studies described below. We numerically computed the eigenvalues of the Hessian $\mathbf{H}_s^\dagger \mathbf{H}_s$ for different transducer dimensions $a = 0.5, 2,$ and 4-mm and scanning radii $R^s = 25$ and 50-mm, respectively. For comparison, we also computed the eigenvalues of the Hessian $\mathbf{H}_0^\dagger \mathbf{H}_0$ for the ideal case.

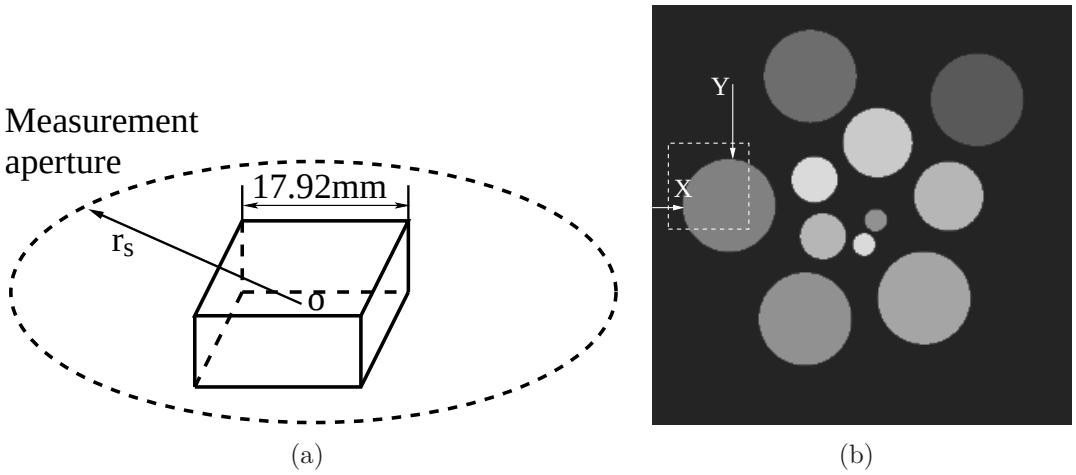

(a) (b)

Figure 4.2: (a) The scanning geometry employed in the computer-simulation studies. (b) The central horizonal slice through the numerical phantom.

4.4.3 Computer-Simulation Studies and Reconstruction Algorithm

Computer-simulated Measurement Data: The 3D numerical phantom shown in Fig. 4.2 was taken to represent the object function $A(\mathbf{r})$. Its support volume was $17.92 \times 17.92 \times 0.07$-mm^3 and was represented by $512 \times 512 \times 2$ non-overlapping spherical voxels of radii 0.0175-mm. From this discrete representation of $A(\mathbf{r})$, the noiseless data $\mathbf{u}^a$ were calculated numerically by use of Eqn. (4.13) at $Q = 360$ equally spaced transducer locations over

the interval $[0, 2\pi)$ on the 2D measurement geometry shown in Fig. 4.2-(a). The scanning radius was 25-mm. At each transducer location, $K = 512$ equally spaced temporal values of the voltage signal over the interval $[8, 25)$-μs were computed. Each transducer had a flat detecting area of dimension 4×4-mm^2 and the speed of sound was described by a constant value $c_0 = 1.521$-mm/μs. The voltage data were generated by use of $\mathbf{H}$ whose $h^e(t)$ was measured experimentally [22, 29] and is displayed in Fig. 4.3.

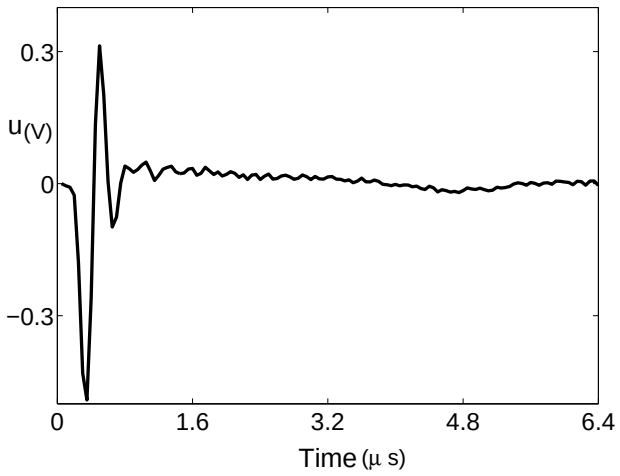

Figure 4.3: The acousto-electrical impulse response of the ultrasonic transducer.

Although the image reconstruction studies described below will employ a different voxel size in the assumed object representation than that employed to generate the measurement data, it should be noted that these computer-simulation studies do not comprehensively assess the impact of modeling errors associated with approximating a C-D imaging model with a D-D one. However, these computer-simulation studies do serve to demonstrate the potential improvement in spatial resolution that can be achieved by incorporation of the transducer response in the imaging model. Also, as described below, these studies will assess the statistical properties of images reconstructed by use of a particular iterative reconstruction algorithm. Images reconstructed from experimental data will corroborate the features revealed by the computer-simulation studies and are discussed later.

Noise model: With consideration of stochastic measurement noise, the detected voltage data can be described as

$$\tilde{\mathbf{u}}^a = \mathbf{u}^a + \tilde{\mathbf{n}}, \tag{4.23}$$

where $\tilde{\mathbf{n}}$ is an additive noise vector. Here, the tilde indicates a stochastic quantity. We focus on the SIR effect and thus $\mathbf{u}^a$ was generated by use of $\mathbf{H}_s$. The noise vector was treated as an uncorrelated zero-mean Gaussian random vector with a standard deviation σ_n chosen according to the rule

$$\sigma_n = 0.03\big[\mathbf{u}^a\big]_{max}, \tag{4.24}$$

where, $\big[\mathbf{u}^a\big]_{max}$ denotes the maximum value of all components of the noiseless $\mathbf{u}^a$. A total of 100 noisy versions of $\tilde{\mathbf{u}}^a$ were computed as realizations of this stochastic process.

Reconstruction Algorithm: From knowledge of the noiseless and noisy simulated measurement data, images were reconstructed by inverting the D-D imaging model in Eqn. (4.13) by solving for a penalized least-squares (PLS) objective [32]. Investigation of alternative objective functions will be discussed in Chapter 5. The optimization problem was formulated as

$$\hat{\boldsymbol{\alpha}} = \arg\min_{\boldsymbol{\alpha}} \|\mathbf{u} - \mathbf{H}\boldsymbol{\alpha}\|^2 + \beta R(\boldsymbol{\alpha}), \tag{4.25}$$

where $R(\boldsymbol{\alpha})$ is a regularizing penalty term whose impact is controlled by the regularization parameter β. In this study we employed a quadratic smoothness penalty given by

$$R(\boldsymbol{\alpha}) = \sum_{n=0}^{N-1} \sum_{k \in \mathcal{N}_n} \Big([\boldsymbol{\alpha}]_n - [\boldsymbol{\alpha}]_k\Big)^2, \tag{4.26}$$

where $\mathcal{N}_n$ is the set of eight neighbors of the n-th voxel. The system matrix $\mathbf{H}$ was constructed according to Eqn. (4.21). For the noiseless voltage data generated by $\mathbf{H}$, we compared the reconstructed images obtained by use of $\mathbf{H}_0$, $\mathbf{H}_e$, $\mathbf{H}_s$, and $\mathbf{H}$. We also investigated the SIR effects in the noisy case where $h^e(t) = \delta(t)$ by comparing the images reconstructed by use of $\mathbf{H}_s$ and $\mathbf{H}_0$.

In all cases, the reconstruction algorithm for implementing Eqn. (4.25) was based on the linear conjugate gradient (CG) method [69, 96, 33]. We calculated the ℓ_2-norm of the gradient and terminated the iteration when it was below a prechosen tolerance. We used the same tolerance in both reconstruction algorithms. The impact of the choice of β on the reconstructed images was studied by Monte Carlo simulations described in the next subsection. The reconstructed object estimates were represented by a $256 \times 256 \times 1$ grid of non-overlapping spherical voxels of radius 0.035-mm.

4.4.4 Empirical Determination of Image Statistics and Resolution Measures

As described above, for each choice of the regularization parameter β, 100 noisy images were reconstructed for the cases where the EIR effect was excluded and the system matrices $\mathbf{H}_s$ and $\mathbf{H}_0$ were employed by the reconstruction algorithm. From each collection of images, the empirical mean image and the empirical estimate of the image variance map were computed by

$$\text{mean}\left\{\left[\hat{\boldsymbol{\alpha}}\right]_n\right\} = \frac{1}{J}\sum_{j=1}^{J}\left[\hat{\boldsymbol{\alpha}}_j\right]_n, \tag{4.27a}$$

$$\text{variance}\left\{\left[\hat{\boldsymbol{\alpha}}\right]_n\right\} = \frac{1}{J-1}\left(\sum_{j=1}^{J}\left[\hat{\boldsymbol{\alpha}}_j\right]_n^{\,2} - \frac{1}{J}\left(\sum_{j=1}^{J}\left[\hat{\boldsymbol{\alpha}}_j\right]_n\right)^2\right), \tag{4.27b}$$

where $J = 100$ is the number of noisy images we reconstructed, $\hat{\boldsymbol{\alpha}}_j$ is the reconstructed image from the j-th realization of noisy data, and n is the voxel index.

We computed the mean variance within a 90×90 voxel region indicated by the dashed box in Fig. 4.2-(b). To quantify the spatial resolution of the reconstructed image, we fitted the rising edge of a prechosen structure in the empirical mean images to a cumulative Gaussian function $C(x)$ as [103]:

$$C(x) = I_1 + \frac{I_2 - I_1}{2}\left(1 + \text{erf}\left(\frac{x-\mu}{\sigma\sqrt{2}}\right)\right), \tag{4.28}$$

where I_1 and I_2 are the true intensities on the two sides of the boundary with $I_1 < I_2$, μ is the true location of the boundary, and $\text{erf}(x)$ is the Gauss error function with the standard deviation denoted by σ The image resolution was characterized by the full width at half-maximum (FWHM) value of the fitted error function [133] as FWHM $= 2\sqrt{2\ln 2}\ \sigma$. We computed the spatial resolutions crossing the two edges marked by the arrows 'X' and 'Y' in Fig. 4.2-(b) that correspond to radial and tangent directions, respectively. The radial and tangent directions are relative to the measurement geometry that was a ring in 2D or a sphere in 3D for this study. Repeating the process for different choices of the regularization parameters β ranging from 0 to 10 produced a collection of (variance, FWHM) pairs, which

were plotted to characterize the tradeoffs between spatial resolution and noise levels in the reconstructed images.

4.4.5 Experimental data

We applied the reconstruction algorithm utilizing the new system matrix $\mathbf{H}$ to experimental data obtained by use of an existing PACT imaging system [14, 15], where the EIR was the same as the one employed in the simulation studies shown in Fig. 4.3. The measurement geometry is shown in Fig. 4.4. The to-be-imaged object consisted of a pair of crossing horse hairs with a thickness of 200-μm and a length of 90-mm mounted on a custom made holder. The laser pulse was of wavelength 765-nm and was delivered by a bifurcated fiber bundle to illuminate the bottom half of the object. Two light beams were expanded to a diameter of 40-mm. A curved transducer array consisting of 64 rectangular detecting elements were focused at 65-mm that approximately coincided with the intersection of the hairs. Each transducer element had a flat detecting surface of size 2×2-mm^2. The object was rotated about the z-axis as indicated in Fig. 4.4, and photoacoustic pressure measurements were obtained at 72 uniformly-spaced views over a 360° interval. The time samples were obtained at 1536 instances at a sampling rate of 20-MHz. We made use of the voltage data obtained by 33 transducers indexed from 31 to 64 shown in Fig. 4.4 for the reconstruction. The region to-be-reconstructed was of size $13.44 \times 5.6 \times 41.44$-mm^3 and was represented by $96 \times 40 \times 296$-voxels. Each voxel was of diameter 0.14-mm. We turned off the smoothness regularization term in Eqn. (5.13), i.e., $\beta = 0$, since the noise level was very low in this data set. For comparison, we also reconstructed images by use of system matrices $\mathbf{H}_e$, and $\mathbf{H}_0$. The algorithms were terminated for all imaging models after six iterations where the objective functions reduced to the same level and the images became noisier for more iterations. The reconstructed 3D image data were visualized by computing maximum intensity projection images by use of the Osirix software [93].

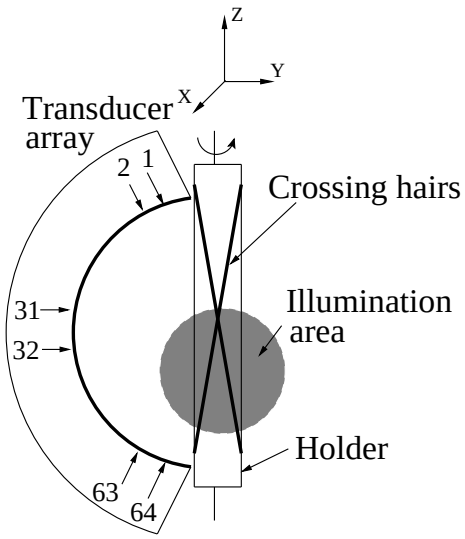

Figure 4.4: The scanning geometry employed in the experimental studies.

4.5 Numerical Results

4.5.1 Intrisic Numerical Properties of H

The eigenvalues of $\mathbf{H}_s^\dagger \mathbf{H}_s$ for the cases of transducer dimensions $a = 0.5$, 2, and 4-mm were numerically computed and plotted in Fig. 4.5. The eigenspectrum of $\mathbf{H}_0^\dagger \mathbf{H}_0$, the Hessian matrix assuming an ideal point-like transducer, was also computed. Figures 4.5-(a) and (b) display the eigenspectra corresponding to cases where the radius of the scanning aperture was $R^s = 25$-mm and 50-mm, respectively. These plots reveal that the rate of decay of the eigenvalues of $\mathbf{H}_s^\dagger \mathbf{H}_s$ increases as the transducer size a is increased. This confirms that the image reconstruction problem becomes more ill-conditioned and is therefore more sensitive to data inconsistencies as the transducer size is increased. Similarly, by comparison of Figs. 4.5-(a) and (b) we observe that the rate of decay of the eigenvalues of $\mathbf{H}_s^\dagger \mathbf{H}_s$ is slower for the larger scanning aperture. This confirms that the ill-conditioning of the reconstruction problem is generally less severe for larger scanning apertures.

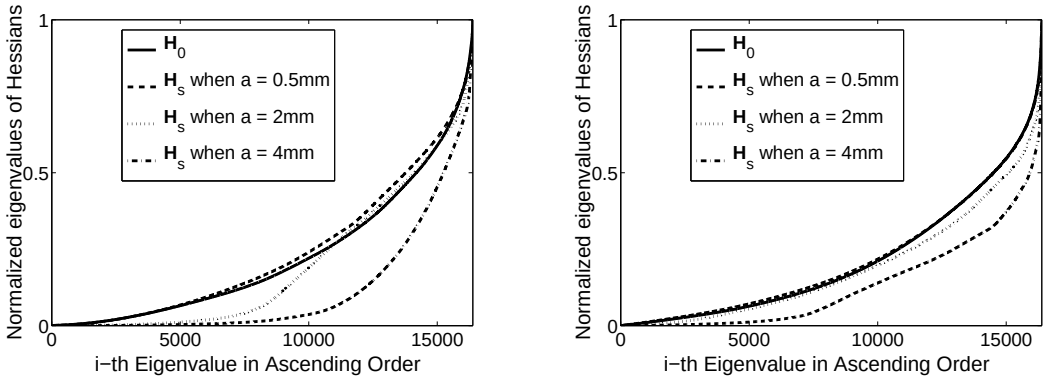

(a) (b)

Figure 4.5: Normalized eigenspectra of the Hessian matrices for the new system matrix $\mathbf{H}_s$, and the system matrix assuming point-like transducer $\mathbf{H}_0$ for different transducer sizes $a = 0.5$, 2, and 4-mm. The scanning radius is (a) $R^s = 25$-mm and (b) $R^s = 50$-mm.

4.5.2 Results from Noiseless Simulation Data

The computer-simulated noiseless data were generated by use of the system matrix $\mathbf{H}$, from which the images reconstructed by use of $\mathbf{H}_0$, $\mathbf{H}_s$, $\mathbf{H}_e$ and $\mathbf{H}$ are shown in Figs. 4.6-(a-d), respectively. We set the regularization parameter $\beta = 0$ for all cases. Reconstruction algorithms were started from the same uniform initial guess and terminated after 150 iterations when the ℓ_2-norms of the objective functions' gradients were reduced by a factor 10^{-5} compared to their initial values. As expected, structures within images reconstructed by use of $\mathbf{H}_s$ had uniformly broadened boundaries while the peripheral structures within images reconstructed by use of $\mathbf{H}_e$ had blurred boundaries along the tangent direction. The images reconstructed by use of $\mathbf{H}_0$ suffer from both degradations. By use of the new system matrix $\mathbf{H}$, the reconstructed images have improved spatial resolution. Ignoring the EIR effect results in the loss of quantitative information of the reconstructed images. Figures 4.6-(a) and (b) contain negative values and are shown in a different gray scale from that employed in Figs. 4.6-(c) and (d). The profiles along the radial and tangent directions, indicated by 'X' and 'Y' in the images in Figs. 4.6-(c) and (d), are shown in Figs. 4.7-(a) and (b).

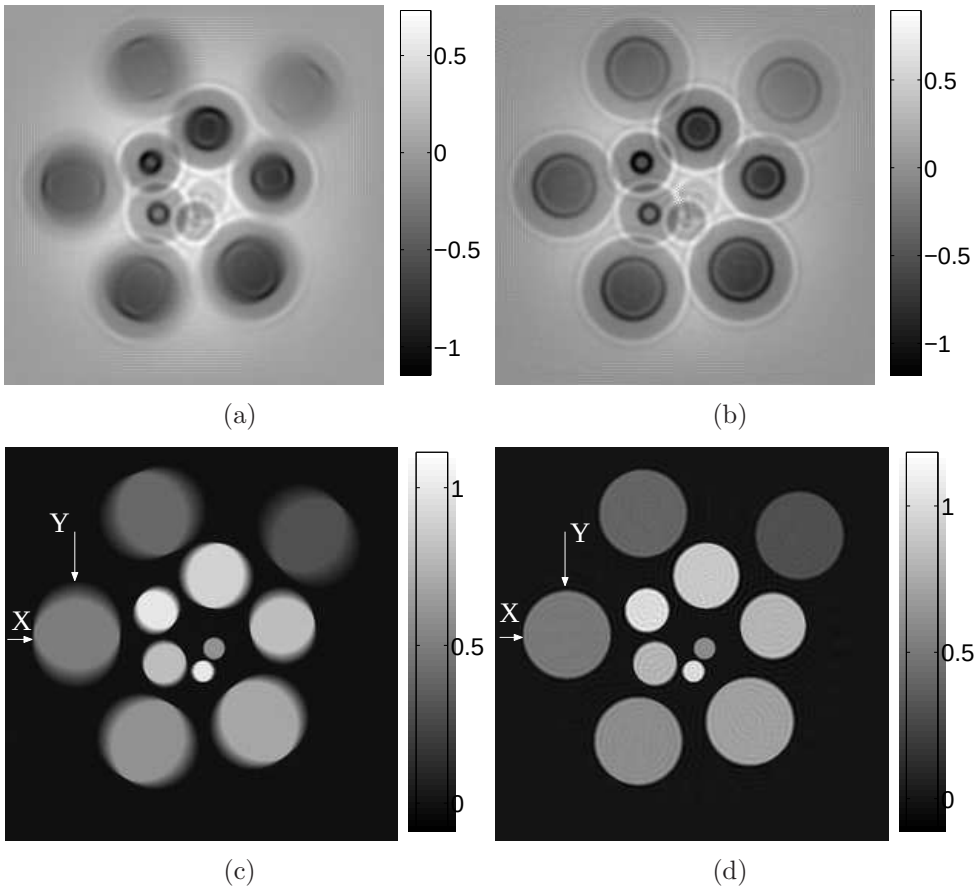

Figure 4.6: Images reconstructed from the noiseless data function $\mathbf{u}^a$ by use of system matrices (a) $\mathbf{H}_0$, (b) $\mathbf{H}_s$, (c) $\mathbf{H}_e$, and (d) $\mathbf{H}$.

4.5.3 Results from noisy simulation data

We simulated the noisy data by use of the system matrix $\mathbf{H}_s$ that assumed $h^e(t) = \delta(t)$. Figures 4.8-(a) and (b) display images reconstructed from noisy simulation data by use of the system matrices $\mathbf{H}_0$ and $\mathbf{H}_s$ with $\beta = 0$. The reconstruction algorithms that employed $\mathbf{H}_0$ and $\mathbf{H}_s$ were terminated at 45 and 54 iterations, respectively, which was when the residues (gradients of the objective functions) were reduced to 0.3% of their initial values. As was observed in the case of noiseless data, structures within the image reconstructed by use of $\mathbf{H}_0$ (Fig. 4.8-(a)) had blurred boundaries, due to the fact that the transducer SIR was not modeled in the system matrix $\mathbf{H}_0$. On the other hand, the spatial resolution of the images reconstructed by use of $\mathbf{H}_s$ (Fig. 4.8-(b)) appear to suffer much less degradation

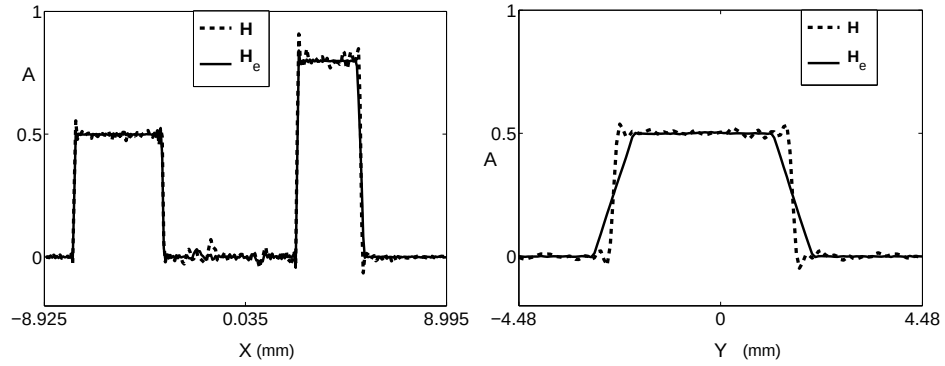

(a) (b)

Figure 4.7: (a) Radial image profiles corresponding to the use of $\mathbf{H}_e$ (solid line) and $\mathbf{H}$ (dashed line). The locations of the profiles are indicated by the 'X'-arrows in Figs. 3.1-(c) and (d), respectively. (d) Tangent image profiles corresponding to the use of $\mathbf{H}_e$ (solid line) and $\mathbf{H}$ (dashed line). The locations of the profiles are indicated by the 'Y'-arrows in Figs. 3.1-(c) and (d), respectively.

in spatial resolution. Additional images reconstructed by use of $\mathbf{H}_s$ with regularization parameters $\beta = 0.5$ and $\beta = 1.0$ are shown in Figs. 4.8-(c) and (d), respectively. As expected, increasing β resulted in a decrease in noise level at the expense of spatial resolution. The root mean square errors of the reconstructed images from the object were calculated within the region of interest marked by the dashed box in Fig. 4.2, which were 6.28, 7.35, 3.91, and 5.07 corresponding to the Figs. 4.8-(a) to (d), respectively. Radial and tangent profiles corresponding to the locations marked 'X' and 'Y' in Figs. 4.8-(a) and (c), are shown in Fig. 4.9.

The curves of the average variance within the specified region-of-interest versus tangential or radial resolution measure for the reconstructed images are shown in Fig. 4.10. The same scanning geometry and acquisition parameters were adopted as described in Section 4.4.3 except that we employed 90 transducers. The left-most point on each curve corresponds to $\beta = 0$. They demonstrate the impact of the regularization parameter β on the tradeoff between the spatial resolution and variance of the reconstructed images. As predicted by the eigenanalysis of the Hessian matrices, for $\beta = 0$ the reconstruction algorithm that employs $\mathbf{H}_s$ produces images with larger variances than those produced by the algorithm employing $\mathbf{H}_0$. However, the spatial resolution of the images produced by the algorithm employing $\mathbf{H}_s$ is superior to those produced by the algorithm employing $\mathbf{H}_0$. When the value of β is

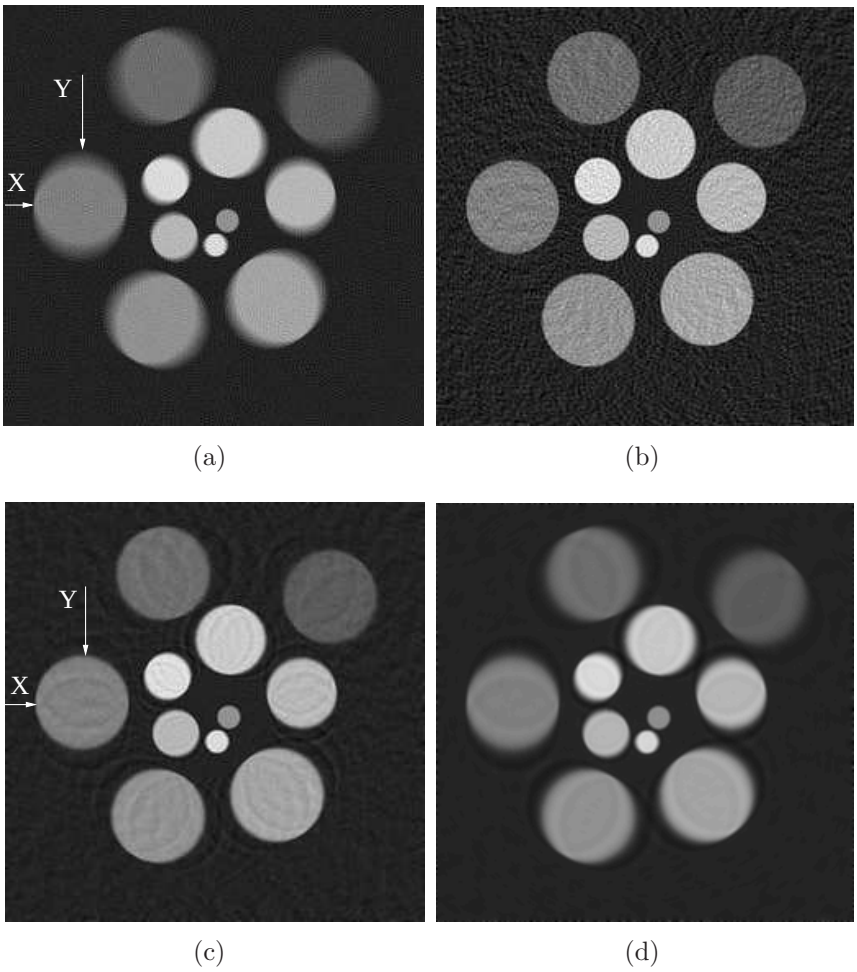

Figure 4.8: Images reconstructed from the noisy data function $\tilde{\mathbf{u}}_a$ by use of (a) $\mathbf{H}_0$, $\beta = 0$, (b) $\mathbf{H}_s$, $\beta = 0$, (c) $\mathbf{H}_s$, $\beta = 0.5$, and (d) $\mathbf{H}_s$, $\beta = 1.0$. The noisy data were degraded only by the SIR.

increased, within the common resolution region of the plot, the curves corresponding to $\mathbf{H}_s$ were lower everywhere than the ones corresponding to $\mathbf{H}_0$. This demonstrates that, when appropriate regularization is employed, an algorithm employing $\mathbf{H}_s$ can produce images with lower noise levels at a matched resolution than can an algorithm employing $\mathbf{H}_0$.

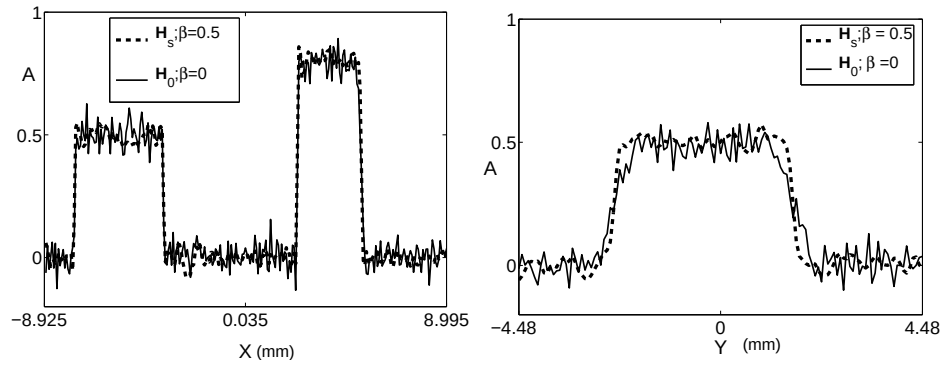

(a) (b)

Figure 4.9: (a) Radial image profiles through the noisy images corresponding to the use of $\mathbf{H}_0$, $\beta = 0$ (solid line) and $\mathbf{H}_s$, $\beta = 0.5$ (dashed line). The locations of the profiles are indicated by the 'X'-arrows in Figs. 4.8-(a) and (c), respectively. (b) Tangent profiles corresponding to the use of $\mathbf{H}_0$, $\beta = 0$ (solid line) and $\mathbf{H}_s$, $\beta = 0.5$ (dashed line). The locations of the profiles are indicated by the 'Y'-arrows in Figs. 4.8-(a) and (c), respectively.

4.5.4 Results from Experimental Data

Figure 4.11 from top to bottom displays reconstructed images of the horse hair phantom corresponding to the planes $y = -5.59$, -3.85, -0.35, and 2.45-mm. The two columns correspond to the use of $\mathbf{H}$ (left) and $\mathbf{H}_e$ (right), respectively, in the reconstruction algorithm. All images were shown in the same display window for comparison. We did not compare them with images reconstructed by use of $\mathbf{H}_0$ because the EIR effect distorted the quantitative values and made them uncomparable in the same grey scale. From Figs. 4.11-(a), (c), (e), and (g) we observed that the thickness of the reconstructed horse hairs was broadened and the intensity was faded for the parts further away from the center of measurement geometry. By use of system matrix $\mathbf{H}$ (see the right column), the structural information of the horse hairs on the peripheral part was preserved. This is consistent with our observations in the computer-simulation studies. Three dimensional rendered images are shown in Fig. 4.12. Figure 4.12-(a), corresponding to $\mathbf{H}_0$, only provided faint structural information while Figs. 4.12-(b) and (c), corresponding to $\mathbf{H}_e$ and $\mathbf{H}$, revealed better-defined structures. Figures 4.12-(b) and (c) employed the same grey scale and display window. These images corrorborate our assertion that compensation for the transducer response in the imaging model can significantly improve the spatial resolution characteristics of the reconstructed image. It is likely that errors in the assumed speed of sound and/or errors in the assumed

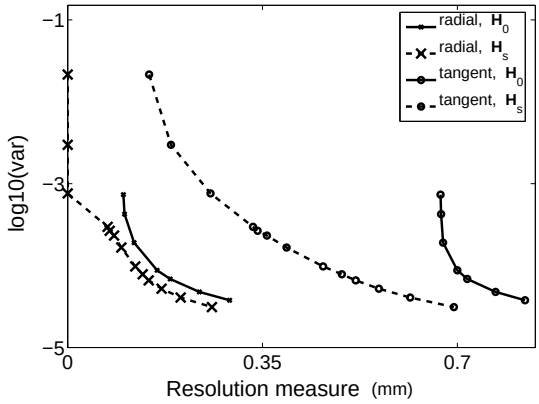

Figure 4.10: Variance vs. resolution curves corresponding to use of the system matrices $\mathbf{H}_s$ and $\mathbf{H}_0$.

location of the center of the scanning geometry limited the achievable spatial resolution of the reconstructed images.

4.6 Summary

Because they provide the opportunity for accurate image reconstruction from incomplete measurement data, iterative reconstruction algorithms for PACT are being developed actively. Iterative reconstruction algorithms permit utilization of imaging models that can accurately describe the measurement process. Despite this, many of the reported PACT image reconstruction algorithms neglect the response of the recording transducer, and relatively little effort in the PACT literature has been devoted towards developing and evaluating detailed imaging models.

In this work, we developed and evaluated an PACT imaging model that incorporates the physical response of an ultrasound transducer. This was accomplished by use of the impulse response method, which is a well-known method for modeling ultrasound transducers using linear acoustics. The imaging model was utilized in conjunction with an iterative algorithm to reconstruct images from computer-simulated and experimental PACT measurement data. These studies confirmed that use of the imaging model in the reconstruction algorithm could significantly improve the spatial resolution of the reconstructed images as compared

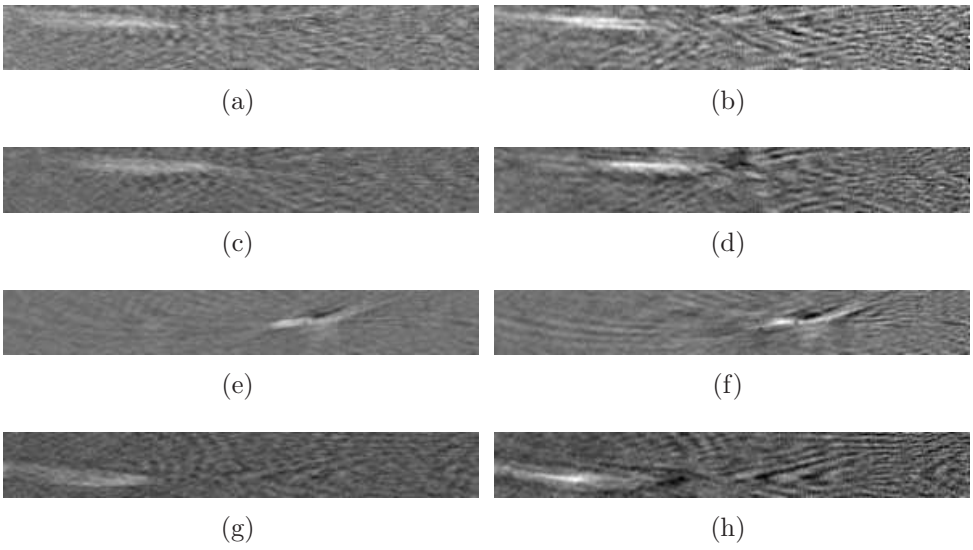

Figure 4.11: Slices through the 3D images reconstucted from the experimental data set. The slices are parallel to the x-o-z plane indicated in Fig. 4.4. The images, from top to bottom, correspond to different locations along y-axis as: (a),(b) $y = -5.95$ mm, (c),(d) $y = -3.85$ mm, (e),(f) $y = -0.35$ mm, and (g),(h) $y = 2.45$ mm. The left column of images corresponds to the use of $\mathbf{H}_e$ while the right column corresponds to the use of $\mathbf{H}$.

to those reconstructed assuming a point-like ultrasound transducer. The proposed imaging model will alleviate the need to utilize small transducers and/or large scanning radii and may permit construction of more compact imaging systems. Compensation for acoustic attenuation and heterogeneities in an object's speed of sound and density may be important in certain applications of PACT. In principle, they can be incorporated into the framework of this study. How to construct the system matrix that accounts for more general acoustic properties of the media remains a topic for future work.

(a) (b) (c)

Figure 4.12: Maximum intensity projection renderings of the experimental phantom image data reconstructed by use of (a) $\mathbf{H}_0$, (b) $\mathbf{H}_e$ and (c) $\mathbf{H}$.

Chapter 5

Investigation of Iterative Image Reconstruction in 3D PACT

5.1 Introduction

A variety of analytic image reconstruction algorithms for three-dimensional (3D) photoacoustic computed tomography (PACT) have been developed [55, 34, 122, 121]. These algorithms are of filtered backprojection forms and assume that the underlying model that relates the object function to measured data is a spherical Radon transform. Analytic image reconstruction algorithms generally possess several limitations that impair their performance. For example, analytic algorithms are often based on discretization of a continuous reconstruction formula and require the measured data to be densely sampled on an aperture that encloses the object. This is problematic for 3D PACT, in which acquiring densely sampled acoustic measurements on a two-dimensional (2D) surface can require expensive transducer arrays and/or long data-acquisition times if a mechanical scanning is employed. Moreover, the simplified forward models, such as the spherical Radon transform, upon which analytic image reconstruction algorithms are based, do not comprehensively describe the imaging physics or response of the detection system [105]. Finally, analytic methods ignore measurement noise and will generally yield images that have suboptimal trade-offs between image variances and spatial resolution. The use of iterative image reconstruction algorithms [31, 1, 69, 87] can circumvent all of these shortcomings.

When coupled with suitable PACT imager designs, iterative image reconstruction algorithms can improve image quality and permit reductions in data-acquistion times as compared with

those yielded by use of analytic reconstruction algorithms. Because of this, the development and investigation of iterative image reconstruction algorithms for PACT [84] is an important research topic of current interest. Recent studies have sought to develop improved discrete imaging models [127, 28, 17, 105] as well as advanced reconstruction algorithms [89, 37, 108]. The majority of these studies utilize approximate 2D imaging models and measurement geometries in which focused transducers are employed to suppress out-of-plane acoustic signals and/or a thin object embedded in an acoustically homogeneous background is employed. Because image reconstruction of extended objects in PACT is inherently a 3D problem, 2D image reconstruction approaches may not yield accurate values of the absorbed optical energy density even when the measurement data are densely sampled. This is due to the fact that simplified 2D imaging models cannot accurately describe transducer focusing and out-of-plane acoustic scattering effects; this results in inconsistencies between the imaging model and the measured data that can result in artifacts and loss of accuracy in the reconstructed images.

Several 3D PACT imaging systems have been constructed and investigated [52, 28, 15]. These systems employ unfocused ultrasonic transducers and analytic 3D image reconstruction algorithms. Only limited studies of the use of iterative 3D algorithms for reconstructing extended objects have been conducted; and these studies employed simple phantom objects [84, 108, 109, 28]. Moreover, iterative image reconstruction in 3D PACT can be extremely computationally burdensome, which can require the use of high performance computing platforms. Graphics processing units (GPUs) can now be employed to accelerate 3D iterative image reconstruction algorithms to the point where they are feasible. However, there remains an important need for the development of accurate discrete image models and image reconstruction algorithms for 3D PACT and an investigation of their ability to mitigate different types of measurement errors found in real-world implementations.

In this chapter, we implement and investigate two 3D iterative image reconstruction methods for use with a small animal PACT imager. Both reconstruction algorithms compensate for the ultrasonic transducer responses but employ different regularization strategies. We compare the different regularization strategies by use of quantitative measures of image quality. Unlike previous studies, we apply the 3D image reconstruction algorithms not only to experimental phantom data but also to the data from a whole-body mouse imaging

experiment. The aim of this study is to demonstrate the feasibility and efficacy of iterative image reconstruction in 3D PACT and to identify current limitations in its performance.

The remainder of the chapter is organized as follows: In Section 5.2, we establish the numerical imaging model that is employed by the iterative image reconstruction algorithms and briefly review the three image reconstruction algorithms. Section 5.3 describes the experimental studies including the data acquisition, implementation details, and approaches for image quality assessment. The numerical results are presented in Section 5.4, and a discussion of our findings is presented in Section 5.5.

5.2 Background: Imaging Models and Reconstruction Algorithms for 3D PACT

Iterative image reconstruction algorithms commonly employ a discrete imaging model that relates the measured data to an estimate of the sought-after object function. In Section 4.3.1, we propose a C-D imaging model that incorporates the characteristics of ultrasonic transducers [105]. A D-D imaging model is constructed to approximate the C-D model in Section 4.3.2. The D-D imaging model was fomulated in time domain while the implementation was conducted in temporal-frequency domain with the aid of fast Fourier transform (FFT) algorithm. In order to gain a more straightfoward interpretation of the imaging model, we reformulate the D-D imaging model in the temporal-frequency domain in Section 5.2.1 for the case of flat rectangular ultrasonic transducers.

5.2.1 Temporal Frequency-Domain Version of the Discrete Imaging Model

Because a transducer's EIR $h^e(t)$ must typically be measured, it generally cannot be described by a simple analytic expression. Accordingly, the two temporal convolutions in Eqn. (4.17) must be approximated by use of discrete time convolution operations. However, both $p_0(t)$ and $h_q^s(\mathbf{r}_n, t)$ are very narrow functions of time, and therefore temporal sampling can result in strong aliasing artifacts unless very high sampling rates are employed. As described

below, to circumvent this we reformulated the D-D imaging model in the temporal frequency domain.

We introduce a function $u_q(t)$ to represent the pre-sampled electric voltage signal corresponding to location index q. By use of $u_q(t)$, the C-D imaging model Eqn. (4.4) can be rewritten as

$$[\mathbf{u}]_{qK+k} = u_q(t)\Big|_{t=k\Delta_t} = h^e(t) *_t \frac{1}{S_q}\int_{S_q} d\mathbf{r}^s\, p(\mathbf{r}^s, t)\Big|_{t=k\Delta_t}. \tag{5.1}$$

In the temporal-frequency domain, Eqn. (5.1) can be expressed as

$$\tilde{u}_q^a(f) = \tilde{p}_0(f)\tilde{h}^e(f)\frac{1}{S_q}\sum_{n=0}^{N-1}\big[\boldsymbol{\alpha}\big]_n \tilde{h}_q^s(\mathbf{r}_n, f), \tag{5.2}$$

where f is the temporal frequency variable conjugate to t and a ' ˜ ' above a function denotes the Fourier transform of that function defined as:

$$\tilde{x}(f) = \int_{-\infty}^{\infty} dt\; x(t)\exp(-\hat{\jmath}2\pi f t). \tag{5.3}$$

For $f \neq 0$, the temporal Fourier transform of $p_0(t)$ is given by

$$\tilde{p}_0(f) = -\hat{\jmath}\frac{\beta c_0^3}{C_p f}\left[\frac{\Delta_s}{2c_0}\cos\big(\frac{\pi f \Delta_s}{c_0}\big) - \frac{1}{2\pi f}\sin\big(\frac{\pi f \Delta_s}{c_0}\big)\right]. \tag{5.4}$$

When the transducer has a flat and rectangular detecting surface of area $a \times b$, under the far-field assumption, the temporal Fourier transform of the SIR is given by [97]:

$$\tilde{h}_q^s(\mathbf{r}_n, f) = \frac{ab\exp(-\hat{\jmath}\,2\pi f\frac{|\mathbf{r}_q^s - \mathbf{r}_n|}{c_0})}{2\pi|\mathbf{r}_q^s - \mathbf{r}_n|}\mathrm{sinc}\Big(\pi f\frac{ax_{nq}^{\mathrm{tr}}}{c_0|\mathbf{r}_q^s - \mathbf{r}_n|}\Big)\mathrm{sinc}\Big(\pi f\frac{by_{nq}^{\mathrm{tr}}}{c_0|\mathbf{r}_q^s - \mathbf{r}_n|}\Big), \tag{5.5}$$

where x_{nq}^{tr} and y_{nq}^{tr} specify the transverse coordinates in a local coordinate system that is centered at the q-th transducer, as depicted in Fig. 5.1, corresponding to the location of a point source described by a 3D Dirac delta function. The SIR does not depend on the third coordinate (z^{tr}) specifying the point-source location due to the far-field assumption. Given the voxel location $\mathbf{r}_n = (x_n, y_n, z_n)$ and transducer location $\mathbf{r}_q^s = (r_q^s, \theta_q^s, \phi_q^s)$, expressed in spherical coordinates as shown in Fig. 5.1, the corresponding values of the local coordinates

can be computed as:

$$x_{nq}^{\mathrm{tr}} = -x_n \cos\theta_q^s \cos\phi_q^s - y_n \cos\theta_q^s \sin\phi_q^s + z_n \sin\theta_q^s, \tag{5.6a}$$

$$y_{nq}^{\mathrm{tr}} = -x_n \sin\phi_q^s + y_n \cos\phi_q^s. \tag{5.6b}$$

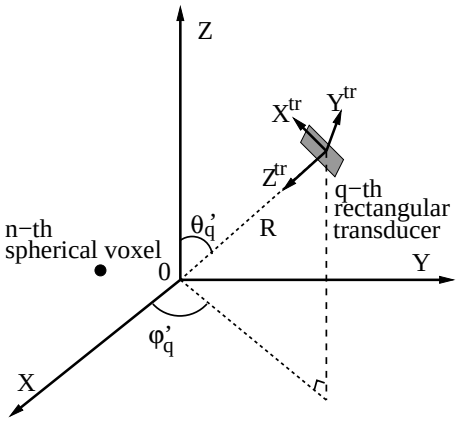

Figure 5.1: Schematic of the local coordinate system for the q-th transducer where the z^{tr}-axis points to the origin of the global coordinate system, the x^{tr} and y^{tr}-axes are along the two edges of the rectangular transducer respectivley.

Equation (5.2) can be discretized by considering L temporal frequency samples specified by a sampling interval Δ_f that are referenced by the index $l = 0, 1, \cdots, L-1$. Utilizing the notation $[\tilde{\mathbf{u}}^a]_{qL+l} = \tilde{u}_q^a(f)\big|_{f=l\Delta_t}$ yields the D-D imaging model:

$$\tilde{\mathbf{u}}^a = \mathbf{H}\boldsymbol{\alpha}, \tag{5.7}$$

where $\mathbf{H}$ is the system matrix of dimension $QL \times N$, whose elements are defined by

$$\big[\mathbf{H}\big]_{qL+l,n} = \tilde{p}_0(f)\tilde{h}^e(f)\frac{\tilde{h}_q^s(\mathbf{r}_n, f)}{ab}\Big|_{f=l\Delta_f}. \tag{5.8}$$

The imaging model in Eqn. (5.7) will form the basis for the iterative image reconstruction studies described in the remainder of the chapter.

5.2.2 Reconstruction Algorithms

We investigated a 3D filtered backprojection algorithm (FBP) and two iterative reconstruction algorithms that employed different forms of regularization.

Filtered Backprojection: A variety of FBP type PACT image reconstruction algorithms have been developed based on the continuous imaging model described by Eqn. (2.1) [55, 34, 122, 121]. If sampling effects are not considered and a closed measurement surface is employed, these algorithms provide a mathematically exact mapping from the acoustic pressure function $p(\mathbf{r}^s, t)$ to the obsorbed energy density function $A(\mathbf{r})$. Since we only have direct access to electric signals in practice, in order to apply FBP algorithms, we need to first estimate the sampled values of the acoustic pressure data from the measured electric signals. In this study, we considered a spherical scanning geometry. For a large scanning radius, when the object is near the center of the measurement sphere, the surface integral over S_q in Eqn. (5.1), i.e., SIR effect, is negligible. The remaining EIR effect is described by a temporal convolution. We employed linear regularized Fourier deconvolution [51] to estimate the pressure data, expressed in temporal frequency domain as:

$$\tilde{p}(\mathbf{r}^s, f) = \frac{\tilde{u}(\mathbf{r}^s, f)}{\tilde{h}^e(f)} \tilde{W}(f), \tag{5.9}$$

where $\tilde{W}(f)$ is a window function for noise suppression. In this study, we adopted the Hann window function defined as:

$$\tilde{W}(f) = \frac{1}{2}\Big[1 - \cos(\pi \frac{f_c - f}{f_c})\Big], \tag{5.10}$$

where f_c is the cutoff frequency. We implemented the following FBP reconstruction formula for a spherical measurement geometry [34]:

$$A(\mathbf{r}) = -\frac{C_p}{2\pi\beta c_0^2 R^s} \int_S d\mathbf{r}^s \, \frac{2p(\mathbf{r}^s, t) + t\frac{\partial}{\partial t} p(\mathbf{r}^s, t)}{|\mathbf{r} - \mathbf{r}^s|} \Bigg|_{t=\frac{|\mathbf{r}-\mathbf{r}^s|}{c_0}}, \tag{5.11}$$

where R^s and S denote the radius and surface area of the measurement sphere respectively. Note that the value of the cutoff frequency f_c controls the degree of noise suppression during the deconvolution, thus indirectly regularizing the FBP algorithm.

Penalized Least-Squares objective with Quadratic Penalty: We employed the least-squares objective regularized by a quadratic penalty. The optimization problem is formulated as

$$\hat{\boldsymbol{\alpha}} = \arg\min_{\boldsymbol{\alpha}} \|\tilde{\mathbf{u}} - \mathbf{H}\boldsymbol{\alpha}\|^2 + \gamma R(\boldsymbol{\alpha}), \tag{5.12}$$

where the regularizing penalty $R(\boldsymbol{\alpha})$ promotes local smoothness whose impact is controlled by the regularization parameter γ. We employed a conventional quadratic smoothness Laplacian penalty given by [31]:

$$\begin{aligned} R(\boldsymbol{\alpha}) = \sum_{n=0}^{N-1} \Bigg\{ &\Big(2[\boldsymbol{\alpha}]_n - [\boldsymbol{\alpha}]_{k_{x_1}} - [\boldsymbol{\alpha}]_{k_{x_2}}\Big)^2 + \Big(2[\boldsymbol{\alpha}]_n - [\boldsymbol{\alpha}]_{k_{y_1}} - [\boldsymbol{\alpha}]_{k_{y_2}}\Big)^2 \\ &+ \Big(2[\boldsymbol{\alpha}]_n - [\boldsymbol{\alpha}]_{k_{z_1}} - [\boldsymbol{\alpha}]_{k_{z_2}}\Big)^2 \Bigg\}, \end{aligned} \tag{5.13}$$

where k_{x_1} and k_{x_2} were the indices of the two neighbor voxels before and after the n-th voxel along x-axis. Similarly, k_{y_1}, k_{y_2} and k_{z_1}, k_{z_2} were the indices of the neighbor voxels along y- and z-axis respectively. The optimization algorithm for solving Eqn. (5.12) was based on the linear conjugate gradient (CG) method [69, 96, 33], and will be referred to as the PLS-Q algorithm.

Penalized Least-Squares objective with Total Variation Norm Penalty: We also investigated the least-squares objective regularized by a TV-norm penalty. The optimization problem is formulated as:

$$\hat{\boldsymbol{\alpha}} = \arg\min_{\boldsymbol{\alpha}\geq 0} \|\tilde{\mathbf{u}} - \mathbf{H}\boldsymbol{\alpha}\|^2 + \beta|\boldsymbol{\alpha}|_{\mathrm{TV}}, \tag{5.14}$$

where β is the regularization parameter, and a non-negativity constraint is employed. The TV-norm is defined as

$$|\boldsymbol{\alpha}|_{\text{TV}} = \sum_{n=0}^{N-1} \sqrt{\Big([\boldsymbol{\alpha}]_n - [\boldsymbol{\alpha}]_{k_{x_1}}\Big)^2 + \Big([\boldsymbol{\alpha}]_n - [\boldsymbol{\alpha}]_{k_{y_1}}\Big)^2 + \Big([\boldsymbol{\alpha}]_n - [\boldsymbol{\alpha}]_{k_{z_1}}\Big)^2}. \tag{5.15}$$

We implemented the fast iterative shrinkage/thresholding algorithm (FISTA) to solve Eqn. (5.14) [10], which will be referred to as PLS-TV algorithm. Implementation of the FISTA algorithm is described in Appendix B.

5.3 Descriptions of Numerical Studies

5.3.1 Experimental Data Acquisition

Scanning Geometry: The experimental data employed in our studies were acquired by TomoWave Laboratories, Houston, TX. The small animal PACT imager has been described in previous publications [29, 14, 15]. As illustrated in Fig. 5.2-(a), the arc-shaped probe consisted of 64 transducers that spanned 152° over a circle of radius 65-mm. Each transducer possessed a square detecting area of size 2×2-mm^2. The laser illuminated the object from rectangular illumination bars in orthogonal mode. During scanning, the object was mounted on the object holder and rotated over the full 360° while the probe and light illumination stayed stationary. Scans were set to sample at 20-MHz over 1536 samples with an amplification of 60-dB and 64 averages per acquisition.

Six-tube Phantom: A physical phantom was created that contained three pairs of poly-tetrafluoroethylene thin walled tubing of 0.81-mm in diameter that were filled with different concentrations of nickel sulfate solution having absorption coefficient values of 5.681-cm^{-1}, 6.18-cm^{-1}, and 6.555-cm^{-1}. The tubes were held within a frame of two acrylic discs of 1" diameter that were separated at a height of 3.25" and kept attached by three garolite rods symmetrically spaced 120° apart. The tubing was such that each pair would contain a tube that would follow along the outside of the phantom and the second would be diagonally inside. A photograph of the phantom is shown in Fig. 5.2-(b). The entire phantom was

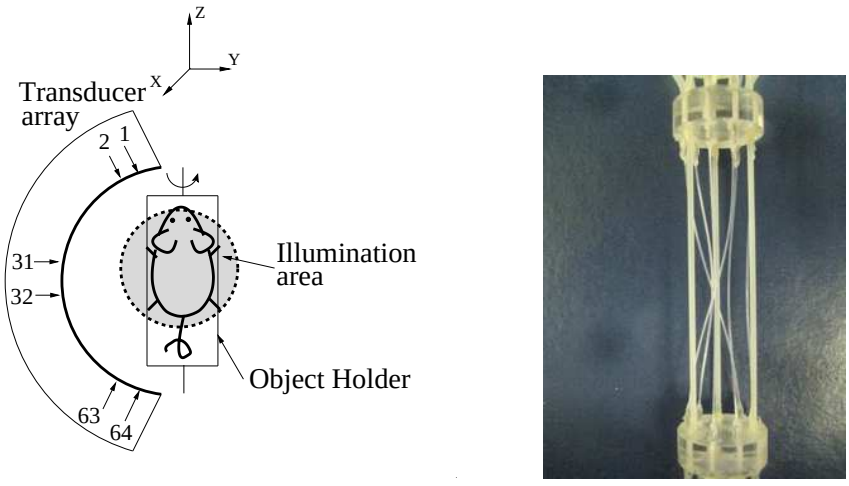

(a) (b)

Figure 5.2: (a) Schematic of the 3D PACT scanning geometry; (b) Photograph of the six-tube phantom.

encased inside a thin latex membrane that was filled with skim milk to create an optically scattering medium. A titanium sapphire laser with a peak at 765-nm and a pulse width of 16-ns (Quanta Systems) were employed to irradiate the phantom. The temperature of the water bath was kept at approximately 29.5°C with a water pump and heater. A complete tomographic data set was acquired by rotating the object about 360° in 0.5° steps. Accordingly, data were recorded by each transducer on the probe at 720 tomographic view angles about the vertical axis.

Whole-Body Mouse Imaging: A 6 to 7 week old athymic Nude-Foxn1^{nu} live mouse (Harlan, Indianapolis, Indiana) was imaged with a similar setup to the phantom scan with a customized holder that provided air to the mouse when it was submerged in water. The holder was essentially comprised of three parts: 1) a hollow acrylic cylinder for breathing, 2) an acrylic disc with hole for mouse tail and an apparatus to attach the legs, and 3) pre-tensioned fiber glass rods to connect the two acrylic pieces. The mouse was given pure oxygen with a flow rate of 2-L/min with an additional 2% isoflurane concentration for initial anesthesia. During scanning the isoflurane was lowered to be around 1.5%. The temperature of water was held constant at 34.7°C with the use of a PID temperature controller connected to heat pads (Watlow Inc., Columbia, MO) underneath the water tank. A bifurcated optical

fiber was attached to a ND:YAG laser (Brilliant, Quantel, Bozeman, MT) operating at 1064-nm wavelength with a energy pulse of about 100-mJ during scans and a pulse duration of 15-ns. The optical fiber outputs were circular beams of approximately 8-cm at the target with an estimated 25-mJ directly out of each fiber. Illumination was done in orthogonal mode along the sides of the water tank with in width of 16". A complete tomographic data set was acquired by rotating the object about 360° in 2° steps. Accordingly, data were recorded by each transducer on the probe at 180 tomographic view angles about the vertical axis. More details regarding the data acquisition procedure can be found in [14, 15].

5.3.2 Implementation of Reconstruction Algorithms

Six-Tube Phantom: The region to-be-reconstructed was of size $19.8 \times 19.8 \times 50.0$-mm^3 and centered at $(-1.0, 0, -3.0)$-mm. The FBP algorithm was employed to determine estimates of $A(\mathbf{r})$ that were sampled on a 3D Cartesian grid with spacing 0.1-mm by use of a discretized form of Eqn. (5.11). The iterative reconstruction algorithms employed spherical voxels of 0.1-mm in diameter inscribed in the cuboids of the Cartesian grid. Accordingly, the reconstructed image matrices for all three algorithms were of size $198 \times 198 \times 500$. The speed-of-sound was set at $c_0 = 1.47$-mm/μs. We selected the Grüneisen coefficient as $\Gamma = \beta c^2/C_p = 2,000$ of arbitrary units for all implementations. Since the top and bottom transducers received mainly noise for elongated structures that were aligned along z-axis, we utilized only the data that were acquired by the central 54 transducers.

Whole-Body Mouse Imaging: The region to-be-reconstructed was of size $29.4 \times 29.4 \times 61.6$-mm^3 and centered at $(0.49, 2.17, -2.73)$-mm. The FBP algorithm was employed to determine estimates of $A(\mathbf{r})$ that were sampled on a 3D Cartesian grid with spacing 0.14-mm by use of Eqn. (5.11). The iterative reconstruction algorithms adopted spherical voxels of 0.14-mm in diameter inscribed in the cuboids of the Cartesian grid. Accordingly, the reconstructed image matrices for all three algorithms were of size $210 \times 210 \times 440$. The speed-of-sound was chosen as $c_0 = 1.54$-mm/μs. We selected the Grüneisen coefficient as $\Gamma = \beta c^2/C_p = 2,000$ of arbitrary units for all implementations. We utilized only the data that were acquired by the central 54 transducers.

Parallel Programming by CUDA GPU Computing: Three-dimensional iterative image reconstruction is computationally burdensome in general. It demands even more computation when utilizing the system matrix defined by Eqn. (5.8), as opposed to the conventional spherical Radon transform model, mainly because the former accumulates contributions from more voxels to compute a single data sample. In addition, calculation of the SIR defined by Eqn. (5.5) introduces extra computation. It can take weeks to accomplish a single iteration by sequential programming using a single CPU, which is infeasible for practical applications. Because the calculation of SIR for each pair of transducer and voxel is mutually independent, we parallelized the SIR calculation by use of GPU computing with CUDA [98, 20] such that multiple SIR samples were computed simultaneously, dramatically reducing the computational time. The six-tube phantom data were processed by use of 3 NVIDIA Tesla C2050 GPU cards, taking 4.52-hours for one iteration from the data set containing 144 tomographic views, while the mouse-imaging data were processed by use of 6 NVIDIA Tesla C1060 GPU cards, taking 5.73-hours for one iteration from the data set containing 180 tomographic views. Though for testing we let the reconstruction algorithms iterate for over 100 iterations, both PLS-Q and PLS-TV usually converged within 20 iterations. More details regarding the GPU-based implementations are provided in Chapter 6.

5.3.3 Image Quality Assessment

Visual Inspection: We examined both the 3D images and 2D sectional images. To avoid misinterpretations due to display colormap, we compared grayscale images. Also, for each comparison, we varied the grayscale window to ensure the observations are minimally dependent on the display methods. For each algorithm we reconstructed a series of images corresponding to different values of regularization parameter over a wide range. To understand how image intensities are affected by the choice of regularization parameter, each 2D sectional image was displayed in the grayscale window that spanned from the minimum to the maximum of the determined image intensities.

It is more challenging to fairly compare 3D images by visual inspection. Hence we intended not to draw conclusions on which algorithm was superior, but instead to reveal the similarities among algorithms when data were densely sampled. Although for each reconstruction algorithm we reconstructed a series of images corresponding to the values of regularization

parameter over a wide range, the main structures within the images appeared very similar in general. Thus we selected a representitive 3D image for each reconstruction algorithms. These representative images correspond to the regularization parameters whose values were near the center of the full ranges and have a very close range of image intensities. We displayed these images in the same grayscale window. For a prechosen grayscale window $[\alpha_{\text{low}}, \alpha_{\text{up}}]$, the reconstructed images were truncated as:

$$[\boldsymbol{\alpha}^{\text{disp}}]_n = \begin{cases} \alpha_{\text{low}}, & \text{if } [\boldsymbol{\alpha}]_n < \alpha_{\text{low}} \\ \alpha_{\text{up}}, & \text{if } [\boldsymbol{\alpha}]_n > \alpha_{\text{up}} \\ [\boldsymbol{\alpha}]_n, & \text{otherwise.} \end{cases} \tag{5.16}$$

The truncated data were linearly projected to the range $[0, 255]$ as 8-bit unsigned integers:

$$[\boldsymbol{\alpha}^{\text{int8}}]_n = \text{round}\Big(- \frac{255}{\alpha_{\text{up}} - \alpha_{\text{low}}} ([\boldsymbol{\alpha}^{\text{disp}}]_n - \alpha_{\text{low}}) \Big). \tag{5.17}$$

The 3D image data $\boldsymbol{\alpha}^{\text{int8}}$ were visualized by computing maximum intensity projection (MIP) images by use of the Osirix software [93].

Quantitative Metrics: Because the six-tube phantom contained nickel sulfate solution as the only optical absorber, the tubes were interpreted as signals in the reconstructed images, which were contaminated by random noise, e.g., the electronic noise. Since the tubes were immersed in nearly pure scattering media, the reconstructed images were expected to have zero-mean background. In contrary, the whole-body mouse imaging possessed a nonzero-mean background because the absorbing capillaries within blood-rich structures were beyond the 0.5-mm resolution limit [15] of the imaging system, resulting a diffuse background. Consequently, we interpreted the arteries and veins as signals, which were immersed in nonzero-mean background plus random noise.

Image Resolution: Because both the tubes and blood vessels were fine threadlike objects, we quantified the spatial resolution by their thickness. To estimate the thickness of a threadlike object lying along z-axis at certain height, we first selected the 2D sectional image at that height. Subsequently, we truncated the 2D image into dimension of $(2N_r + 1)$-by-$(2N_r + 1)$ pixels; and adjusted the location of the truncated image such that only a continuous group of pixels corresponding to the structure of interest, or hot spot, was present at the center.

We then fitted the 2D sectional image to a 2D Gaussian function given by:

$$G[n_1, n_2] = G[0, 0] \exp(-\frac{n_1^2 + n_2^2}{2\sigma_r^2}), \tag{5.18}$$

where n_1 and n_2 denoted the indices of pixels in the 2D digital image with $n_1, n_2 = -N_r, -N_r + 1, \cdots, N_r$ in units of pixel size, $G[0, 0]$ was the peak value of the Gaussian function located in the center, and σ_r was the standard deviation of the Gaussian function to be estimated. We let $N_r = 15$ and $N_r = 10$ for the six-tube phantom and the mouse imaging respectively. Finally, the estimated σ_r was converted to full width at half maximum (FWHM) as the spatial resolution measure, i.e.,

$$\text{FWHM} = 2\sqrt{2 \ln 2}\sigma_r. \tag{5.19}$$

Contrast-to-noise ratio (CNR): For a prechosen structure, a series of adjacent 2D sectional images were selected along the structure (i.e, along z-axis) as described above. We collected the central voxel of each 2D image, forming the signal region-of-interest (s-ROI). The signal intensity was calculated as:

$$\bar{\boldsymbol{\alpha}}^s = \frac{1}{N^s} \sum_{n=0}^{N^s-1} [\boldsymbol{\alpha}^s]_n, \tag{5.20}$$

where N^s denoted the total number of voxels within the s-ROI. For the six-tube phantom, the s-ROI for each tube contained $N^s = 200$ voxels that extended from $z = -10.4$-mm to $z = 9.6$-mm, while for the mouse-imaging study, the s-ROI for the vessel under study contained $N^s = 20$ voxels that extended from $z = 7.0$-mm to $z = 9.8$-mm. For each s-ROI, we defined a background region-of-interest (b-ROI) that has the same dimension along z-axis as the s-ROI. For the six-tube phantom, we randomly selected 50 voxels at every height that were within a circle of radius 5-mm centered at the hot spot of the signal. Similarly, for the mouse-imaging study, we randomly selected 15 voxels at every height that were within a circle of radius 2.1-mm centered at the hot spot of the signal. Correspondingly, the b-ROI contained $N^b = 10,000$ and $N^b = 300$ voxels for the six-tube phantom and the mouse-imaging study, respectively. The background intensity was calculated by:

$$\bar{\boldsymbol{\alpha}}^b = \frac{1}{N^b} \sum_{n=0}^{N^b-1} [\boldsymbol{\alpha}^b]_n. \tag{5.21}$$

Also, the background standard deviation was calculated by:

$$\sigma_b = \sqrt{\frac{1}{N^b - 1} \sum_{n=0}^{N^b-1} \left([\boldsymbol{\alpha}^b]_n - \bar{\boldsymbol{\alpha}}^b \right)^2}. \tag{5.22}$$

Because the reconstructed image is not a realization of an ergodic random process, the value of σ_b estimated from a single reconstructed image is not equivalent to the standard deviation of the ensemble of images reconstructed by use of a certain reconstruction algorithm. Nevertheless, the σ_b can be employed as a summary measure of the noise level in the reconstructed images. Consequently, the contrast-to-noise ratio (CNR) was calculated by:

$$\text{CNR} = \frac{|\bar{\boldsymbol{\alpha}}^s - \bar{\boldsymbol{\alpha}}^b|}{\sigma_b}. \tag{5.23}$$

Plot of resolution against standard deviation: All three reconstruction algorithms possess regularization parameters that control the trade-offs among multiple aspects of image quality. A plot of resolution against standard deviation evaluates how much spatial resolution is degraded by a regularization method during its noise suppression. To obtain this plot for each reconstruction algorithm, we swept the value of the regularization parameter. For each value, we reconstructed 3D images and quantified the spatial resolution and noise level by use of Eqns. (5.19) and (5.22) respectively. The FWHM values calculated along the structure of interest were averaged as a summary measure of resolution, denoted by $\overline{\text{FWHM}}$. The average was conducted over 20-mm and 2.8-mm for the six-tube phantom and the mouse imaging respectively. The $\overline{\text{FWHM}}$ was plotted against the standard deviation (σ_b).

Plot of signal intensity against standard deviation: In addition to the trade-off between resolution and standard deviation, regularization parameters also control the trade-off between bias and standard deviation. In general, stronger regularization may introduce higher bias while more effectiviely reducing the variance of the reconstructed image. Because the true values of absorbed energy density were unavailable, we plotted the signal intensity against the image standard variation that were calculated by use of Eqns. (5.20) and (5.22). From this plot, we compared the noise level of the reconstructed images with comparable image intensities and hence with comparable biases.

5.4 Experimental Results

The data for the six-tube phantom and whole-body mouse imaging were collected at 720 and 180 view angles respectively, and will be referred to as 'full' data sets. In order to emulate the scans with reduced numbers of views, we undersampled the 'full' data sets to subsets with different numbers of view angles that were evenly distributed over 2π. These subsets will be referred to as 'N-view data' sets, where N is the number of view angles.

5.4.1 Six-Tube Phantom

Visual Inspection of Reconstructed Images from Densely-Sampled Data Sets: From densely-sampled data sets, the MIP images corresponding to the FBP and the PLS-TV algorithms appear to be very similar as shown in Fig. 5.3. Note that the two images were reconstructed from different data sets: The image reconstructed by use of the FBP algorithm is from the full data set, i.e., the 720-view data set, while the one reconstructed by use of the PLS-TV algorithm is from the 144-view data set. We did not apply iterative reconstruction algorithms to the 720-view data set mainly because of the computational burden. Moreover, the images reconstructed from the 144-view data set by use of the PLS-TV algorithm already appear to be at least comparable with those reconstructed by use of the FBP algorithm from full data set. Certain features are shared by both images. For example, both images contain two tubes (indicated by white arrows) that are brighter than the others, which is consistent with the fact that these two tubes are filled with the solution of higher absorption coefficient ($\mu_a = 6.555\text{-cm}^{-1}$). The similarities between the two images are not surprising for two reasons: Firstly, when the pressure function is densely sampled and the object is near the center of the measurement sphere, where the SIR can be neglected, we would expect all three algorithms to perform similarly because the imaging models they are based upon are equivalent in the continuous limit; Also the process of forming the MIP images strongly attenuates the background artifacts.

However, 2D sections of the 3D images reveal cerrtain favorable characteristics of the PLS-TV algorithm, as shown in Fig. 5.4. Though we varied the cutoff frequency f_c over a wide range for the FBP algorithm, none of these images has background as clean as the image

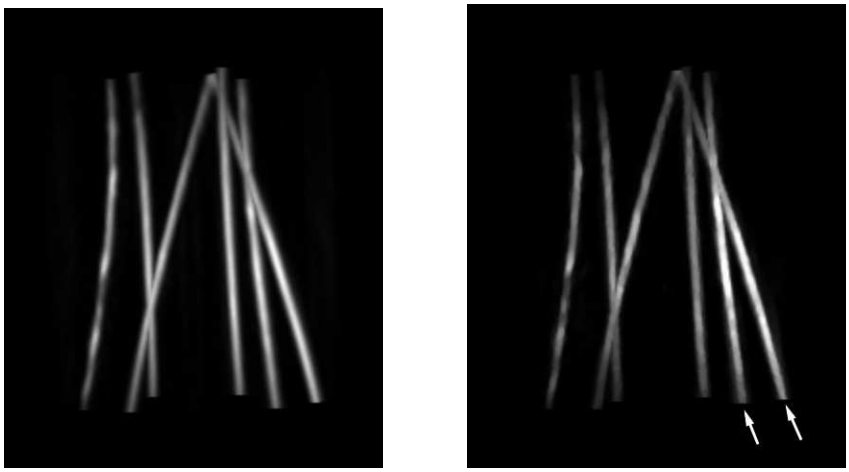

(a) (b)

Figure 5.3: MIP renderings of the six-tube phantom images reconstructed (a) from the 720-view data by use of the FBP algorithm with $f_c = 6$-MHz; and (b) from the 144-view data by use of the PLS-TV algorithm with $\lambda = 0.1$. The grayscale window is [0,7.0]. Two arrows indicate the two tubes that were filled with the solution of the highest absorption coefficient 6.555-cm^{-1}.

reconstructed by the PLS-TV algorithm. We notice two types of artifacts in the images reconstructed by use of the FBP algorithm: the random noise and the radial streaks centered at the tubes. The former is caused by measurement noise while the latter is likely due to certain unmodeled system inconsistencies that are referred to as systematic artifacts and will be addressed in Section 5.5. The regularizing low-pass filter mitigates the random noise but also degrades the spatial resolution (Fig. 5.4-b-e). The TV-norm regularization mitigates the background artifacts with minimal sacrifice in spatial resolution. The image reconstructed by use of the PLS-TV algorithm shown in Fig. 5.4-(f) has at least comparable resolution as that of the FBP image with $f_c = 6$-MHz (Fig. 5.4-c).

Qualitative Comparison of Regularization Methods: The three reconstruction algorithms are regularized by use of the low-pass filter, the ℓ_2-norm smoothness penalty and the TV-norm penalty, respectively. The impacts of the low-pass filter are revealed in Fig. 5.4. We observe that a slight regularization (i.e., a large value of f_c) results in sharp but noisy images while a heavy regularization (i.e., a small value of f_c) produces clean but blurry images. Also, the intensities of the tubes are lower for a smaller value of f_c. Similar effects

are observed for the PLS-Q algorithm with the ℓ_2-norm smoothness penalty as shown in Fig. 5.6. These observations agree with the conventional understandings of the impacts of regularization summarized as two trade-offs: resolution versus variance and bias versus variance [31]. The TV-norm regularization, however, mitigates the image variance with minimal sacrifice in image resolution as shown in Fig. 5.5. Though the signal intensity is reduced at $\beta = 0.1$ (Fig. 5.5-c and -f), the spatial resolution appears to be very close to that of the images corresponding to smaller values of β (Fig. 5.5-a and -d). In addition, both the low-pass filter and the ℓ_2-norm penalty have little effects on the systematic artifacts while the TV algorithm effectively mitigates both the systematic artifacts and the random measurement noise.

Tradeoff Between Signal Intensity and Noise Level of Reconstructed Images: The image intensities in tube-A are plotted as a function of z, as shown in Fig. 5.7 where the location of tube-A is indicated in the 2D image slices as shown in Figs. 5.4 and 5.5. The profiles corresponding to the FBP algorithm were extracted from images reconstructed from the 720-view data set while the profiles corresponding to iterative algorithms were extracted from images reconstructed from the 144-view data set. For each reconstruction algorithm, two profiles are plotted that correspond to moderate and strong regularization as displayed in Fig. 5.7-(a) and (b) respectively. As expected, the quantitative values are smaller when the algorithms are heavily regularized. More importantly, images reconstructed by use of iterative image reconstruction algorithms quantitatively match with those reconstructed by use of FBP algorithm from densely sampled data. In addition, the signal intensities vary gradually along z-axis because the laser was illuminated from the side resulting a higher energy distribution near the center of z-axis. These plots demonstrate the effectiveness of PLS-TV algorithm when the object is not piecewise constant.

From the same data sets, the signal intensities are plotted against the image standard deviations in Fig. 5.8-(a). This plot suggests that the images reconstructed by use of the PLS-TV algorithm have smaller standard deviation while sharing the same bias as those of images reconstructed by use of the FBP and the PLS-Q algorithms because the same signal intensity indicates the same bias. Note that these curves were obtained from densely sampled data. Visual inspections suggest the systematic artifacts contribute more to the background standard deviation measure than does the measurement random noise. Hence, to be more

precise, this plot demonstrates the PLS-TV algorithm outperforms the FBP and the PLS-Q algorithms in the sense of balancing the tradeoff between bias and standard deviation when the signal is present in a uniform background.

Tradeoff Between Resolution and Noise Level of Reconstructed Images: The plots of resolution ($\overline{\text{FWHM}}$) against background standard deviation measure (σ_b) are shown in Fig. 5.8-(b). Clearly, the spatial resolution of the images reconstructed by use of the PLS-TV algorithm is higher than that of the images reconstructed by the FBP and the PLS-Q algorithms while the images having the same background standard deviation. In addition, the curve corresponding to the PLS-TV algorithm is flatter than those corresponding to the FBP and PLS-Q algorithm, suggesting that TV regularization mitigates image noise with minimal sacrifice in spatial resolution. This observation is consistent with our earlier visual inspections of the reconstructed images. It is also interesting to note that the curve corresponding to the PLS-Q algorithm intersects the one corresponding to the FBP algorithm, indicating that conventional iterative reconstruction algorithms may not always outperform the FBP algorithm.

Reconstructed Images from Sparsely-Sampled Data Sets: Images reconstructed from the 72-view data set and the 36-view data set are displayed in Figs. 5.9 and 5.10 respectively. The regularization parameters were selected such that the quantitative values of the images are within the similar range. As expected, from both data sets, the images reconstructed by use of PLS-TV algorithm appear to have higher spatial resolution as well as cleaner backgrounds, suggesting the PLS-TV algorithm can effectively mitigate data incompleteness in 3D PACT.

5.4.2 Whole-Body Mouse Imaging

Visual Inspection of Reconstructed Images from Densely-Sampled Data Sets: From the 180-view data set, the MIP images corresponding to the FBP and the PLS-TV algorithms appear to be very similar as shown in Fig. 6.7. In contrast to the images of the six-tube phantom that have a uniform background, the whole-body mouse images have

a diffuse background. The diffuse background is due to the measurement random noise as well as the capillaries that are beyond the resolution limit of the imaging system [15], thus carrying little information regarding the object. In general, the images reconstructed by the PLS-TV algorithm appear to have a cleaner background while revealing a sharper appearing body vascular tree. Besides, the left kidney in the images reconstructed by use of the PLS-TV algorithm appears to have a higher contrast than the image reconstructed by use of the FBP algorithm. In addition, comparing with the images reconstructed by use of direct backprojection from the raw data, (see figure 6 in [14]), both our algorithms appear to improve the continuity of blood vessels. We believe this is because our algorithms are based on an imaging model that incorporates the transducer SIR and EIR.

Additional details are revealed in the 2D sectional images as shown in Figs. 5.12 and 5.13. Obviously, the contrast of the blood vessels in the images reconstructed by use of the PLS-TV algorithm are higher than those reconstructed by use of the FBP algorithm. In particular, the PLS-TV algorithm significantly enhanced the appearance of peripheral blood vessels. For example, within the ROI A in Fig. 5.12, two blood vessels B and C can be detected easily as two bright spots in zoomed-in image A. However, the two bright spots have much lower visual contrast in the images reconstructed by use the FBP algorithm. In addition, as shown in Fig. 5.13, the PLS-TV algorithm effectively mitigates the foggy background as well as noise with minimal sacrifice in image resolution. However, none of the images reconstructed by use the FBP algorithm has a background as clean as the images reconstructed by the PLS-TV algorithm.

Qualitative Comparison of Regularization Methods: Figures. 5.12 and 5.13 demonstrate how the low-pass filter regularizes the FBP algorithm. Similar to the observations from the six-tube phantom, a large value of f_c results in high spatial resolution, large signal intensities, and high noise level. For the PLS-TV algorithm, besides the image corresponding to $\beta = 0.05$ shown in Fig. 5.12-(d), images corresponding to $\beta = 0.01$ and $\beta = 0.1$ are displayed in Fig. 5.14. Though the TV regularization also suppresses the background variance as well as the signal intensities when the regularization is enhanced, the TV regularization results in minimal sacrifice in spatial resolution.

Trade-Off Between Signal Intensity and Noise Level of Reconstructed Images: The s-ROI is defined to be voxels within a blood vessel that extends from $z = -9.87$-mm to $z = -7.07$-mm, including 20 voxels. At the plane of $z = -8.74$-mm, the blood vessel is centered at the white dashed box D shown in Fig. 5.14-(a). The signal intensities are plotted against the image standard deviations in Fig. 5.15-(a). This plot indicates that the signal intensity in the images reconstructed by use of the PLS-TV algorithm is lower than that of the FBP algorithm. This reveals that the PLS-TV algorithm can introduce image biases to achieve the same level of noise suppression. This observation is different than the previous observations from the six-tube phantom, perhaps because the PLS-TV algorithm somehow promotes discontinuities in the diffuse background. Nevertheless, the CNR's of the images reconstructed by use of the PLS-TV algorithm are higher than those of the FBP algorithms for the regularization parameters spanning a wide range as shown in Fig. 5.15-(b).

Trade-Off Between Image Resolution and Noise Level of Reconstructed Images: The plots of resolution against background standard deviation are shown in Fig. 5.16. Similar to our observations from the six-tube phantom imaging, the spatial resolution of the images reconstructed by use of the PLS-TV algorithm is higher than that of the images reconstructed by use of the FBP algorithm when the images have the same background standard deviation. Also, the curve corresponding to the PLS-TV algorithm is flatter than that of the FBP algorithm, confirming that the TV regularization mitigates image noise with minimal sacrifice in spatial resolution.

Reconstructed Images from Sparsely-Sampled Data Sets: Figures 5.17 and 5.18 show sectional images at different locations. Each figure contains subfigures reconstructed by use of the FBP and the PLS-TV algorithms from the 90-view data set and the 45-view data set. The observations are in general consistent with those corresponding to densely-sampled data sets; namely the images reconstructed by use of the PLS-TV algorithm appear to have higher spatial resolution, higher contrast, and cleaner backgrounds.

5.5 Discussion and Summary

In this study, we investigated two iterative imaging reconstruction algorithms for 3D PACT: the penalized least-squares (PLS) with a quadratic smoothness penalty (PLS-Q) and the PLS with a TV-norm penalty (PLS-TV). To our knowledge, this was the first systematic investigation of 3D iterative image reconstruction for PACT animal imaging. Our results demonstrated the feasibility and advantages of 3D iterative image reconstruction algorithms for PACT. Specifically, the PLS-TV algorithm overall outperforms the FBP algorithm proposed by Finch et al. and the conventional iterative image reconstruction algorithm (e.g., PLS-Q) for reconstruction from incomplete data. Although not reported here, we observed this result to also hold true when other mathematically equivalent FBP algorithms were employed [122].

In PACT, the majority of studies of advanced image reconstruction algorithms have been based on 2D imaging models [37, 89, 17, 126]. For a 2D imaging model to be valid in practice, it is necessary to assume the focused transducers only receive in-plane acoustic signals. The accuracy of this assumption is still under investigation [92]. However, it is interesting to note that none of these studies compared the performances of 2D analytic reconstruction algorithms with those of the iterative algorithms, although the 2D analytic reconstruction algorithms have been proposed and proved to be mathematically exact [35, 26]. In this work, our studies are based on a 3D imaging model that incorporates ultrasonic transducer characteristics [105], avoiding heuristic assumptions regarding the transducer response. Although the FBP algorithm neglects the SIR effect, when the region-of-interest is close to the center of the measurement sphere, the images reconstructed by use of the FBP algorithm from densely-sampled data provide an accurate reference image that permits quantitative evaluation of images reconstructed by use of the PLS-Q and PLS-TV algorithms when data are incomplete. On the other hand, from densely-sampled data, the images reconstructed by use of different algorithms are quantitatively consistent, further validating our 3D imaging model.

The TV-norm regularization penalty has been intensively investigated within the context of mature imaging modalities including X-ray computed tomography (CT) [87, 39]. In a study of X-ray CT, the TV-norm regularized iterative reconstruction algorithm has been demonstrated to achieve the same image quality as those reconstructed by use of analytic

reconstruction algorithms, while reducing the amount of data required to one sixth of that the latter requires [39, 12]. However, our images reconstructed from sparsely-sampled data sets by use of the PLS-TV algorithm contain clear differences from those reconstructed from densely-sampled data by use of the FBP algorithm. Moreover, from densely-sampled data, the images reconstructed by use of the PLS-TV algorithm also appear to be different from those reconstructed by use of the FBP algorithm. Note the streaklike artifacts in the six-tube phantom images reconstructed by use of the FBP algorithm in Fig. 5.4, which remain visible even when the number of tomographic views is increased to 720. These artifacts are likely due to the inconsistencies between the measured data and the numerical imaging model. Such inconsistencies can be caused by unmodeled heterogeneities in the medium [43, 42, 95], errors in the assumed transducer response, and uncharacterized noise sources [123, 124]. These inconsistencies can prevent PACT reconstruction algorithms from working as effectively as their counterparts in mature imaging modalities such as X-ray CT that are well-characterized.

There remain several important topics for future studies that may further improve image quality in 3D PACT. Such topics include the development and investigation of more accurate imaging models that model the effects of acoustic heterogeneities and attenuation. Also, in this study, we employed an unweighted least-squares data fidelity term, which is equivalent to the maximum likelihood estimator assuming that the randomness in the measured data is due to additive Gaussian white noise [69]. However, additive Gaussian white noise may not be a good approximation in practice [99]. Identification of the noise sources and characterization of their second order statistical properties will facilitate iterative reconstruction algorithms that may optimally reduce noise levels in the reconstructed images. Even though our reconstruction algorithms were implemented using GPUs, the reconstruction time were still on the order of hours, which is undesirable for future clinical imaging applications of 3D PACT. Therefore there remains a need for the development of accelerated reconstruction algorithms and their evaluation for specific diagnostic tasks.

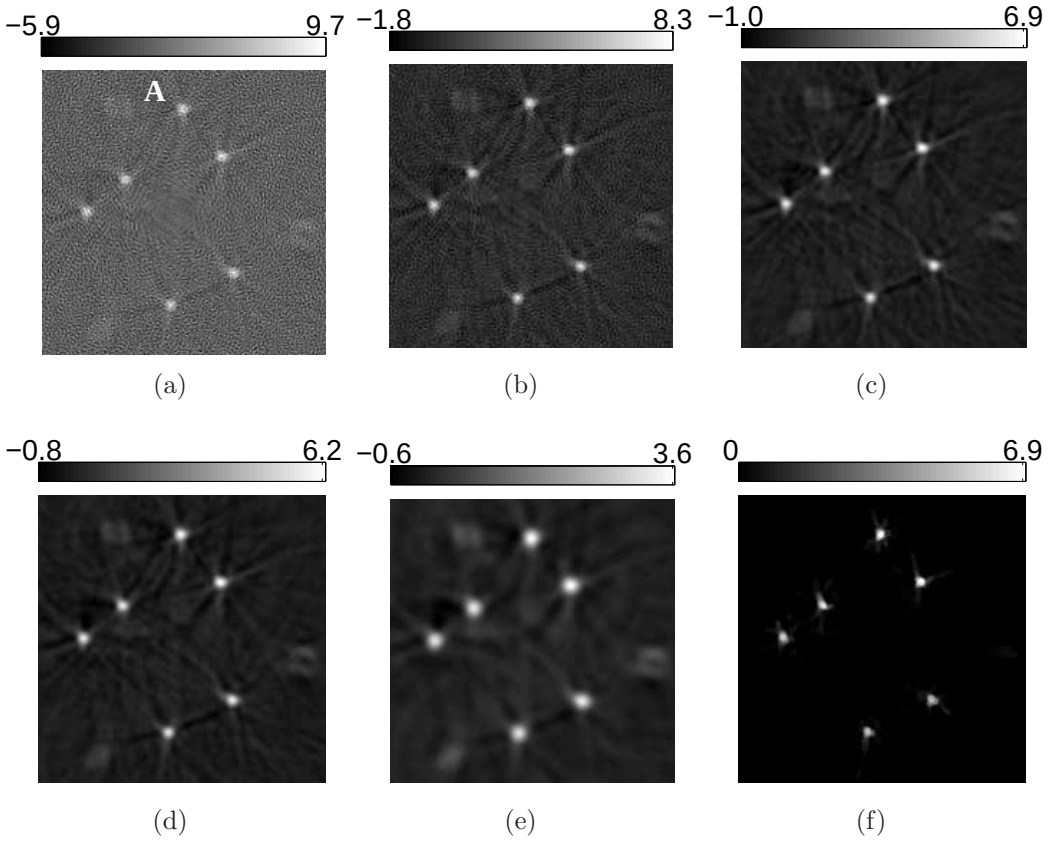

Figure 5.4: Slices corresponding to the plane $z = -2.0$-mm through the 3D images of the six-tube phantom reconstructed from (a) the 720-view data by use of the FBP algorithm with $f_c = 10$-MHz; (b) the 720-view data by use of the FBP algorithm with $f_c = 8$-MHz; (c) the 720-view data by use of the FBP algorithm with $f_c = 6$-MHz; (d) the 720-view data by use of the FBP algorithm with $f_c = 4$-MHz; (e) the 720-view data by use of the FBP algorithm with $f_c = 2$-MHz; and (f) the 144-view data by use of the PLS-TV algorithm with $\beta = 0.1$. All images are of size 19.8×19.8-mm^2. The ranges of the grayscale windows were determined by the minimum and the maximum values in each image.

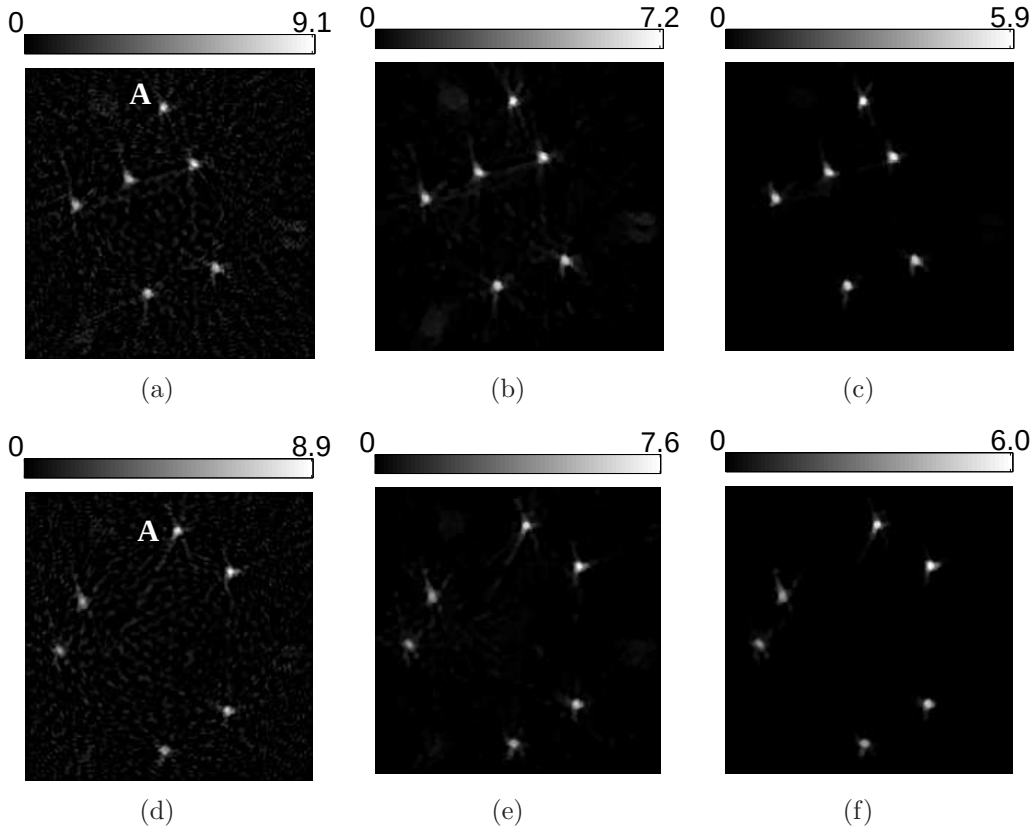

Figure 5.5: Slices corresponding to the plane $z = -6.0$-mm (top row: a-c) and the plane $z = 4.5$-mm (bottom row: d-f) through the 3D images of the six-tube phantom reconstructed from the 144-view data by use of the PLS-TV algorithm with varying regularization parameter β: (a), (d) $\beta = 0.001$; (b), (e) $\beta = 0.05$; and (c), (f) $\beta = 0.1$; All images are of size 19.8×19.8-mm^2. The ranges of the grayscale windows were determined by the minimum and the maximum values in each image.

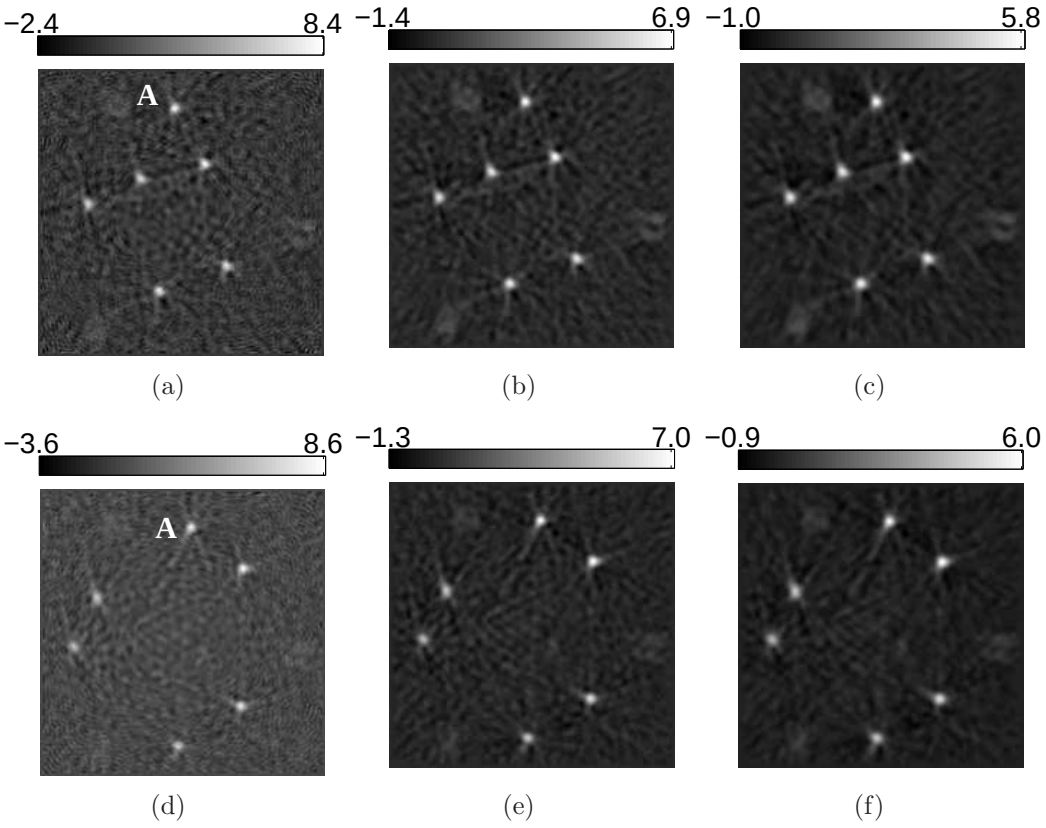

Figure 5.6: Slices corresponding to the plane $z = -6.0$-mm (top row: a-c) and the plane $z = 4.5$-mm (bottom row: d-f) through the 3D images of the six-tube phantom reconstructed from the 144-view data by use of the PLS-Q algorithm with varying regularization parameter γ: (a), (d) $\gamma = 0$; (b), (e) $\gamma = 1.0 \times 10^3$; and (c), (f) $\gamma = 5.0 \times 10^3$; All images are of size 19.8×19.8-mm^2. The ranges of the grayscale windows were determined by the minimum and the maximum values in each image.

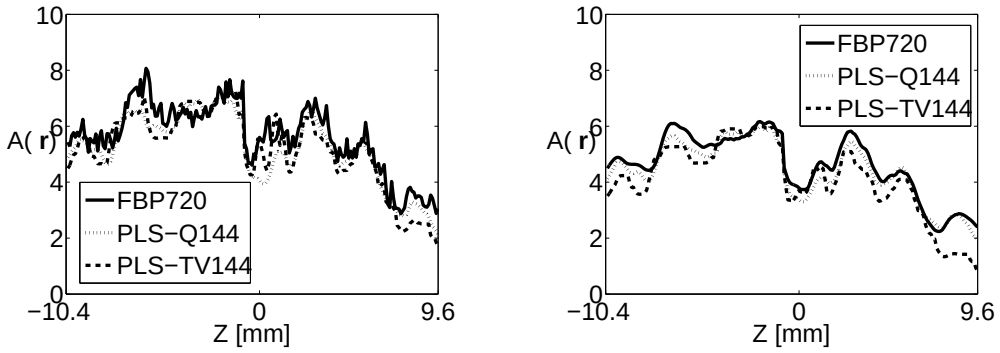

(a) (b)

Figure 5.7: Image profiles along the z-axis through the center of Tube-A extracted from images reconstructed by use of (a) the FBP algorithm with $f_c = 10$-MHz from the 720-view data (solid line) the PLS-Q algorithm with $\gamma = 1.0 \times 10^3$ from the 144-view data (dotted line), and the PLS-TV algorithm with $\beta = 0.05$ from the 144-view data (dashed line). Subfigure (b) shows the corresponding profiles for the case where each algorithm employed stronger regularization specified by the parameters $f_c = 5$-MHz, $\gamma = 5.0 \times 10^3$, and $\beta = 0.1$, respectively.

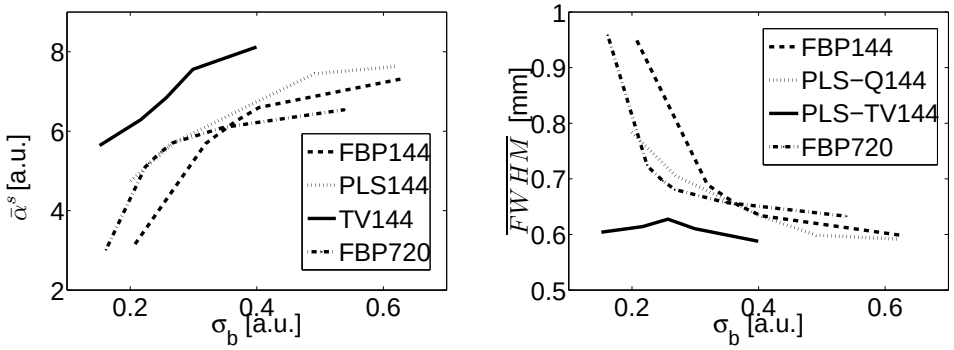

(a) (b)

Figure 5.8: (a) Signal intensity vs. standard deviation curves and (b) image resolution vs. standard deviation curves for the images reconstructed by use of the FBP algorithm from the 144-view data (FBP144), the PLS-Q algorithm from the 144-view data (PLS-Q144), the PLS-TV algorithm from the 144-view data (PLS-TV144), and the FBP algorithm from the 720-view data (FBP720).

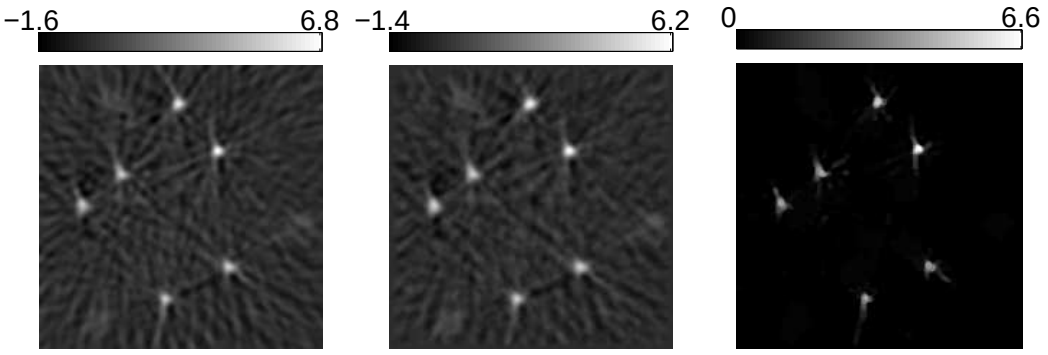

(a) (b) (c)

Figure 5.9: Slices corresponding to the plane $z = -2.0$-mm through the 3D images of the six-tube phantom reconstructed from the 72-view data by use of (a) the FBP algorithm with $f_c = 3.7$-MHz; (b) the PLS-Q algorithm with $\gamma = 1.0 \times 10^3$; and (c) the PLS-TV algorithm with $\beta = 0.07$. All images are of size 19.8×19.8-mm^2. The ranges of the grayscale windows were determined by the minimum and the maximum values in each image.

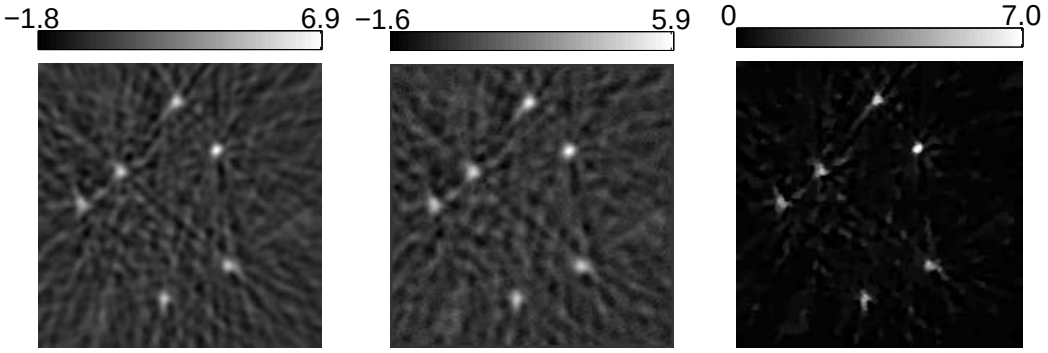

(a) (b) (c)

Figure 5.10: Slices corresponding to the plane $z = -2.0$-mm through the 3D images of the six-tube phantom reconstructed from the 36-view data by use of (a) the FBP algorithm with $f_c = 3.3$-MHz; (b) the PLS-Q algorithm with $\gamma = 7.0$; and (c) the PLS-TV algorithm with $\beta = 0.02$; All images are of size 19.8×19.8-mm^2. The ranges of the grayscale windows were determined by the minimum and the maximum values in each image.

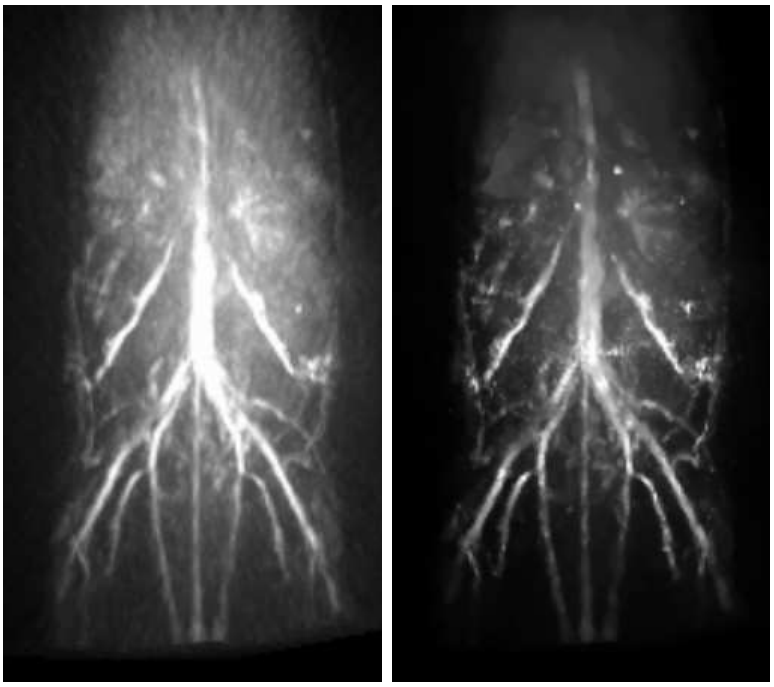

(a) (b)

Figure 5.11: MIP renderings of the 3D images of the mouse body reconstructed from the 180-view data by use of (a) the FBP algorithm with f_c = 5-MHz; and (b) the PLS-TV algorithm with $\beta = 0.05$; The grayscale window is [0,12.0].

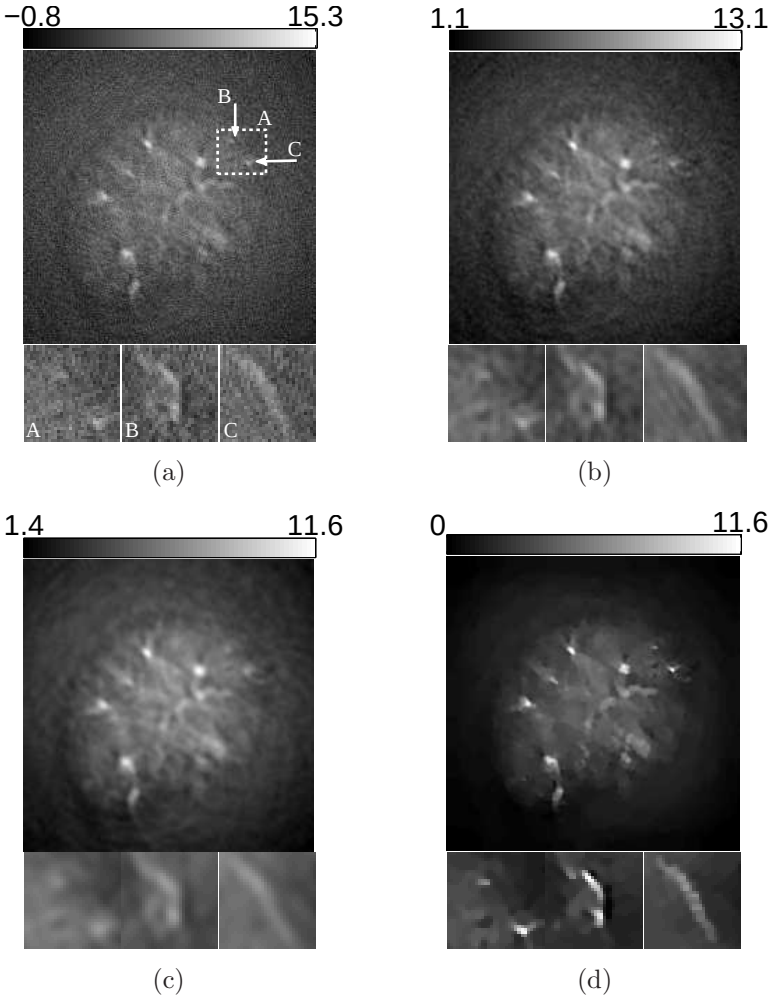

Figure 5.12: Slices corresponding to the plane $z = -8.47$-mm through the 3D images of the mouse body reconstructed from the 180-view data by use of (a) the FBP algorithm with $f_c = 8$-MHz; (b) the FBP algorithm with $f_c = 5$-MHz; (c) the FBP algorithm with $f_c = 3$-MHz; and (d) the PLS-TV algorithm with $\beta = 0.05$. The images are of size 29.4×29.4-mm^2. The three zoomed-in images correspond to the ROIs of the dashed rectangle A, and the images on the orthogonal planes $x = 8.47$-mm (Intersection line is along the arrow B), and $y = -3.29$-mm (Intersection line is along the arrow C), respectively. All zoomed-in images are of size 4.34×4.34-mm^2. The ranges of the grayscale windows were determined by the minimum and the maximum values in each image.

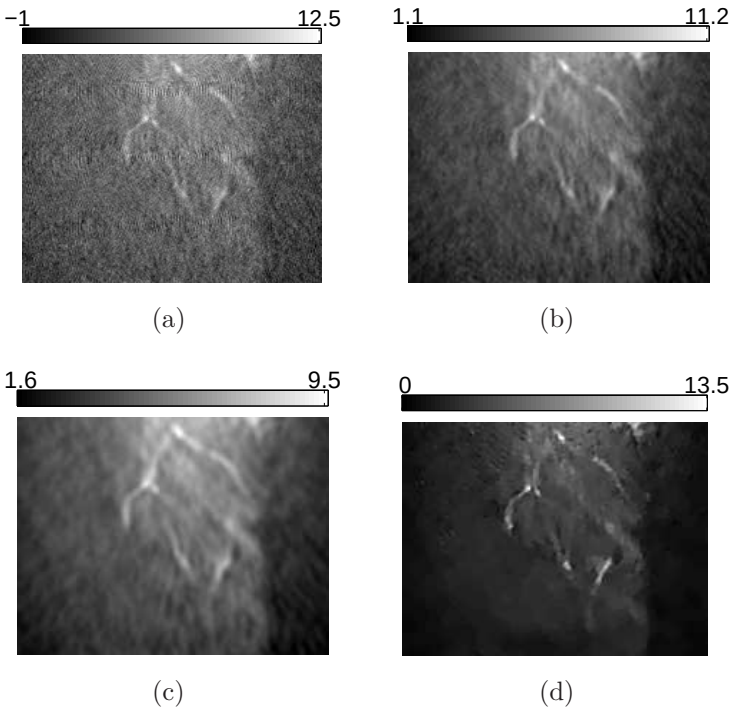

Figure 5.13: Slices corresponding to the plane $y = -3.57$-mm through the 3D images of the mouse body reconstructed from the 180-view data by use of (a) the FBP algorithm with $f_c = 8$-MHz; (b) the FBP algorithm with $f_c = 5$-MHz; (c) the FBP algorithm with $f_c = 3$-MHz; and (d) the PLS-TV algorithm with $\beta = 0.05$. The images are of size 22.4×29.4-mm^2. The ranges of the grayscale windows were determined by the minimum and the maximum values in each image.

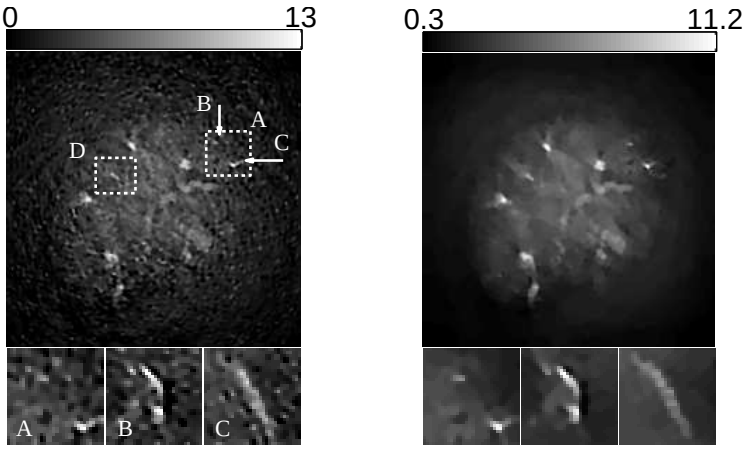

(a) (b)

Figure 5.14: Slices corresponding to the plane $z = -8.47$-mm through the 3D images of the mouse body reconstructed from the 180-view data by use of the PLS-TV algorithm with (a) $\beta = 0.01$; and (b) $\beta = 0.1$. The images are of size 29.4×29.4-mm^2. The three zoomed-in images correspond to the ROIs of the dashed rectangle A, and the images on the orthogonal planes $x = 8.47$-mm (Intersection line is along the arrow B), and $y = -3.29$-mm (Intersection line is along the arrow C), respectively. All zoomed-in images are of size 4.34×4.34-mm^2. The ranges of the grayscale windows were determined by the minimum and the maximum values in each image.

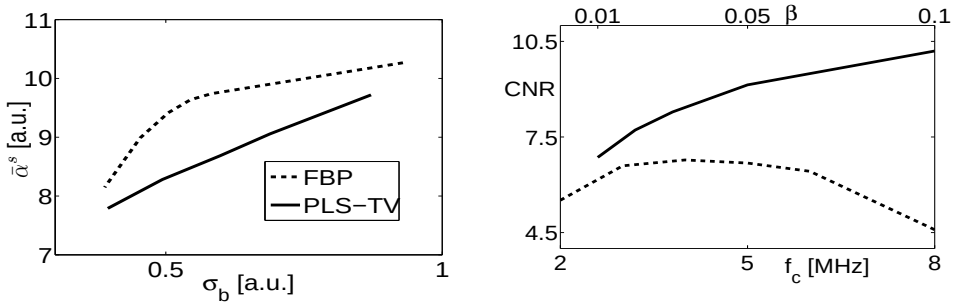

(a) (b)

Figure 5.15: (a) Signal intensity vs. standard deviation curves for the images reconstructed by use of the FBP (dashed line) and the PLS-TV (solid line) algorithms from the 180-view data; (b) CNR vs. the cutoff frequency curve for the FBP algorithm (dashed line) and CNR vs. the regularization parameter β curve for the PLS-TV algorithm (solid line) from the 180-view data.

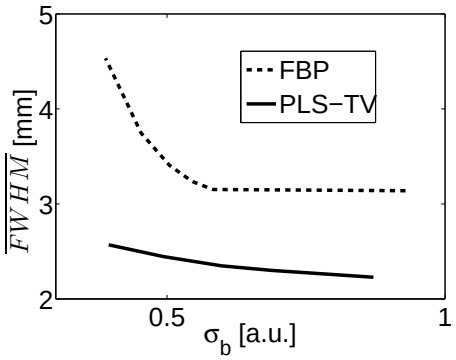

Figure 5.16: Image resolution vs. standard deviation curves for the images reconstructed by use of the FBP and PLS-TV algorithms from the 180-view data.

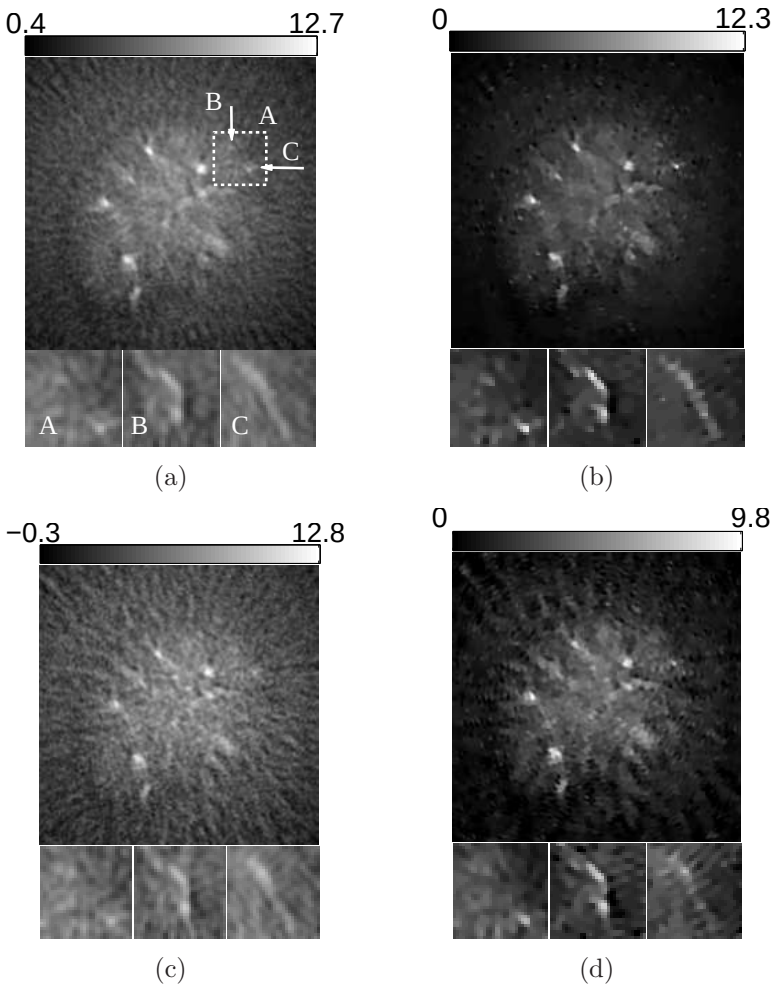

Figure 5.17: Slices corresponding to the plane $z = -8.47$-mm through the 3D images of the mouse body reconstructed from the 90-view data (top row: a, b) and the 45-view data (bottom row: c, d) by use of (a) the FBP algorithm with $f_c = 5$-MHz; (b) the PLS-TV algorithm with $\beta = 0.03$; (c) the FBP algorithm with $f_c = 5$-MHz; and (d) the PLS-TV algorithm with $\beta = 0.01$. The images are of size 29.4×29.4-mm^2. The three zoomed-in images correspond to the ROIs of the dashed rectangle A, and the images on the orthogonal planes $x = 8.47$-mm (Intersection line is along the arrow B) and $y = -3.29$-mm (Intersection line is along the arrow C), respectively. All zoomed-in images are of size 4.34×4.34-mm^2. The ranges of the grayscale windows were determined by the minimum and the maximum valuse of each image.

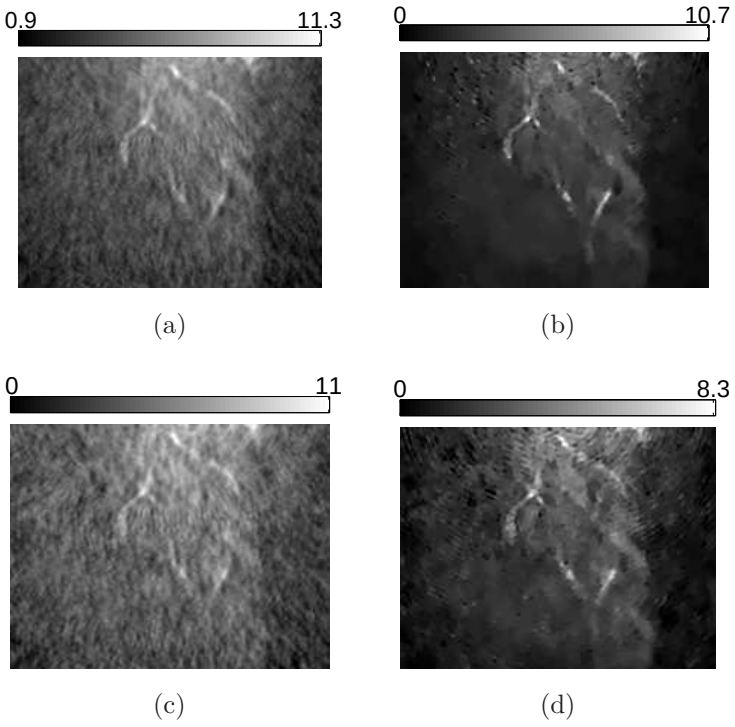

Figure 5.18: Slices corresponding to the plane $y = -3.57$-mm through the 3D images of the mouse body reconstructed from the 90-view data (top row: a, b) and the 45-view data (bottom row: c, d) by use of (a) the FBP algorithm with $f_c = 5$-MHz; (b) the PLS-TV algorithm with $\beta = 0.03$; (c) the FBP algorithm with $f_c = 5$-MHz; and (d) the PLS-TV algorithm with $\beta = 0.01$. The images are of size 22.4×29.4-mm^2. The ranges of the grayscale windows were determined by the minimum and the maximum values in each image.

Chapter 6

Accelerating Image Reconstruction in 3D PACT on Graphics Processing Units

6.1 Introduction

Although photoacoustic wave intrinsically propagates in three-dimensional (3D) space, when applying to experimental data, most studies have employed two-dimensional (2D) imaging models by making certain assumptions on the transducer responses and/or the object structures [127, 89, 37, 44, 17, 43]. An important reason is because the computation required for 3D PACT image reconstruction is excessively burdensome. Therefore, there remains a great need to develop fast implementations of 3D reconstruction algorithms.

A graphics processing unit (GPU) card is a specialized device specifically designed for parallel computations [62]. Compute unified device architecture (CUDA) is an extension of the C/Fortran language that provides a convenient programming platform to exploit the parallel computational power of GPUs [76]. The CUDA-based parallel programming technique has been successfully applied to accelerate image reconstruction in mature imaging modalities such as X-ray computed tomography (CT) [134, 78, 20] and magnetic resonance imaging (MRI) [98]. In PACT, however, only a few works on utilization of GPUs to accelerate image reconstruction have been reported [16, 101]. For example, the k-wave toolbox employs the NVIDIA CUDA Fast Fourier Transform library (cuFFT) to accelerate the computation of 3D FFT [101]. Also a GPU-based sparse matrix-vector multiplication strategy has been

applied to 3D PACT image reconstruction for the case that the system matrix is sparse and can be stored in memory [16]. However, there remains an important need to develop efficient implementations of PACT reconstruction algorithms for general applications in which the system matrix is too large to be stored.

In this chapter, we propose parallelization strategies, for use with GPUs, to accelerate 3D image reconstruction in PACT. Both filtered backprojection (FBP) and iterative image reconstruction algorithms are investigated. For use with iterative image reconstruction algorithms, we focus on the parallelization of projection and backprojection operators. Specifically, we develop two pairs of projection/backprojection operators that correspond to two distinct discrete-to-discrete (D-D) imaging models employed in PACT, namely the interpolation-based and the spherical-voxel-based D-D imaging models. Note that our implementations of the backprojection operators compute the exact adjoint of the forward operators, and therefore the projector pairs are 'matched' [9].

The remainder of the chapter is organized as follows. In Section 6.2, we briefly review PACT imaging models in their continuous and discrete forms. We propose GPU-based parallelization strategies in Section 6.3. Numerical studies and results are described in Section 6.4 and Section 6.5 respectively. Finally, a brief discussion and summary of the proposed algorithms are provided in Section 6.6.

6.2 Background

PACT C-C imaging models have been described in Section 2.1. Based on the C-C imaging models, a variety of analytic image reconstruction algorithms have been developed [55, 34, 122, 121]. For the case of a spherical measurement geometry, an FBP algorithm in its continuous form is given by Eqn. (5.11) [34]. As discussed in Chapter 4, a C-D imaging model has been proposed to describe practical PACT imaging systems. In order to conduct iterative image reconstructions, we approximate the C-D imaging model by a D-D imaging model that employs uniform spherical expansion functions to represent the object function. This D-D imaging model in the temporal-frequency domain has been thoroughly described in Section 5.2.1, and will be referred to as 'spherical-voxel-based' D-D imaging model in this chapter. When the diffraction effects of transducers are not critical, an 'interpolation-based'

D-D imaging model can be constructed and has been applied for PACT image reconstructions [2, 133, 17]. Below the quantities $\mathbf{u}$, $\mathbf{H}$, and $\boldsymbol{\alpha}$ (or ψ_n) in the two models will be distinguished by the subscripts (or superscripts) 'int' and 'sph', respectively. In Section 6.2.1 we briefly review the 'interpolation-based' D-D imaging model. We derived the adjoints of both the 'interpolation-based' and the 'spherical-based' D-D imaging models in Section 6.2.2. The basics of GPU architecture and CUDA programming are outlined in Section 6.2.3.

6.2.1 Interpolation-Based D-D Imaging Model

The interpolation-based D-D imaging model provides another approximation to the C-D imaging model defined by Eqn. (4.5). Following the generic methodology described in Section 4.3.2, the interpolation-based D-D imaging model defines the coefficient vector as samples of the object function on the nodes of a uniform Cartesian grid:

$$\left[\boldsymbol{\alpha}_{\text{int}}\right]_n = \int_V d\mathbf{r}\, \delta(\mathbf{r} - \mathbf{r}_n) A(\mathbf{r}), \quad n = 0, 1, \cdots, N-1, \tag{6.1}$$

where, $\mathbf{r}_n = (x_n, y_n, z_n)^T$ specifies the location of the n-th node of the uniform Cartesian grid. The definition of the expansion function depends on the choice of interpolation method [17]. If a trilinear interpolation method is employed, the expansion function can be expressed as [46]:

$$\psi_n^{\text{int}}(\mathbf{r}) = \begin{cases} (1 - \frac{|x-x_n|}{\Delta_s})(1 - \frac{|y-y_n|}{\Delta_s})(1 - \frac{|z-z_n|}{\Delta_s}), & \text{if } |x-x_n|, |y-y_n|, |z-z_n| \leq \Delta_s \\ 0, & \text{otherwise} \end{cases}, \tag{6.2}$$

where Δ_s is the distance between two neighboring grid points.

In principle, the interpolation-based D-D imaging model can be constructed by substitution from Eqns. (6.1) and (6.2) to Eqn. (4.5). In practice, however, implementation of the surface integral over S_q is difficult for the choice of expansion functions as Eqn. (6.2). Also, implementations of the temporal convolution and $\mathcal{H}_{\text{CC}}\psi_n^{\text{int}}$ usually require extra discretization procedures. Therefore, utilization of the interpolation-based D-D model commonly assumes the transducers to be point-like. In this case, the implementation of $\mathbf{H}_{\text{int}}$ is decomposed as

a three-step operation:

$$\mathbf{u}_{\text{int}} = \mathbf{H}_{\text{int}}\boldsymbol{\alpha}_{\text{int}} \equiv \mathbf{H}^e\mathbf{D}\mathbf{G}\boldsymbol{\alpha}_{\text{int}}, \tag{6.3}$$

where $\mathbf{G}$, $\mathbf{D}$, and $\mathbf{H}^e$ are discrete approximations of the SRT (Eqn. (2.2)), the differential operator (Eqn.(2.3)), and the operator that implements a temporal convolution with EIR, respectively. We implemented $\mathbf{G}$ in a way [1, 2, 133] that is similar to the 'ray-driven' implementation of Radon transform in X-ray CT [46], i.e, for each data sample, we accumulated the contributions from the voxels that resided on the spherical shell specified by the data sample. By use of Eqns. (2.2), (2.9), (6.1), and (6.2), one obtains:

$$\big[\mathbf{G}\boldsymbol{\alpha}_{\text{int}}\big]_{qK+k} = \Delta_s^2 \sum_{n=0}^{N-1} \big[\boldsymbol{\alpha}_{\text{int}}\big]_n \sum_{i=0}^{N_i-1}\sum_{j=0}^{N_j-1} \psi_n^{\text{int}}(\mathbf{r}_{k,i,j}) \equiv \big[\mathbf{g}\big]_{qK+k}, \tag{6.4}$$

where $[\mathbf{g}]_{qK+k} \approx g(\mathbf{r}_q^s, t)|_{t=k\Delta_t}$ with $\mathbf{r}_q^s$ specifying the location of the q-th point-like transducer, and N_i and N_j denote the numbers of divisions over the two angular coordinates of a local spherical coordinate system shown in Fig. 6.1-(b). A derivation of Eqn. (6.4) is provided in Appendix. The differential operator in Eqn. (2.3) is approximated as

$$\big[\mathbf{D}\mathbf{g}\big]_{qK+k} = \frac{\beta}{8\pi C_p \Delta_t^2}\Big(\frac{[\mathbf{g}]_{qK+k+1}}{k+1} - \frac{[\mathbf{g}]_{qK+k-1}}{k-1}\Big) \equiv \big[\mathbf{p}_{\text{int}}\big]_{qK+k}, \tag{6.5}$$

where $[\mathbf{p}_{\text{int}}]_{qK+k} \approx p(\mathbf{r}_q^s, t)|_{t=k\Delta_t}$. Finally, the continuous temporal convolution is approximated by a discrete linear convolution as [21]

$$\big[\mathbf{H}^e\mathbf{p}_{\text{int}}\big]_{qK+k} = \sum_{\kappa=0}^{K-1} [\mathbf{h}^e]_{k-1-\kappa}[\mathbf{p}_{\text{int}}]_{qK+\kappa} \equiv [\mathbf{u}_{\text{int}}]_{qK+k}, \tag{6.6}$$

where $[\mathbf{h}^e]_k = \Delta_t h^e(t)|_{t=k\Delta_t}$.

6.2.2 Adjoints of the Interpolation-Based and the Spherical-Voxel-Based System Matrices

Iterative image reconstruction algorithms employ numerical implementations of the projection operator, i.e., the system matrix $\mathbf{H}$, as well as its adjoint, denoted by $\mathbf{H}^\dagger$ [69]. The

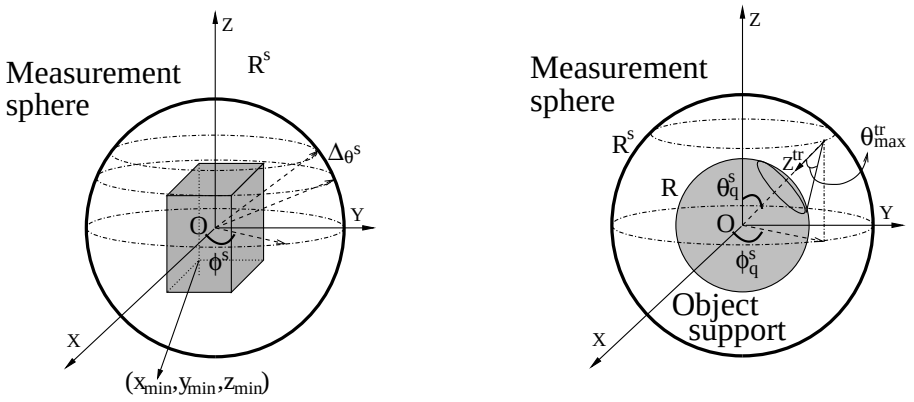

(a) (b)

Figure 6.1: (a) Schematic of the 3D PACT scanning geometry. (b) Schematic of the local coordinate system for the implementation of interpolation-based D-D imaging model

adjoint is also referred to as the backprojection operator. Note that for most practical applications, $\mathbf{H}$ and $\mathbf{H}^\dagger$ are too large to be stored in the random access memory of currently available computers. Therefore, in practice, the actions of $\mathbf{H}$ and $\mathbf{H}^\dagger$ are almost always calculated on the fly. The same strategy was adopted in this work.

According to the definition of the adjoint operator [9, 21], $\mathbf{H}_{\text{int}}^\dagger = \mathbf{G}^\dagger \mathbf{D}^\dagger \mathbf{H}^{\text{e}\dagger}$, where

$$\left[\mathbf{H}^{\text{e}\dagger}\mathbf{u}_{\text{int}}\right]_{qK+k} = \sum_{\kappa=0}^{K-1} [\mathbf{h}^e]_{\kappa-1-k}[\mathbf{u}]_{qK+\kappa} \equiv [\mathbf{p}'_{\text{int}}]_{qK+k}, \tag{6.7}$$

$$\left[\mathbf{D}^\dagger \mathbf{p}'_{\text{int}}\right]_{qK+k} = \frac{\beta}{8\pi C_p \Delta_t^2 k}\Big(\left[\mathbf{p}'_{\text{int}}\right]_{qK+k-1} - \left[\mathbf{p}'_{\text{int}}\right]_{qK+k+1}\Big) \equiv \left[\mathbf{g}'\right]_{qK+k}, \tag{6.8}$$

and

$$\left[\mathbf{G}^\dagger \mathbf{g}'\right]_n = \Delta_s^2 \sum_{q=0}^{Q-1}\sum_{k=0}^{K-1} \left[\mathbf{g}'\right]_{qK+k} \sum_{i=0}^{N_i-1}\sum_{j=0}^{N_j-1} \psi_n^{\text{int}}(\mathbf{r}_{k,i,j}) \equiv [\boldsymbol{\alpha}'_{\text{int}}]_n. \tag{6.9}$$

It can also be verified that the adjoint operator $\mathbf{H}_{\text{sph}}^\dagger$ is given by:

$$\left[\mathbf{H}_{\text{sph}}^\dagger \tilde{\mathbf{u}}_{\text{sph}}\right]_n = \sum_{q=0}^{Q-1}\sum_{l=0}^{L-1} \left[\tilde{\mathbf{u}}_{\text{sph}}\right]_{qL+l} \tilde{p}_0^*(f)\tilde{h}_q^*(\mathbf{r}_n, f)\Big|_{f=l\Delta_f}, \tag{6.10}$$

where the superscript '*' denotes the complex conjugate. Unlike the unmatched backprojection opertors [129] that are obtained by discretization of the continuous adjoint operator, utilization of the exact adjoint operator facilitates the convergence of iterative image reconstruction algorithms.

6.2.3 GPU Architecture and CUDA programming

The key features of GPU architecture and the basics of CUDA programming are briefly summarized in this section. We refer the readers to [76, 62] for additional details.

A GPU card contains multiple streaming multiprocessors. Each streaming multiprocessor is configured with multiple processor cores. For example, the Tesla C1060 possesses 30 streaming multiprocessors with 8 processor cores on each; and the Tesla C2050 possesses 14 streaming multiprocessors with 32 processor cores on each [62]. The processor cores in each multiprocessor execute the same instruction on different pieces of data, which is referred to as "single instruction, multiple data" (SIMD) model of parallel programming. In order to fully exploit the computing power of GPUs, one of the major challenges is to design a parallelization strategy fitting in the SIMD framework such that the largest number of processor cores can execute the computation simultaneously [76].

A GPU card has six types of memory that have varying capacities and different access rules and efficiencies: (1) Registers are assigned for each thread and have the fastest access. (2) Shared memory is assigned for each block and can be efficiently accessed by all threads in the block if designed appropriately. (3) Constant memory is read-only and can be accessed by all threads efficiently. (4) Texture memory is also read-only and is optimized for interpolation operations. (5) Global memory has the slowest access that takes hundreds times more clock cycles than does the computation of basic arithmetic operations. (6) Local memory is assigned for each thread but has a slow access as does the global memory. Therefore, an efficient GPU-based implementation in general requires a limited number of global and local memory access.

CUDA is a platform and programming model developed by NVIDIA that includes a collection of functions and keywords to exploit the parallel computing power of GPUs [76]. A CUDA

parallel program is composed of a host program and kernels. The host program is executed by CPUs and launches the kernels, which are custom-designed functions executed by GPUs. A general parallel programming strategy is to launch multiple instances of a kernel and to run the multiple instances concurrently on GPUs. In CUDA, each instance of the kernel is named as a thread and processes only a portion of the data. A hierarchy of threads is employed: Threads are grouped into blocks, and blocks are grouped into a grid. Therefore, each thread is specified by a multi-index containing a block index and a thread index within the block.

6.3 GPU-Accelerated Reconstruction Algorithms

In this section, we propose GPU-based parallelization strategies for the FBP algorithm and the projection/backprojection operations corresponding to the interpolation-based and the spherical-voxel-based D-D imaging models.

6.3.1 Measurement Geometry

We employed a spherical measurement geometry shown in Fig. 6.1-(a). The measurement sphere was of radius R^s centered at the origin of the Cartesian coordinate system (or the equivalent spherical coordinate system). The polar angle $\theta^s \in [0, \pi]$ was equally divided with interval $\Delta_{\theta^s} = \pi/N_r$, starting from $\theta^s_{\min}$. At each polar angle, a ring on the sphere that was parallel to the plane $z = 0$ can be specified, resulting N_r rings. On each ring, N_v ultrasonic transducers were assumed to be uniformly distributed with azimuth angle interval $\Delta_{\phi^s} = 2\pi/N_v$. Hereafter, each azimuth angle will be referred to as a tomographic view. At each view, we assumed that N_t temporal samples were acquired and the first sample corresponded to time instance $t_{\min}$. For implementations in temporal-frequency domain, we assumed that N_f temporal-frequency samples were available and the first sample corresponded to $f_{\min}$. The region to be reconstructed was a rectangular cuboid whose edges were parallel to the axes of the coordinate system and the left-bottom-back vertex was located at $(x_{\min}, y_{\min}, z_{\min})$. The numbers of voxels along the three coordinates will be denoted by N_x, N_y, and N_z, respectively, totally $N = N_x N_y N_z$ voxels. We also assumed the cuboid was contained in

another sphere of radius R that was concentric with the measurement sphere shown in Fig. 6.1-(b).

6.3.2 Implementation of the FBP Algorithm

Central processing unit (CPU)-based implementations of continuous FBP formulae have been described in [55, 34, 122, 121]. Though the discretization methods vary, in general, three approximations have to be employed. Firstly, the first-order derivative term $\partial p(\mathbf{r}^s, t)/\partial t$ has to be approximated by a difference scheme up to certain order [73]. Secondly, the measurement sphere has to be divided into small patches, and the surface integral has to be approximated by a summation of the area of every patch weighted by the effective value of the integrand on the patch. Finally, the value of the integrand at an arbitrary time instance $t = |\mathbf{r}^s - \mathbf{r}|/c_0$ has to be approximated by certain interpolation method.

In this study, we approximated the surface integral by use of the trapezoidal rule. As described earlier, the spherical surface was divided into $N_r N_v$ patches. For the transducer indexed by q that was located at $\mathbf{r}_q^s = (R^s, \theta_q^s, \phi_q^s)$, the area of the patch was approximated by $(R^s)^2 \Delta_{\theta^s} \Delta_{\phi^s} \sin\theta_q^s$. The value at time instance $t = |\mathbf{r}_q^s - \mathbf{r}_n|/c_0$ was approximated by the linear interpolation from its two neighboring samples as:

$$p(\mathbf{r}_q^s, t)\Big|_{t=\frac{|\mathbf{r}_q^s - \mathbf{r}_n|}{c_0}} \approx \big(k + 1 - \tilde{k}\big)\big[\mathbf{p}\big]_{qK+k} + \big(\tilde{k} - k\big)\big[\mathbf{p}\big]_{qK+k+1}, \tag{6.11}$$

where $\tilde{k} = (|\mathbf{r}_q^s - \mathbf{r}_n|/c_0 - t_{\min})/\Delta_t$, and k is the integer part of $\tilde{k}$. Here $\mathbf{p}$ is a vector of lexicographically ordered samples of the pressure function $p(\mathbf{r}^s, t)$, which is estimated from the measured voltage data vector $\mathbf{u}$. Also, the first-order derivative term was approximated by:

$$\frac{\partial}{\partial t} p(\mathbf{r}_q^s, t)\Big|_{t=\frac{|\mathbf{r}_q^s - \mathbf{r}_n|}{c_0}} \approx \frac{1}{\Delta_t}\Big(\big[\mathbf{p}\big]_{qK+k+1} - \big[\mathbf{p}\big]_{qK+k}\Big). \tag{6.12}$$

By use of these three numerical approximations, the discretized FBP formula was expressed as:

$$\left[\hat{\boldsymbol{\alpha}}_{\text{fbp}}\right]_n = -\frac{C_p R^s \Delta_{\theta^s} \Delta_{\phi^s}}{\pi\beta c_0^3 \Delta_t} \sum_{n_r=0}^{N_r-1} \sin\theta_q^s \sum_{n_v=0}^{N_v-1} \left\{ \left(1.5 - \frac{k + t_{\min}/\Delta_t}{\tilde{k} + t_{\min}/\Delta_t}\right) \left[\mathbf{p}\right]_{qK+k+1} + \left(\frac{k+1+t_{\min}/\Delta_t}{\tilde{k} + t_{\min}/\Delta_t} - 1.5\right) \left[\mathbf{p}\right]_{qK+k} \right\}. \tag{6.13}$$

Unlike the implementations of FBP formulas in X-ray cone beam CT [78, 20], we combined the filter and the linear interpolation. This reduced the number of visits to the global memory in the GPU implementation described below.

We implemented the FBP formula in a way that is similar to the 'pixel-driven' implementation in X-ray CT [20], i.e., we assigned each thread to execute the two accumulative summations in Eqn. (6.13) for each voxel. We bound the pressure data $\mathbf{p}$ to texture memory because it is cached and has a faster accessing rate. Therefore our implementation only requires access to texture memory twice and to global memory once. The pseudo-codes are provided in Algs. 1 and 2 for the host part and the device part respectively. Note that the pseudo-codes do not intend to be always optimal because the performance of the codes could depend on the dimensions of $\mathbf{p}$ and $\hat{\boldsymbol{\alpha}}_{\text{fbp}}$. For example, we set the block size to be $(N_z, 1, 1)$ because for our applications, N_z was bigger than N_x and N_y and smaller than the limit number of threads that a block can support (i.e., 1024 for the NVIDIA Tesla C2050). If the values of N_x, N_y, and N_z change, we may need to redesign the dimensions of the grid and blocks. However, the general SIMD parallelization strategy remains.

Algorithm 1 Implementation of the FBP algorithm (on host)

Input: $\mathbf{p}$

Output: $\hat{\boldsymbol{\alpha}}_{\text{fbp}}$

1: $w = -C_p R^s \Delta_{\theta^s} \Delta_{\phi^s} / (\pi\beta c_0^3 \Delta_t)$ {Precalculate the common coefficient}
2: T_$\mathbf{p} \leftarrow \mathbf{p}$ {Bound data to texture memory}
3: K_fbp $\langle\langle\langle \quad (N_y, N_x), (N_z, 1, 1) \quad \rangle\rangle\rangle$ (ω, D_$\hat{\boldsymbol{\alpha}}_{\text{fbp}}$)
4: $\hat{\boldsymbol{\alpha}}_{\text{fbp}} \leftarrow$ D_$\hat{\boldsymbol{\alpha}}_{\text{fbp}}$ {Copy data from global memory to host}

Algorithm 2 Implementation of kernel K_fbp $\langle\langle\langle \quad (N_y, N_x), (N_z, 1, 1) \quad \rangle\rangle\rangle$

Input: ω, T_**p**, D_$\hat{\boldsymbol{\alpha}}_{\text{fbp}}$

Output: D_$\hat{\boldsymbol{\alpha}}_{\text{fbp}}$

$x = (\text{blockIdx.y})\Delta_s + x_{\min}$; $y = (\text{blockIdx.x})\Delta_s + y_{\min}$; $z = (\text{threadIdx.x})\Delta_s + z_{\min}$
$\Sigma = 0$
for $n_r = 0$ **to** $N_r - 1$ **do**
    $\theta^s = n_r\Delta_{\theta^s} + \theta^s_{\min}$; $z^s = R^s\cos\theta^s$; $r^s = R^s\sin\theta^s$; $w' = w\sin\theta^s$
    for $n_v = 0$ **to** $N_v - 1$ **do**
        $\phi^s = n_v\Delta_{\phi^s} + \phi^s_{\min}$; $x^s = r^s\cos\phi^s$; $y^s = r^s\sin\phi^s$
        $\bar{t} = ((x - x^s)^2 + (y - y^s)^2 + (z - z^s)^2)^{1/2}$
        $t_n = (\bar{t}/c_0 - t_{\min})/\Delta_t$; $n_t = \text{floor}(t_n)$
        $\Sigma \mathrel{+}= \omega'\Big\{\big[(n_t\Delta_t + t_{\min})/(t_n\Delta_t + t_{\min}) - 1.5\big]\text{T\_}\mathbf{p}[n_r][n_v][n_t] + \big[1.5 - (n_t\Delta_t + t_{\min})/(t_n\Delta_t + t_{\min})\big]\text{T\_}\mathbf{p}[n_r][n_v][n_t + 1]\Big\}$ {Fetch data from texture memory}
    end for
end for
D_$\hat{\boldsymbol{\alpha}}_{\text{fbp}}$[blockIdx.y][blockIdx.x][threadIdx.x] $= \Sigma$

6.3.3 Implementation of $\mathbf{H}_{\text{int}}$ and $\mathbf{H}^{\dagger}_{\text{int}}$

The forward projection operation $\mathbf{H}_{\text{int}}\boldsymbol{\alpha}_{\text{int}}$ is composed of three consecutive operations $\mathbf{g} = \mathbf{G}\boldsymbol{\alpha}_{\text{int}}$, $\mathbf{p}_{\text{int}} = \mathbf{D}\mathbf{g}$, and $\mathbf{u}_{\text{int}} = \mathbf{H}^e\mathbf{p}_{\text{int}}$ that are defined in Eqns. (6.4), (6.5), and (6.6), respectively. Both the difference operator $\mathbf{D}$ and the one-dimensional (1D) convolution $\mathbf{H}^e$ have low computational complexities while the SRT operator $\mathbf{G}$ is computationally burdensome. Hence, we developed the GPU-based implementation of $\mathbf{G}$ while leaving $\mathbf{D}$ and $\mathbf{H}^e$ to be implemented by CPUs.

The SRT in PACT shares many features with the Radon transform in X-ray CT. Thus, our GPU-based implementation is closely related to the implementations of Radon transform that have been optimized for X-ray CT[134, 78, 20]. The surface integral was approximated according to the trapezoidal rule. Firstly, the integral surface was divided into small patches, which is described in the Appendix. Secondly, each patch was assigned an effective value of the object function by trilinear interpolation. The trilinear interpolation was calculated by use of the texture memory of GPUs that is specifically designed for interpolation. Finally, GPU threads accumulated the areas of patches weighted by the effective values of the object function and wrote the final results to global memory. The pseudo-codes for implementation

of $\mathbf{G}$ are provided in Algs. 3 and 4 for the host part and the device part, respectively. Note that we employed the "one-level"-strategy [20], i.e., each thread calculates one data sample. Higher level strategies have been proposed to improve the performance by assigning each block to calculate multiple data samples [20], which, however, caused many thread idles in PACT mainly because the amount of computation required to calculate a data sample varies largely among samples for SRT.

Algorithm 3 Implementation of $\mathbf{g} = \mathbf{G}\boldsymbol{\alpha}_{\text{int}}$ (on host)

Input: $\boldsymbol{\alpha}_{\text{int}}$
Output: $\mathbf{g}$

1: T_$\boldsymbol{\alpha}_{\text{int}} \leftarrow \boldsymbol{\alpha}_{\text{int}}$ {Bound data to texture memory}
2: K_srt $\langle\langle\langle \quad (N_v, N_t), (N_r, 1, 1) \quad \rangle\rangle\rangle$ (D_$\mathbf{g}$)
3: $\mathbf{g} \leftarrow$ D_$\mathbf{g}$ {Copy data from global memory to host}

Algorithm 4 Implementation of kernel K_srt $\langle\langle\langle \quad (N_v, N_t), (N_r, 1, 1) \quad \rangle\rangle\rangle$

Input: D_$\mathbf{g}$, T_$\boldsymbol{\alpha}_{\text{int}}$
Output: D_$\mathbf{g}$

1: $\bar{t} = (\text{blockIdx.y})c_0\Delta_t + c_0 t_{\min}$; $\quad \theta^s = (\text{threadIdx.x})\Delta_{\theta^s} + \theta^s_{\min}$; $\quad \phi^s = (\text{blockIdx.x})\Delta_{\phi^s} + \phi^s_{\min}$
2: $\theta'_{\max} = \arccos\left(((R^s)^2 + \bar{t}^2 - R^2)/(2\bar{t}R^s)\right)$
3: $\Sigma = 0$; $\quad \theta' = \theta'_{\max}$
4: **while** $\theta' > 0$ **do**
5: $\quad z' = \bar{t}\cos\theta'$; $\quad r' = \bar{t}\sin\theta'$; $\quad \phi' = 0$
6: $\quad$ **while** $\phi' < 2\pi$ **do**
7: $\quad\quad x' = r'\cos\phi'$; $\quad y' = r'\sin\phi'$
8: $\quad\quad x = -x'\sin\theta' - (z' - R^s)\cos\theta'$; $\quad y = y'$; $\quad z = x'\cos\theta' - (z' - R^s)\sin\theta'$ {Convert to global coordinate system}
9: $\quad\quad x_n = (x - x_{\min})/\Delta_s$; $\quad y_n = (y - y_{\min})/\Delta_s$; $\quad z_n = (z - z_{\min})/\Delta_s$
10: $\quad\quad \Sigma \mathrel{+}= \text{tex3D}(x_n, y_n, z_n)$ {Tri-linear interpolation}
11: $\quad\quad \phi' = \phi' + \Delta_s/r'$
12: $\quad$ **end while**
13: $\quad \theta' = \theta' - \Delta_s/\bar{t}$
14: **end while**
15: D_$\mathbf{g}$[threadIdx.x][blockIdx.x][blockIdx.y] $= \Sigma\Delta_s^2$

Implementation of the backprojection operator $\mathbf{H}^{\dagger}_{\text{int}}$ was very similar to the implementation of $\mathbf{H}_{\text{int}}$. The operators $\mathbf{D}^{\dagger}$ and $\mathbf{H}^{e\dagger}$ were calculated on CPUs while $\mathbf{G}^{\dagger}$ was calculated by

use of GPUs. The pseudo-codes are provided in Algs. 5 and 6. We made use of the CUDA function 'atomicAdd' to add weights to global memory from each thread.

Algorithm 5 Implementation of $\boldsymbol{\alpha}'_{\text{int}} = \mathbf{G}^{\dagger}\mathbf{g}'$ (on host)

Input: $\mathbf{g}'$
Output: $\boldsymbol{\alpha}'_{\text{int}}$
1: T_$\mathbf{g}' \leftarrow \mathbf{g}'$ {Bound data to texture memory}
2: K_srtT $\langle\langle\langle \quad (N_v, N_t), (N_r, 1, 1) \quad \rangle\rangle\rangle$ (D_$\boldsymbol{\alpha}'_{\text{int}}$)
3: $\boldsymbol{\alpha}'_{\text{int}} \leftarrow$ D_$\boldsymbol{\alpha}'_{\text{int}}$ {Copy data from global memory to host}

Algorithm 6 Implementation of kernel K_srtT $\langle\langle\langle \quad (N_v, N_t), (N_r, 1, 1) \quad \rangle\rangle\rangle$

Input: D_$\boldsymbol{\alpha}'_{\text{int}}$, T_$\mathbf{g}'_{\text{int}}$
Output: D_$\boldsymbol{\alpha}'_{\text{int}}$
1: $\bar{t} = (\text{blockIdx.y})c_0\Delta_t + c_0 t_{\min}$; $\theta^s = (\text{threadIdx.x})\Delta_{\theta^s} + \theta^s_{\min}$; $\phi^s = (\text{blockIdx.x})\Delta_{\phi^s} + \phi^s_{\min}$
2: $\theta'_{\max} = \arccos\big(((R^s)^2 + \bar{t}^2 - R^2)/(2\bar{t}R^s)\big)$; $\theta' = \theta'_{\max}$
3: **while** $\theta' > 0$ **do**
4: $z' = \bar{t}\cos\theta'$; $r' = \bar{t}\sin\theta'$; $\phi' = 0$
5: **while** $\phi' < 2\pi$ **do**
6: $x' = r'\cos\phi'$; $y' = r'\sin\phi'$
7: $x = -x'\sin\theta - (z' - R')\cos\theta$; $y = y'$; $z = x'\cos\theta - (z' - R')\sin\theta$ {Convert to global coordinate system}
8: $x_n = (x - x_{\min})/\Delta_s$; $y_n = (y - y_{\min})/\Delta_s$; $z_n = (z - z_{\min})/\Delta_s$
9: $n_x = \text{floor}(x_n)$; $n_y = \text{floor}(y_n)$; $n_z = \text{floor}(z_n)$
10: D_$\boldsymbol{\alpha}'_{\text{int}}[n_z][n_y][n_x] \mathrel{+}= \Delta_s^2(n_x + 1 - x_n)(n_y + 1 - y_n)(n_z + 1 - z_n)$T_$\mathbf{g}'_{\text{int}}$[threadIdx.x][blockIdx.x][blockIdx.y] {Add weights to one of the eight neighboring nodes by use of 'atomicAdd'; Repeat this operation for all other seven neighboring nodes}
11: $\phi' = \phi' + \Delta_s/r'$
12: **end while**
13: $\theta' = \theta' - \Delta_s/\bar{t}$
14: **end while**

6.3.4 Implementation of $\mathbf{H}_{\text{sph}}$ and $\mathbf{H}^{\dagger}_{\text{sph}}$

Implementation of the forward projection operation for the spherical-voxel-based imaging model is distinct from that of the interpolation-based model. The major difference is that

calculation of each element of the data vector for the spherical-voxel-based imaging model requires the accumulation of the contributions from all voxels because the model is expressed in the temporal frequency domain. Because of this, the amount of computation required to calculate each data sample in the spherical-voxel-based imaging model is almost identical, simplifying the parallelization strategy.

We proposed a parallelization strategy that was inspired by one applied in advanced MRI reconstruction [98] and is summarized as follows. Discrete samples of $\tilde{p}_0(f)$ defined in Eqn. (5.4) were precalcualted and stored as a vector $\tilde{\mathbf{p}}_0$ in constant memory. Because the size of the input vector $\boldsymbol{\alpha}_{\text{sph}}$ is often too large to fit in the constant memory, we divided $\boldsymbol{\alpha}_{\text{sph}}$ into sub-vectors that matched the capacity of the constant memory. We employed a CPU loop to copy every sub-vector sequentially to the constant memory and call the GPU kernel function to accumulate a partial summation. The major advantage of this design is that the total number of global memory visits to calculate one data sample is reduced to the number of sub-vectors.

Implementation of the projection operator for the spherical-voxel-based imaging model generally involves more arithmetic operations than does the interpolation-based imaging model. Moreover, the spherical-voxel-based imaging model has been employed to compensate for the finite aperture size effect of transducers [105, 110], which makes the computation even more burdensome. Because of this, we further developed an implementation that employed multiple GPUs. The pseudo-codes of the projection operation are provided in Algs. 7, 8, and 9. We created N_{pth} pthreads on CPUs by use of the 'pthread.h' library. Here, we denote the threads on CPUs by 'pthread' to distinguish from threads on GPUs. We divided the input vector $\boldsymbol{\alpha}_{\text{sph}}$ into N_{pth} sub-vectors (denoted by $\boldsymbol{\alpha}_{\text{pth}}$'s) of equal size and declared an output vector $\tilde{\mathbf{u}}'_{\text{sph}}$ of dimension $N_{\text{pth}} N_r N_v N_f$. By calling the pthread function 'fwd_pthread', N_{sph} pthreads simultaneously calculated the projection. Each pthread projected an $\boldsymbol{\alpha}_{\text{pth}}$ to a partial voltage data vector $\tilde{\mathbf{u}}'_{\text{pth}}$ that filled in the larger vector $\tilde{\mathbf{u}}'_{\text{sph}}$. Once all pthreads finished filling their $\tilde{\mathbf{u}}'_{\text{pth}}$ into $\tilde{\mathbf{u}}'_{\text{sph}}$, the projection data $\tilde{\mathbf{u}}_{\text{sph}}$ were obtained by a summation of the N_{pth} $\tilde{\mathbf{u}}'_{\text{pth}}$'s.

Implementation of the backprojection operator was similar except the dividing and looping were over the vector $\tilde{\mathbf{u}}_{\text{sph}}$ instead of $\boldsymbol{\alpha}_{\text{sph}}$. The pseudo-codes for the backprojection operation are provided in Algs. 10, 11, and 12.

Algorithm 7 Implementation of $\tilde{\mathbf{u}}_{\text{sph}} = \mathbf{H}_{\text{sph}}\boldsymbol{\alpha}_{\text{sph}}$ (on host)

Input: $\boldsymbol{\alpha}_{\text{sph}}$, $\tilde{\mathbf{p}}_0$
Output: $\tilde{\mathbf{u}}_{\text{sph}}$

for $n_{\text{pth}} = 0$ **to** $N_{\text{pth}} - 1$ **do**
    parm_fwdarg[n_{pth}].$n_{\text{pth}} = n_{\text{pth}}$
    parm_fwdarg[n_{pth}].$\tilde{p}_0$ = &$\tilde{\mathbf{p}}_0$[0]
    parm_fwdarg[n_{pth}].α_{pth}=&$\boldsymbol{\alpha}_{\text{sph}}[n_{\text{pth}} N_x N_y N_z / N_{\text{pth}}]$
    parm_fwdarg[n_{pth}].$\tilde{u}'_{\text{pth}}$=&$\tilde{\mathbf{u}}'_{\text{sph}}[n_{\text{pth}} N_r N_v N_f]$ {Pass addresses of arrays to each pthread}
    pthread_create(&pthreads[n_{pth}], NULL, fwd_pthread, (void *)(parm_fwdarg+n_{pth})) {Call function fwd_pthread}
end for
for $n_{\text{pth}} = 0$ **to** $N_{\text{pth}} - 1$ **do**
    for $n = 0$ **to** $N_r N_v N_f$ **do**
        $\tilde{\mathbf{u}}_{\text{sph}}[n]$ += $\tilde{\mathbf{u}}'_{\text{sph}}[n + n_{\text{pth}} N_r N_v N_f]$
    end for
end for

6.4 Descriptions of Numerical Studies

The computational efficiency and accuracy of the proposed GPU-based implementations of the FBP algorithm and projection/backprojection operators for use with iterative image reconstruction algorithms were quantified in computer-simulated and experimental PACT imaging studies.

6.4.1 Computer-Simulation Studies

Numerical Phantom: The numerical phantom consisted of 9 uniform spheres that were blurred by a 3D Gaussian kernel possessing a full width at half maximum (FWHM) of 0.77-mm. The phantom was contained within a cuboid of size $29.4 \times 29.4 \times 61.6$-mm^3. A 2D image corresponding to the plane $y = 0$ through the phantom is shown in Fig. 6.2-(a).

Simulated Projection Data: The measurement surface was a sphere of radius $R^s = 65$-mm. corresponding to an exsiting PACT imaging system [15, 110]. As described in Section 6.3, ideal point-like transducers were uniformly distributed over 128 rings and 90 tomographic

Algorithm 8 Implementation of function fwd_pthread (on host)

Input: n_{pth}, $\tilde{\mathbf{p}}_0$, $\boldsymbol{\alpha}_{\text{pth}}$, $\tilde{\mathbf{u}}'_{\text{pth}}$
Output: $\tilde{\mathbf{u}}'_{\text{pth}}$

C_$\tilde{\mathbf{p}}_0 \leftarrow \tilde{\mathbf{p}}_0$ {Copy from host to constant memory}
for $n_x = 0$ **to** $N_x/N_{\text{pth}} - 1$ **do**
    $x = (n_x + n_{\text{pth}} N_x/N_{\text{pth}})\Delta_s + x_{\min}$
    for $n_y = 0$ **to** $N_y - 1$ **do**
        $y = n_y \Delta_s + y_{\min}$
        C_$\boldsymbol{\alpha}_{\text{pth}} \leftarrow \boldsymbol{\alpha}_{\text{pth}}[n_x][n_y][:]$ {Copy from host to constant memory}
        K_fwdsph $\langle\langle\langle \quad (N_v, N_r), (N_f, 1, 1) \quad \rangle\rangle\rangle$ $(x, y,$ D_$\tilde{\mathbf{u}}'_{\text{pth}})$
    end for
end for
$\tilde{\mathbf{u}}'_{\text{pth}} \leftarrow$ D_$\tilde{\mathbf{u}}'_{\text{pth}}$ {Copy from global memory to host}

views. The 128 rings covered the full π polar angle, i.e., $\theta^s_{\min} = \pi/256$, while the 90 views covered the full 2π azimuth angle. The speed of sound was set at $c_0 = 1.54$-mm/μs. We selected the Grüneisen coefficient as $\Gamma = \beta c_0^2/C_p = 2,000$ of arbitrary units (a.u.). For each transducer, we analytically calculated 1022 temporal samples of the pressure function at the sampling rate of $f_{\text{sam}} = 20$-MHz by use of Eqn. (2.1). Because we employed a smooth object function, the pressure data were calculated by the following two steps: Firstly, we calculated temporal samples of pressure function $p_{\text{us}}(\mathbf{r}^s, t)$ that corresponds to the 9 uniform spheres by [68, 113]

$$p_{\text{us}}(\mathbf{r}^s, t)|_{t=k\Delta_t} = \sum_{i=0}^{8} \begin{cases} A_i \Big[-\frac{\beta c_0^3}{C_p |\mathbf{r}^s - \mathbf{r}_i|} t + \frac{\beta c_0^2}{2} \Big]_{t=k\Delta_t}, & \text{if } \big| c_0 k\Delta_t - |\mathbf{r}^s - \mathbf{r}_i| \big| \le R_i \\ 0, & \text{otherwise} \end{cases} \tag{6.14}$$

where $\mathbf{r}_i$, R_i and A_i denote the center location, the radius and the absorbed energy density of the i-th sphere, respectively. Subsequently, we convolved $p_{\text{us}}(\mathbf{r}^s, t)$ with a one-dimensional (1D) Gaussian kernel with FWHM = 0.5-μs [5] to produce the pressure data. From the simulated pressure data, we calculated the temporal-frequency spectrum by use of fast Fourier transform (FFT), from which we created an alternative data vector that contained 511 frequency components occupying $(0, 5]$-MHz for each transducer. The simulated projection data in either the time domain or the temporal frequency domain will hereafter be referred to as "128×90"-data. By undersampling the "128×90"-data uniformly over rings and tomographic views, we created three subsets that contained varying number of transducers.

Algorithm 9 Implementation of Kernel K_fwdsph $\langle\langle\langle \quad (N_v, N_r), (N_f, 1, 1) \quad \rangle\rangle\rangle$

Input: x, y, D_$\tilde{\mathbf{u}}'_{\text{pth}}$, C_$\boldsymbol{\alpha}_{\text{pth}}$, C_$\tilde{\mathbf{p}}_0$

Output: D_$\tilde{\mathbf{u}}'_{\text{pth}}$

1: $\theta^s = (\text{blockIdx.y})\Delta_{\theta^s} + \theta^s_{\min}$; $\quad \phi^s = (\text{blockIdx.x})\Delta_{\phi^s} + \phi^s_{\min}$; $\quad f = (\text{threadIdx.x})\Delta_f + f_{\min}$

2: $z^s = R^s \cos\theta^s$; $\quad x^s = R^s \sin\theta^s \cos\phi^s$; $\quad y^s = R^s \sin\theta^s \sin\phi^s$ {Calculate locations of transducers}

3: $\Sigma^r = 0$; $\quad \Sigma^i = 0$ {Initiate the partial summation including the real and imaginary parts}

4: **for** $n_z = 0$ **to** $N_z - 1$ **do**

5: $\quad z = n_z \Delta_s + z_{\min}$

6: $\quad d = \left((x - x^s)^2 + (y - y^s)^2 + (z - z^s)^2\right)^{1/2}$

7: $\quad \tilde{h}^r = \cos(2\pi f d/c_0)/(2\pi d)$; $\quad \tilde{h}^i = -\sin(2\pi f d/c_0)/(2\pi d)$ {Calculate SIR; Example here assumes point-like transducers}

8: $\quad \Sigma^r \mathrel{+}= \text{C\_}\boldsymbol{\alpha}_{\text{pth}}[n_z]\left(\tilde{h}^r \text{C\_}\tilde{\mathbf{p}}_0[\text{threadIdx.x}].r - \tilde{h}^i \text{C\_}\tilde{\mathbf{p}}_0[\text{threadIdx.x}].i\right)$

9: $\quad \Sigma^i \mathrel{+}= \text{C\_}\boldsymbol{\alpha}_{\text{pth}}[n_z]\left(\tilde{h}^r \text{C\_}\tilde{\mathbf{p}}_0[\text{threadIdx.x}].i + \tilde{h}^i \text{C\_}\tilde{\mathbf{p}}_0[\text{threadIdx.x}].r\right)$

10: **end for**

11: D_$\tilde{\mathbf{u}}'_{\text{pth}}$[blockIdx.y][blockIdx.x][threadIdx.x].$r \mathrel{+}= \Sigma^r$

12: D_$\tilde{\mathbf{u}}'_{\text{pth}}$[blockIdx.y][blockIdx.x][threadIdx.x].$i \mathrel{+}= \Sigma^i$

These data sets will be referred to as "64×90"-data, "64×45"-data, and "32×45"-data, where the two numbers specify the number of rings and the number of tomographic views, respectively.

Reconstruction Algorithms: The GPU accelerated FBP algorithm was employed to reconstruct the object function sampled on a 3D Cartesian grid with spacing $\Delta_s = 0.14$-mm. The dimension of the reconstructed images $\hat{\boldsymbol{\alpha}}_{\text{fbp}}$ was $210 \times 210 \times 440$.

We employed an iterative image reconstruction algorithm that sought to minimize a penalized least-squares (PLS) objective [31, 69]. Two versions of the reconstruction algorithm were developed that utilized the interpolation-based imaging model and the spherical-voxel-based imaging model respectively. The two versions sought to solve the optimization problems by use of the linear conjugate gradient (CG) method [96, 33]:

$$\hat{\boldsymbol{\alpha}}_{\text{int}} = \arg\min_{\boldsymbol{\alpha}_{\text{int}}} \|\mathbf{u} - \mathbf{H}_{\text{int}} \boldsymbol{\alpha}_{\text{int}}\|^2 + \mu R(\boldsymbol{\alpha}_{\text{int}}), \tag{6.15}$$

Algorithm 10 Implementation of $\boldsymbol{\alpha}'_{\text{sph}} = \mathbf{H}^{\dagger}_{\text{sph}}\tilde{\mathbf{u}}$ (on host)

Input: $\tilde{\mathbf{u}}$, $\tilde{\mathbf{p}}_0$
Output: $\boldsymbol{\alpha}'_{\text{sph}}$

for $n_{\text{pth}} = 0$ **to** $N_{\text{pth}} - 1$ **do**
    parm_bwdarg[n_{pth}].$n_{\text{pth}} = n_{\text{pth}}$
    parm_bwdarg[n_{pth}].$\tilde{p}_0$ = &$\tilde{\mathbf{p}}_0$[0]
    parm_bwdarg[n_{pth}].$\tilde{u}_{\text{pth}}$=&$\tilde{\mathbf{u}}$[$n_{\text{pth}} N_r N_v N_f / N_{\text{pth}}$]
    parm_bwdarg[n_{pth}].α''_{pth}=&$\boldsymbol{\alpha}''_{\text{sph}}$[$n_{\text{pth}} N_x N_y N_z$] {Pass addresses of arrays to each pthread}
    pthread_create(&pthreads[n_{pth}], NULL, bwd_pthread, (void *)(parm_bwdarg+n_{pth})) {Call function bwd_pthread}
end for
for $n_{\text{pth}} = 0$ **to** $N_{\text{pth}} - 1$ **do**
    for $n = 0$ **to** $N_x N_y N_z$ **do**
        $\boldsymbol{\alpha}'_{\text{sph}}[n]$ += $\boldsymbol{\alpha}''_{\text{sph}}[n + n_{\text{pth}} N_x N_y N_z]$
    end for
end for

and

$$\hat{\boldsymbol{\alpha}}_{\text{sph}} = \arg\min_{\boldsymbol{\alpha}_{\text{sph}}} \|\tilde{\mathbf{u}} - \mathbf{H}_{\text{sph}}\boldsymbol{\alpha}_{\text{sph}}\|^2 + \mu R(\boldsymbol{\alpha}_{\text{sph}}), \tag{6.16}$$

respectively, where $R(\boldsymbol{\alpha})$ is a regularizing penalty term whose impact is controlled by the regularization parameter μ. The penalty term was employed only when processing the experimental data as described in Section 6.4-B. The reconstruction algorithms required computation of one projection and one backprojection operation at each iteration. Hereafter, the two reconstruction algorithms will be referred to as PLS-Int and PLS-Sph algorithms, respectively. We set $\Delta_s = 0.14$-mm. Therefore, both the dimensions of $\hat{\boldsymbol{\alpha}}_{\text{int}}$ and $\hat{\boldsymbol{\alpha}}_{\text{sph}}$ were $210 \times 210 \times 440$.

Performance Assessment: We compared the computational times of 3D image reconstruction corresponding to the GPU- and CPU-based implementations. The CPU-based implementations of the PLS-Int and PLS-Sph algorithms take several days to complete a single iteration even for the "32×45"-data. Therefore, we only recorded the computational time for the CPU-based implementations to complete a single iteration when the data

Algorithm 11 Implementation of function bwd_pthread (on host)

Input: n_{pth}, $\tilde{\mathbf{p}}_0$, $\tilde{\mathbf{u}}_{\text{pth}}$, $\boldsymbol{\alpha}''_{\text{pth}}$
Output: $\boldsymbol{\alpha}''_{\text{pth}}$
1: C_$\tilde{\mathbf{p}}_0 \leftarrow \tilde{\mathbf{p}}_0$ {Copy from host to constant memory}
2: **for** $n_r = 0$ **to** $N_r/N_{\text{pth}} - 1$ **do**
3: $\quad\theta^s = (n_r + n_{\text{pth}} N_r/N_{\text{pth}})\Delta_{\theta^s} + \theta^s_{\text{min}}; \quad z^s = R^s \cos\theta^s; \quad r^s = R^s \sin\theta^s$
4: $\quad$**for** $n_v = 0$ **to** $N_v - 1$ **do**
5: $\quad\quad\phi^s = n_v \Delta_{\phi^s} + \phi^s_{\text{min}}; \quad x^s = r^s \cos\phi^s; \quad y^s = r^s \sin\phi^s$
6: $\quad\quad$C_$\tilde{\mathbf{u}}_{\text{pth}} \leftarrow \tilde{\mathbf{u}}_{\text{pth}}[n_r][n_v][:]$ {Copy from host to constant memory}
7: $\quad\quad$K_bwdsph $\langle\langle\langle \quad (N_y, N_x), (N_z, 1, 1) \quad \rangle\rangle\rangle$ $(x^s, y^s, z^s$ D_$\boldsymbol{\alpha}''_{\text{pth}})$
8: $\quad$**end for**
9: **end for**
10: $\boldsymbol{\alpha}''_{\text{pth}} \leftarrow$ D_$\boldsymbol{\alpha}''_{\text{pth}}$ {Copy from global memory to host}

vector contained a single transducer. We assumed that the computational times were linearly proportional to the number of transducers in the data sets because the CPU-based implementations are sequential.

The GPU-based implementations employed the single-precision floating-point format rather than the conventional double-precision utilized by CPU-based implementations. In order to quantify how the single-precision floating-point format would degrade the image accuracy, we calculated the root mean square error (RMSE) between the reconstructed image and the phantom defined by:

$$\text{RMSE} = \sqrt{\frac{1}{N}(\hat{\boldsymbol{\alpha}} - \boldsymbol{\alpha})^{\text{T}}(\hat{\boldsymbol{\alpha}} - \boldsymbol{\alpha})}, \tag{6.17}$$

where $\boldsymbol{\alpha}$ and $\hat{\boldsymbol{\alpha}}$ are the samples of the phantom and the coefficients of the reconstructed images respectively.

Hardware Specifications: All implementations were tested on the platform consisted of dual quad-core Intel(R) Xeon (R) CPUs with a clock speed 2.40-GHz. The GPU-based implementations of the FBP and the PLS-Int algorithms were tested on a single Tesla C2050 GPU, while the PLS-Sph algorithm was tested on 8 Tesla C1060 GPUs.

Algorithm 12 Implementation of Kernel K_bwdsph $\langle\langle\langle \quad (N_y, N_x), (N_z, 1, 1) \quad \rangle\rangle\rangle$

Input: x^s, y^s, z^s, D_$\boldsymbol{\alpha}''_{\text{pth}}$, C_$\tilde{\mathbf{u}}_{\text{pth}}$, C_$\tilde{\mathbf{p}}_0$

Output: D_$\boldsymbol{\alpha}''_{\text{pth}}$

1: $x = (\text{blockIdx.y})\Delta_s + x_{\min}$; $\quad y = (\text{blockIdx.x})\Delta_s + y_{\min}$; $\quad z = (\text{threadIdx.x})\Delta_s + z_{\min}$

2: $d = \Big((x - x^s)^2 + (y - y^s)^2 + (z - z^s)^2\Big)^{1/2}$; $\quad \Sigma = 0$ {Initiate the partial summation}

3: **for** $n_f = 0$ **to** $N_f - 1$ **do**

4: $\quad f = n_f\Delta_f + f_{\min}$

5: $\quad \tilde{h}^r = \cos(2\pi f d/c_0)/(2\pi d)$; $\quad \tilde{h}^i = -\sin(2\pi f d/c_0)/(2\pi d)$ {Calculate SIR; Example here assumes point-like transducers}

6: $\quad \Sigma+ = \text{C\_}\tilde{\mathbf{u}}_{\text{pth}}[n_f].r\Big(\tilde{h}^r\text{C\_}\tilde{\mathbf{p}}_0[n_f].r - \tilde{h}^i\text{C\_}\tilde{\mathbf{p}}_0[n_f].i\Big) + \text{C\_}\tilde{\mathbf{u}}_{\text{pth}}[n_f].i\Big(\tilde{h}^i\text{C\_}\tilde{\mathbf{p}}_0[n_f].r + \tilde{h}^r\text{C\_}\tilde{\mathbf{p}}_0[n_f].i\Big)$

7: **end for**

8: D_$\boldsymbol{\alpha}''_{\text{pth}}$[blockIdx.y][blockIdx.x][threadIdx.x] += Σ

6.4.2 Experimental Studies

The FBP, PLS-Int and PLS-Sph algorithms were investigated by use of an existing data set corresponding to a live mouse [15, 110]. The scanning geometry and dimensions were the same as those employed in the computer-simulation studies except that only 64 rings were uniformly distributed over the polar angle ranging from 14° to 83°. The transducers were of size $2 \times 2\text{-mm}^2$. The raw data were acquired at 180 tomographic views, which are referred to as "full data". We undersampled the "full data" uniformly over the tomographic views, constructing a subset containing 45 tomographic views. The subset will be referred to as "quarter data".

Unlike in the idealized computer-simulation studies, the transducer response has to be compensated for when processing the experimental data. When implementing the FBP algorithm, the EIR was compensated for by a direct Fourier deconvolution, expressed in temporal frequency domain as [51]:

$$\tilde{p}(\mathbf{r}^s, f) = \frac{\tilde{u}(\mathbf{r}^s, f)}{\tilde{h}^e(f)}\tilde{W}(f), \tag{6.18}$$

where $\tilde{W}(f)$ is a window function for noise suppression. In this study, we adopted the Hann window function defined as:

$$\tilde{W}(f) = \frac{1}{2}\Big[1 - \cos(\pi \frac{f_c - f}{f_c})\Big], \tag{6.19}$$

where the cutoff frequency was chosen as $f_c = 5$-MHz. When applying iterative image reconstruction algorithms, the transducer effects were implicitly compensated for during iteration by employing imaging models that incorporates the transducer charactertics [105, 110]. We incorporated the EIR into the interpolation-based imaging model while incorporating both the EIR and the SIR into the spherical-voxel-based imaging model.

For both PLS-Int and PLS-Sph algorithms, we employed a quadratic smoothness penalty to mitigate measurement noise [31]:

$$R(\boldsymbol{\alpha}) = \sum_{n=0}^{N-1} \big([\boldsymbol{\alpha}]_n - [\boldsymbol{\alpha}]_{n_x}\big)^2 + \big([\boldsymbol{\alpha}]_n - [\boldsymbol{\alpha}]_{n_y}\big)^2 + \big([\boldsymbol{\alpha}]_n - [\boldsymbol{\alpha}]_{n_z}\big)^2, \tag{6.20}$$

where n_x, n_y and n_z were the indices of the neighboring voxels before the n-th voxel along the three Cartesian axes, respectively.

6.5 Numerical Results

6.5.1 Computational Efficiency

As shown in Table 6.1, the GPU-based implementations took less than 0.1%, 0.4% and 0.8% of the computational times required by corresponding CPU-based implementations for the FBP, the PLS-Int, and the PLS-Sph algorithms, respectively. The relative computational times for the GPU-based implementations are nearly linearly proportional to the amount of data. Note that the "64×90"-data and the "quarter data" are of the same size. However, the computational times of the "quarter data" are more than 1.8 times those of the "64×90"-data. This is because the calculation of the SIR increases the computational complexity of the reconstruction algorithm.

Table 6.1: Computational times of the 3D image reconstructions by use of the CPU- and GPU-based implementations

Data sets	FBP [sec]		PLS-Int [min/iteration]		PLS-Sph [min/iteration]	
	CPU	GPU	CPU	GPU	CPU	GPU
"32×45"	$6,189$	6	$2,448$	20	$7,961$	22
"64×45"	$12,975$	12	$4,896$	35	$15,923$	43
"64×90"	$26,190$	23	$9,792$	68	$31,845$	86
"128×90"	$53,441$	46	-	-	-	-
"quarter data"	$12,975$	12	$4,896$	35	$19,776$	78
"full data"	$53,441$	46	$19,968$	137	$79,177$	313

6.5.2 Computational Accuracy

Images reconstructed by use of the CPU- and GPU-based implementations of the FBP algorithm are almost identical. From the "128×90"-data, in which case, transducers were densely distributed over the measurement surface, both implementations reconstructed accurate images, as shown Fig. 6.2-(b) and -(c). The profiles along the three arrows in Fig. 6.2 are plotted in Fig. 6.5-(a), suggesting a nearly exact reconstruction. As expected, when the amount of measurement data are reduced, the reconstructed images contain more artifacts as shown in Fig. 6.3. However, the images reconstructed by use of GPU- and CPU-based implementations remain indistinguishable. The plots of the RMSE versus the amount of measurement data employed in Fig. 6.4 overlap, also suggesting the single-precision floating-point format employed by the GPU-based implementation has little impact on the computational accuracy.

The GPU-based implementations of the PLS-Int and PLS-Sph algorithms both reconstructed accurate images as displayed in Fig. 6.6. As expected, the images reconstructed by use of both iterative algorithms contain fewer artifacts than do those reconstructed by use of the FBP algorithm from the same amount of data. Unlike the images reconstructed by use of the FBP algorithm from the "64×90"-data (Fig. 6.3-(a) or -(d)), the images reconstructed by use of both iterative algorithms (Fig. 6.6-(a) and -(d)) appear to be identical to the numerical phantom. The profiles along the two arrows in Fig. 6.6-(a) and -(d) are plotted in Fig. 6.5-(b), further confirming the computational accuracy of iterative image reconstruction algorithms. The plots of the RMSE versus the amount of measurement data employed in

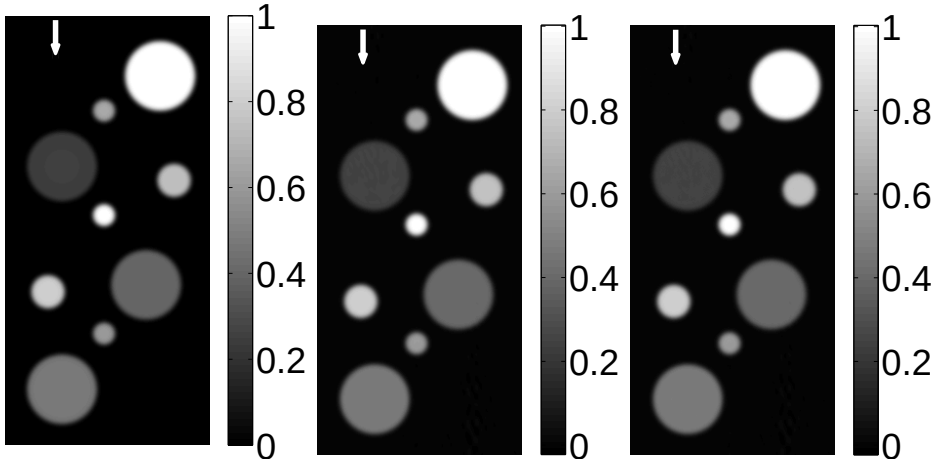

(a) (b) (c)

Figure 6.2: Slices corresponding to the plane $y = 0$ of (a) the phantom and the images reconstructed by use of (b) the CPU-based and (c) the GPU-based implementations of the FBP algorithm from the "128×90"-data.

Fig. 6.4 suggest the iterative image reconstruction algorithms in general outperform the FBP algorithm from the same amount of data.

6.5.3 Experimental Results

The maximum intensity projection (MIP) of the 3D mouse images reconstructed by use of the GPU-based implementations reveal the mouse body vasculature as shown in Fig. 6.7. Images reconstructed by use of both the PLS-Int and the PLS-Sph algorithms appear to have cleaner background than do the images reconstructed by use of the FBP algorithm from the same amount of data. All images reconstructed by iterative algorithms were obtained by 20-iterations starting with uniform zeros as the initial guess. The PLS-Int algorithm took approximately a half day and 2 days to process the "quarter data" and the "full data" respectively. The PLS-Sph algorithm took approximately one day and 4 days to process the "quarter data" and the "full data" respectively. Alternatively, if the CPU-based implementations were utilized, the PLS-Int algorithm would take an estimated 68 days and 277 days to process the "quarter data" and the "full data" respectively. The PLS-Sph algorithm would take an estimated 275 days and $1,100$ days to process the "quarter data" and the "full data" respectively.

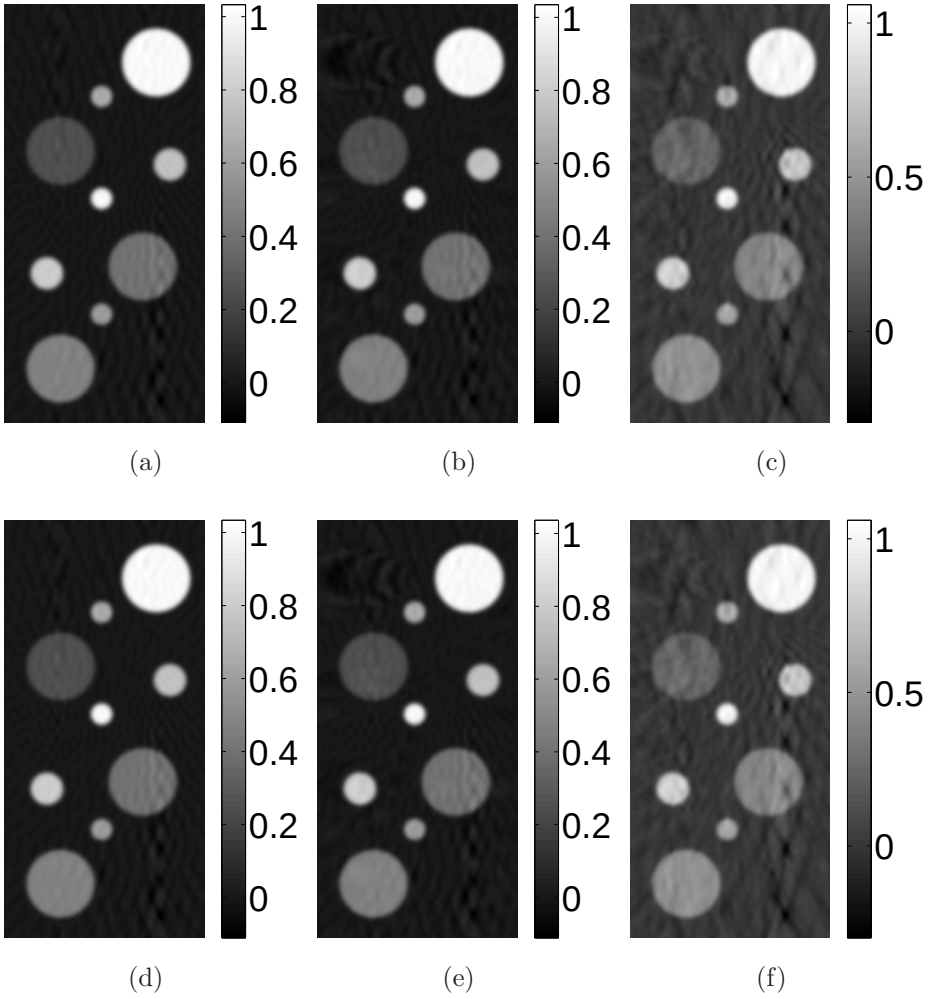

Figure 6.3: Slices corresponding to the plane $y = 0$ of the images reconstructed by use of the FBP algorithm with (a) the CPU-based implementation from the "64×90"-data, (b) the CPU-based implementation from the "64×45"-data, (c) the CPU-based implementation from the "32×45"-data, (d) the GPU-based implementation from the "64×90"-data, (e) the GPU-based implementation from the "64×45"-data, and (f) the GPU-based implementation from the "32×45"-data.

6.6 Discussion and Conclusion

In this study, we developed and investigated GPU-based implementations of the FBP algorithm and two pairs of projection/backprojection operators for 3D PACT. Our implementation of the FBP algorithm improved the computational efficiency over $1,000$ times

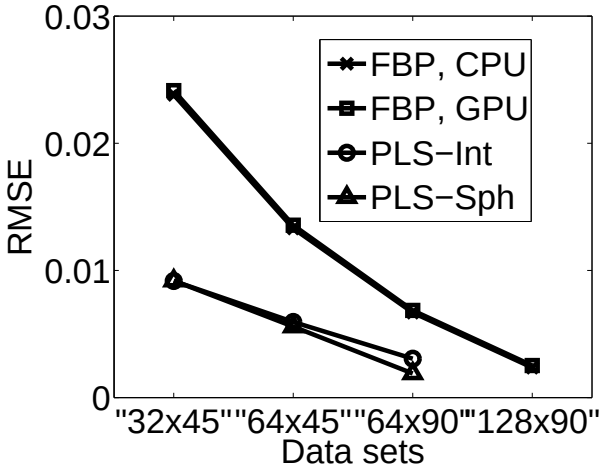

Figure 6.4: Plots of the RMSE against the amount of data by use of the FBP, the PLS-Int and the PLS-Sph algorithms.

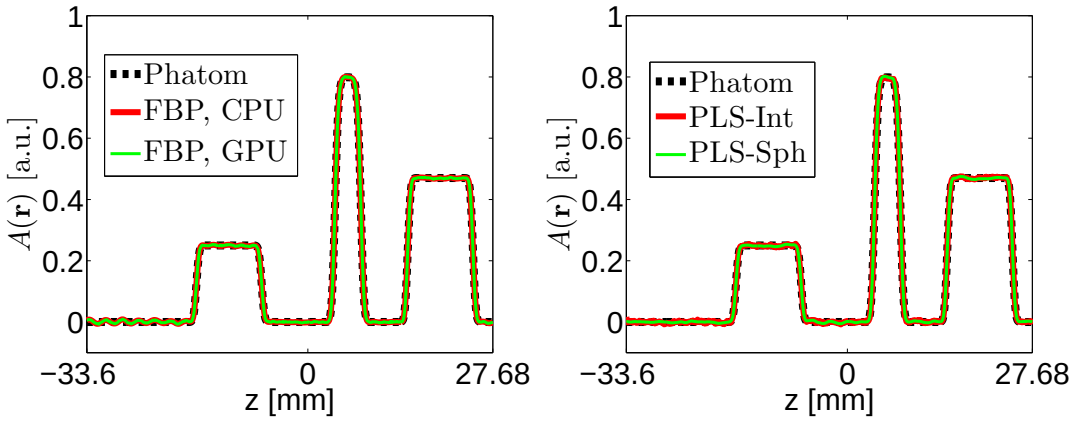

(a) (b)

Figure 6.5: Profiles along the line $(x, y) = (-6.58, 0)$-mm of the images reconstructed by use of (a) the CPU- and GPU-based implementations of the FBP algorithm from the "128×90"-data, and (b) the GPU-based implementations of the PLS-Int and the PLS-Sph algorithms from the "64×90"-data.

compared to the CPU-based implementation. More importantly, our implementations of the projection/backprojection operators demonstrate the feasibility of 3D iterative image reconstruction in practice[109, 110].

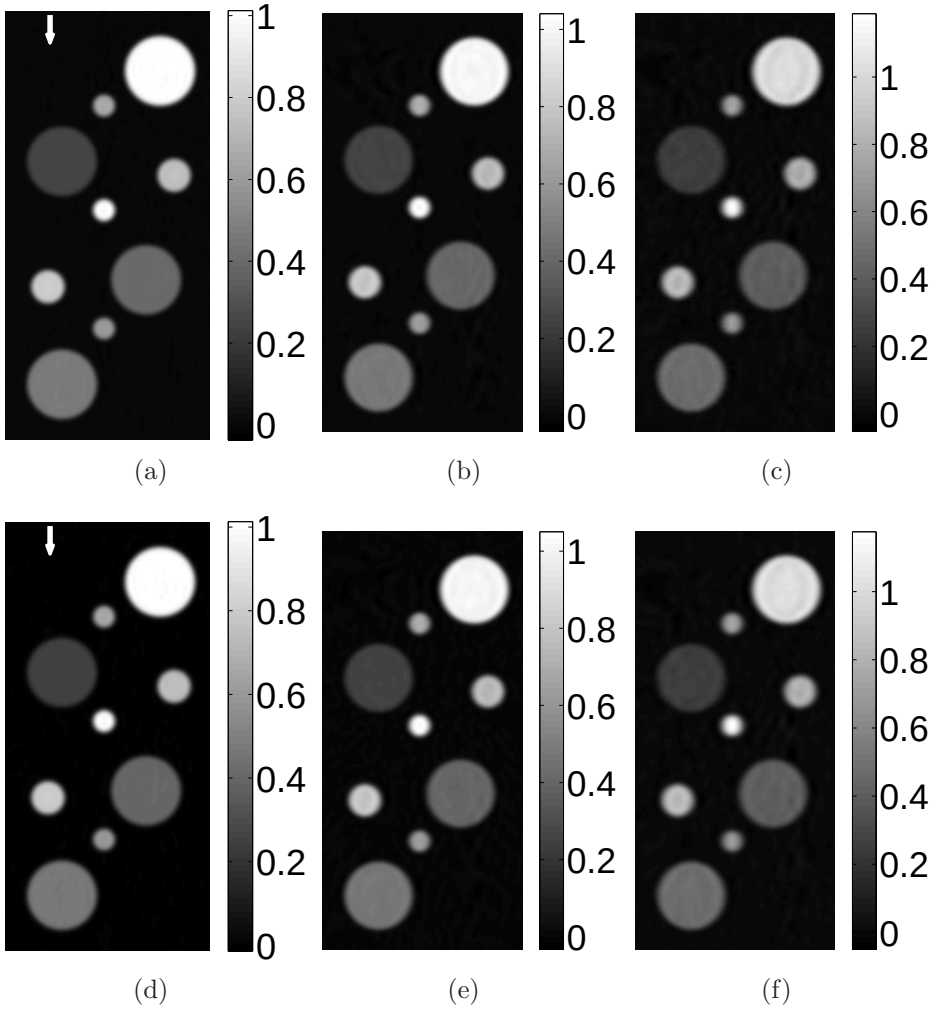

Figure 6.6: Slices corresponding to the plane $y = 0$ of the images reconstructed by use of the GPU-based implementations of (a) the PLS-Int algorithm from the "64×90"-data, (b) the PLS-Int algorithm from the "64×45"-data, (c) the PLS-Int algorithm from the "32×45"-data, (d) the PLS-Sph algorithm from the "64×90"-data, (e) the PLS-Sph algorithm from the "64×45"-data, and (f) the PLS-Sph algorithm from the "32×45"-data.

Our current implementations of the iterative image reconstruction algorithms still require several days to process the densely sampled data set, which, however, can be further improved. Firstly, the amount of measurement data required for accurate image reconstruction can be further reduced by developing advanced image reconstruction methods [89, 37, 71, 110]. Secondly, the number of iterations required can be reduced by developing fast-converging optimization algorithms [10, 110, 13].

The proposed parallelization strategies by use of GPUs are of general interest. The implementation of the FBP algorithm [34] can be adapted to other analytic image reconstruction algorithms, including those described in [120, 122, 55, 35, 26]. We demonstrated the feasibility of PLS algorithm that utilized the proposed GPU-based implementations of the projection/backprojection operators. By use of these implementations, many advanced image reconstruction algorithms may also be feasible in practice [110]. Though we described our parallelization strategies for the projection/backprojection operators that utilized two discrete-to-discrete imaging models, these strategies can also be applied to other D-D imaging models [84, 28, 92, 16]. Therefore, the proposed algorithms will facilitate the further investigation and application of advanced image reconstruction algorithms in 3D PACT.

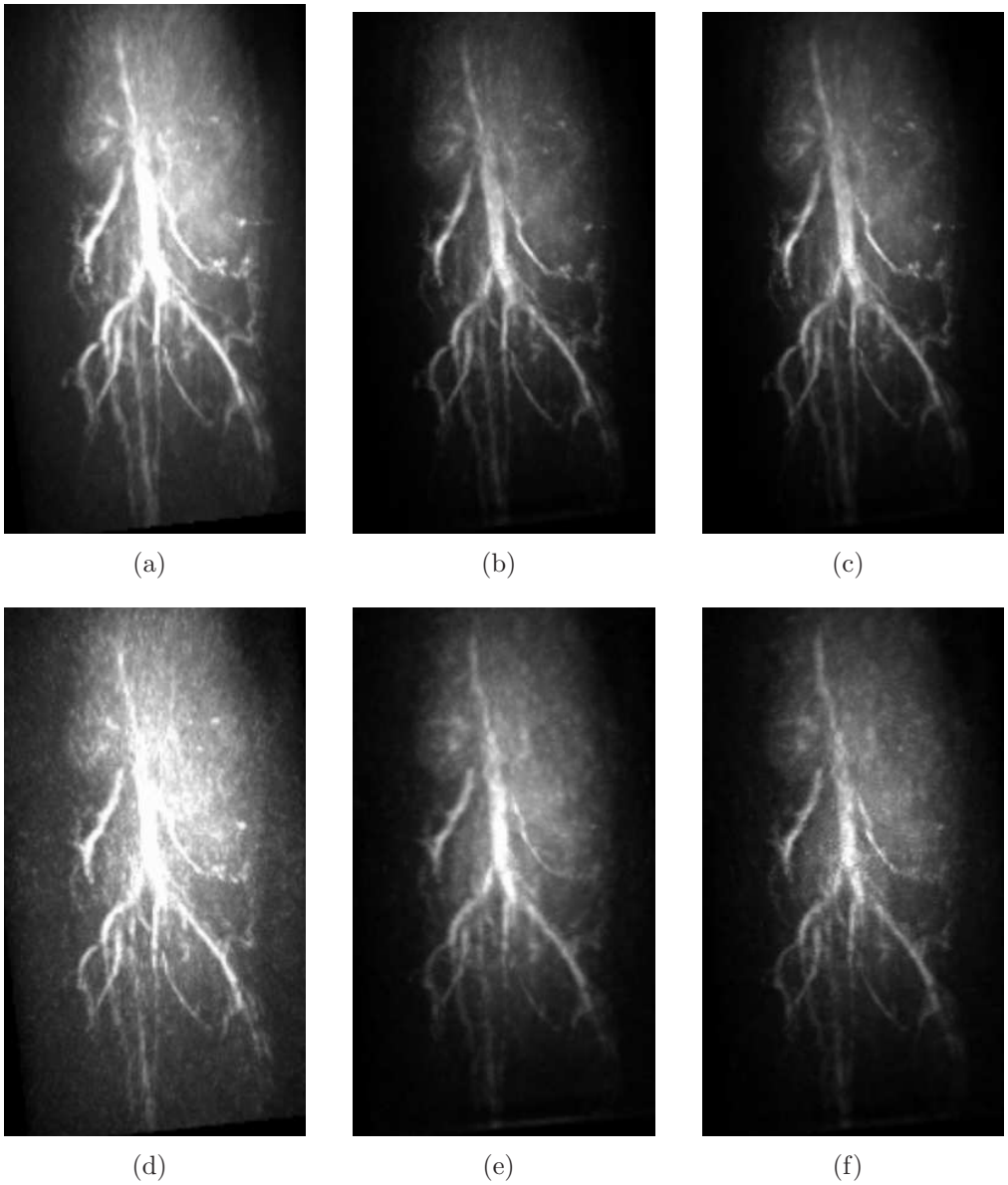

Figure 6.7: MIP renderings of the 3D images of the mouse body reconstructed by use of the GPU-based implementations of (a) the FBP algorithm from the "full data", (b) the PLS-Int algorithm from the "full data" with $\mu = 1.0 \times 10^4$, (c) the PLS-Sph algorithm from the "full data" with $\mu = 1.0 \times 10^4$, (d) the FBP algorithm from the "quarter data", (e) the PLS-Int algorithm from the "quarter data" with $\mu = 1.0 \times 10^3$, and (f) the PLS-Sph algorithm from the "quarter data" with $\mu = 1.0 \times 10^3$. The grayscale window is [0,12.0].

Chapter 7

Summary

In the dissertation, we have investigated imaging models and reconstruction algorithms for three-dimensional (3D) photoacoustic computed tomography (PACT). The contributions are summarized as following.

1. We have derived a Fourier transform-based reconstruction formula for PACT that is two orders of magnitude more computationally efficient than 3D filtered backprojection (FBP) algorithms [106].

2. We have proposed a continuous-to-discrete (C-D) imaging model that incorporates the characteristics of ultrasonic transducers [107, 105]. For the purpose of iterative image reconstruction, a spherical-voxel-based discrete-to-discrete (D-D) imaging model has been developed to approximate the C-D model. The use of the new imaging model, in conjunction with the itertiave reconstruction algorithm, has significantly improved the spatial resolution, permitting the construction of compact imaging scanners.

3. We have systematically investigated various iterative image reconstruction algorithms for small animal imaging, including the fast iterative shrinkage/thresholding algorithm (FISTA) that solves for objectives with a total variation (TV)-norm penalty [109, 110]. The results demonstrate, for the first time, the feasibility and advantages of iterative image reconstruction in practice. The TV-norm regularization in general outperforms the conventional quadratic smoothness penalty, and may reduce the amount of data required while maintaining high image quality.

4. In order to accelerate the 3D image reconstruction, we have developed graphics processing unit (GPU)-based implementations of the FBP algorithm and two pairs of

projection/backprojection operators. Our implementation of the FBP algorithm has improved the computational efficiency over $1,000$ times compared to the CPU-based implementation. The GPU-based implementations of projection/backprojection operators will directly promote the algorithm development for 3D PACT.

PACT has great potential for a wide range of biomedical imaging applications. On the other hand, as an emerging imaging modality, research on PACT image reconstruction algorithms is still at an early age comparing with other more mature imaging modalities. Therefore, there remain many important and challenging topics for future studies. For example, the assessment of image quality is commonly conducted by use of visual inspection or quantitative metrics as we discussed in Chapter 5. Development of task-based image quality assessment methods will provide a more effective guideline for system design. A related topic is the identification of the noise sources and characterization of [99] their second order statistical properties. The knowledge of noise statistics will facilitate iterative reconstruction algorithms to optimally reduce noise levels in the reconstructed images. Research in this dissertation assumes acoustically homogeneous media and ignore the effects of acoustic attenuations. Pioneers are actively developing more accurate imaging models that model the effects of acoustic heterogeneities and attenuation [72, 42, 43]. Also development of advanced image reconstruction algorithms will further improve the accuracy and efficiency of PACT image reconstruction [13, 111]. I believe that computed tomography techniques will promote PACT in clinical applications in the future.

Appendix A

Implementation of Eqn. (4.21)

Below we provide additional information regarding the numerical implementation the system matrix **H** in Eqn. (4.21) that was employed in our studies.

As described above Eqn. (4.21), an anti-aliasing filter was applied to $l_q(\mathbf{r}_n, t)$, which was implemented in the temporal frequency domain as

$$\tilde{l}'_q(\mathbf{r}_n, f) = \tilde{l}_q(\mathbf{r}_n, f)\tilde{v}(f), \tag{A.1}$$

where $\tilde{v}(f)$ is the anti-aliasing filter, and $\tilde{l}_q(\mathbf{r}_n, f)$ is the Fourier transform of $l_q(\mathbf{r}_n, t)$:

$$\tilde{l}_q(\mathbf{r}_n, f) = \int_{-\infty}^{\infty} dt\ l_q(\mathbf{r}_n, t) \exp(-\hat{\jmath}2\pi f t). \tag{A.2}$$

Here $\hat{\jmath} = \sqrt{-1}$. We defined the low-pass filter $\tilde{v}(f)$ as

$$\tilde{v}(f) = \begin{cases} 1, & \text{for} \quad 0 \le f < f_l \\ \cos(\frac{\pi}{2}\frac{f-f_l}{f_h-f_l}), & \text{for} \quad f_l \le f < f_h \\ 0, & \text{for} \quad f_h \le f \end{cases}, \tag{A.3}$$

where f_l and f_h specified a continuous decaying window in frequency space. The location of the window limits the spatial resolution we can achieve in the reconstructed images. Since $l_q(\mathbf{r}_n, t) = \frac{1}{S_q} h^s_q(\mathbf{r}_n, t) *_t p_0(t)$, its frequency spectrum can be calculated by

$$\tilde{l}_q(\mathbf{r}_n, f) = \frac{1}{S_q}\tilde{h}^s_q(\mathbf{r}_n, f)\tilde{p}_0(f), \tag{A.4}$$

where

$$\tilde{h}_q^s(\mathbf{r}_n, f) = \int_{-\infty}^{\infty} dt\ h_q^s(\mathbf{r}_n, t) \exp(-\hat{\jmath} 2\pi f t), \tag{A.5a}$$

$$\tilde{p}_0(f) = \int_{-\infty}^{\infty} dt\ p_0(t) \exp(-\hat{\jmath} 2\pi f t). \tag{A.5b}$$

It can be verified that $\tilde{h}_q^s(\mathbf{r}_n, f)$ can be calculated analytically as

$$\tilde{h}_q^s(\mathbf{r}_n, f) = \mathrm{sinc}\left(\pi f \frac{a \sin\theta \cos\phi}{c_0}\right) \mathrm{sinc}\left(\pi f \frac{a \sin\theta \sin\phi}{c_0}\right), \tag{A.6}$$

where $\mathrm{sinc}(x) = x^{-1} \sin x$. Also, $\tilde{p}_0(t)$ has an analytical form given by

$$\tilde{p}_0(f) = -\hat{\jmath} \frac{\beta c_0^3}{C_p f} \left[\frac{\Delta_s}{2c_0} \cos\left(\frac{\pi f \Delta_s}{c_0}\right) - \frac{1}{2\pi f} \sin\left(\frac{\pi f \Delta_s}{c_0}\right) \right]. \tag{A.7}$$

To obtain $l'_q(\mathbf{r}_n, k\Delta_t)$, we sampled $\tilde{l'}_q(\mathbf{r}_n, f)$ in frequency space at a rate of $K\Delta_t$ samples per Hertz, and applied the inverse discrete Fourier transform

$$l'_q(\mathbf{r}_n, k\Delta_t) = \Delta_f \sum_{k'=0}^{K-1} \exp(j \frac{2\pi k' k}{K}) \tilde{l}'_q(\mathbf{r}_n, f)\Big|_{f=k'\Delta_f}, \tag{A.8}$$

where, $\Delta_f = 1/(K\Delta_t)$. The discrete convolution in Eqn. (4.21) and the inverse discrete Fourier transform in Eqn. (A.8) were implemented by use of the fast Fourier transform.

The implementation of the conjugate gradient algorithm requires calculating Eqns. (A.6) and (A.7) at $n = 0, 1, \cdots, N-1$, $q = 0, 1, \cdots, Q-1$, and $f = k\Delta_f$ with $k = 1, 2, \cdots, K$ once for each iteration. To accelerate the computation, we developed parallel program by use of graphic processing unit (GPU). We created $N \times Q \times K$ threads with each for a pair of voxel (n), transducer location (q) and temporal frequency component (k). By use of multiple GPUs, thousands of threads can run simultaneously. This technique tremendously reduced our computational time and made the iterative reconstruction for 3D PACT feasible. For this work, it took 12 seconds and 2.5 hours per iteration respectively for the simulation and the experimental studies by use of single NVIDIA® Tesla™ C1060 computing processor.

Appendix B

Implementation of FISTA Algorithm for 3D PACT

We employed the fast iterative shrinkage thresholding algorithm (FISTA) algorithm [11, 10] to solve for the total variation (TV)-norm regularized least-squares objective defined by Eqn. (5.14). We extended the FISTA algorithm described in [10] to three-dimensional (3D) space. The pseudocodes are provided in Alg. 13.

Algorithm 13 Solver of the optimization problem defined by Eqn. (5.14)

Input: $\tilde{\mathbf{u}}$, $\boldsymbol{\alpha}^{(0)}$, β, L

Output: $\hat{\boldsymbol{\alpha}}$

1: $t^{(0)} \leftarrow 1$; $\boldsymbol{\sigma}^{(1)} \leftarrow \boldsymbol{\alpha}^{(0)}$ {Set the initial guess}
2: **for** $n = 1$ **to** N **do**
3: $\quad \boldsymbol{\alpha}^{(n)} \leftarrow \text{F\_Dnoise}\big(\boldsymbol{\sigma}^{(\mathrm{n})} - \frac{2}{\mathrm{L}}\mathbf{H}^{\dagger}(\mathbf{H}\boldsymbol{\sigma}^{(\mathrm{n})} - \tilde{\mathbf{u}}), 2\beta/\mathrm{L}\big)$
4: $\quad t^{(n+1)} \leftarrow 0.5 + 0.5\sqrt{1 + 4(t^{(n)})^2}$
5: $\quad \boldsymbol{\sigma}^{(n+1)} \leftarrow \boldsymbol{\alpha}^{(n)} + (t^{(n)} - 1)(\boldsymbol{\alpha}^{(n)} - \boldsymbol{\alpha}^{(n-1)})/t^{(n+1)}$
6: **end for**
7: $\hat{\boldsymbol{\alpha}} \leftarrow \boldsymbol{\alpha}^{(N)}$

Here, $\mathbf{H}^{\dagger}$ denotes the adjoint of the projection operator $\mathbf{H}$, and 'L' denotes the Lipschitz constant of the operator $2\mathbf{H}^{\dagger}\mathbf{H}$.

The function 'F_Dnoise' in Alg. 13-Line 3 solves a de-noising problem defined as:

$$\hat{\mathbf{x}} = \arg\min_{\mathbf{x}\geq 0} \|\mathbf{y} - \mathbf{x}\|^2 + \mu|\mathbf{x}|_{\mathrm{TV}}, \tag{B.1}$$

where $\mu = 2\lambda/L$ and

$$\mathbf{y} = \boldsymbol{\sigma}^{(n)} - \frac{2}{L}\mathbf{H}^{\dagger}(\mathbf{H}\boldsymbol{\sigma}^{(n)} - \tilde{\mathbf{u}}). \tag{B.2}$$

It has been demonstrated that Eqn. (B.1) can be solved efficiently [11, 10], and the pseudocodes are provided in Alg. 14.

Algorithm 14 Solver of the de-noising problem defined by Eqn. (B.1)

Input: $\mathbf{y}$, μ

Output: $\hat{\mathbf{x}}$

$\big[\mathbf{a}^{(1)}, \mathbf{b}^{(1)}, \mathbf{c}^{(1)}\big] \leftarrow \big[\mathbf{0}_{(N_x-1)\times N_y \times N_z}, \mathbf{0}_{N_x\times(N_y-1)\times N_z}, \mathbf{0}_{N_x\times N_y\times(N_z-1)}\big]$
$\big[\mathbf{d}^{(0)}, \mathbf{e}^{(0)}, \mathbf{f}^{(0)}\big] \leftarrow \big[\mathbf{0}_{(N_x-1)\times N_y \times N_z}, \mathbf{0}_{N_x\times(N_y-1)\times N_z}, \mathbf{0}_{N_x\times N_y\times(N_z-1)}\big]$
$t^{(1)} = 1$
for $n = 1$ **to** N **do**
  $\big[\mathbf{d}^{(n)}, \mathbf{e}^{(n)}, \mathbf{f}^{(n)}\big] \leftarrow \mathcal{P}_p\Big\{[\mathbf{a}^{(n)}, \mathbf{b}^{(n)}, \mathbf{c}^{(n)}] + (6\mu)^{-1}\mathcal{P}_l^T\big\{\mathcal{P}_c\{\mathbf{y} - 0.5\mu\mathcal{P}_l\{\mathbf{a}^{(n)}, \mathbf{b}^{(n)}, \mathbf{c}^{(n)}\}\}\big\}\Big\}$
  $t^{(n+1)} \leftarrow 0.5 + 0.5\sqrt{1 + 4(t^{(n)})^2}$
  $\big[\mathbf{a}^{(n+1)}, \mathbf{b}^{(n+1)}, \mathbf{c}^{(n+1)}\big] \leftarrow (t^{(n)} - 1)/t^{(n+1)}\big[\mathbf{d}^{(n)} - \mathbf{d}^{(n-1)}, \mathbf{e}^{(n)} - \mathbf{e}^{(n-1)}, \mathbf{f}^{(n)} - \mathbf{f}^{(n-1)}\big]$
end for
$\hat{\mathbf{x}} \leftarrow \mathcal{P}_c\big\{\mathbf{y} - \lambda\mathcal{P}_l\{\mathbf{d}^{(N)}, \mathbf{e}^{(N)}, \mathbf{f}^{(N)}\}\big\}$

The four operators $\mathcal{P}_l$ $\mathcal{P}_c$, $\mathcal{P}_l^T$ and $\mathcal{P}_p$ in Alg. 14 are defined as follows.

$\mathcal{P}_l : \mathbb{R}^{(N_x-1)\times N_y\times N_z} \times \mathbb{R}^{N_x\times(N_y-1)\times N_z} \times \mathbb{R}^{N_x\times N_y\times(N_z-1)} \rightarrow \mathbb{R}^{N_x\times N_y\times N_z}$**:**

$$\begin{aligned}\big[\mathcal{P}_l\{\mathbf{a},\mathbf{b},\mathbf{c}\}\big]_{n_x,n_y,n_z} &= [\mathbf{a}]_{n_x,n_y,n_z} + [\mathbf{b}]_{n_x,n_y,n_z} + [\mathbf{c}]_{n_x,n_y,n_z} \\ &\quad - [\mathbf{a}]_{n_x-1,n_y,n_z} - [\mathbf{b}]_{n_x,n_y-1,n_z} - [\mathbf{c}]_{n_x,n_y,n_z-1} \\ &\quad \text{for} \quad n_x = 1,\cdots,N_x,\ n_y = 1,\cdots,N_y,\ n_z = 1,\cdots,N_z,\end{aligned} \tag{B.3}$$

where we assume $[\mathbf{a}]_{0,n_y,n_z} = [\mathbf{a}]_{N_x,n_y,n_z} = [\mathbf{b}]_{n_x,0,n_z} = [\mathbf{b}]_{n_x,N_y,n_z} = [\mathbf{c}]_{n_x,n_y,0} = [\mathbf{c}]_{n_x,n_y,N_z} \equiv 0$.

$\mathcal{P}_c : \mathbb{R}^{N_x\times N_y\times N_z} \rightarrow \mathbb{R}^{N_x\times N_y\times N_z}$**:**

$$\big[\mathcal{P}_c\{\mathbf{x}\}\big]_{n_x,n_y,n_z} = \max\big\{0, [\mathbf{x}]_{n_x,n_y,n_z}.\big\} \tag{B.4}$$

$\mathcal{P}_l^T : \mathbb{R}^{N_x \times N_y \times N_z} \to \mathbb{R}^{(N_x-1)\times N_y \times N_z} \times \mathbb{R}^{N_x \times (N_y-1) \times N_z} \times \mathbb{R}^{N_x \times N_y \times (N_z-1)}$**:** If we denote the input and output matrices by $\mathbf{y}$ and $(\mathbf{a}, \mathbf{b}, \mathbf{c})$ respectively, we have

$$\begin{aligned}
[\mathbf{a}]_{n_x,n_y,n_z} =& [\mathbf{y}]_{n_x,n_y,n_z} - [\mathbf{y}]_{n_x+1,n_y,n_z}, \\
& \text{for} \quad n_x = 1, \cdots, N_x - 1, n_y = 1, \cdots, N_y, n_z = 1, \cdots, N_z \\
[\mathbf{b}]_{n_x,n_y,n_z} =& [\mathbf{y}]_{n_x,n_y,n_z} - [\mathbf{y}]_{n_x,n_y+1,n_z}, \\
& \text{for} \quad n_x = 1, \cdots, N_x, n_y = 1, \cdots, N_y - 1, n_z = 1, \cdots, N_z \\
[\mathbf{c}]_{n_x,n_y,n_z} =& [\mathbf{y}]_{n_x,n_y,n_z} - [\mathbf{y}]_{n_x,n_y,n_z+1}, \\
& \text{for} \quad n_x = 1, \cdots, N_x, n_y = 1, \cdots, N_y, n_z = 1, \cdots, N_z - 1.
\end{aligned} \tag{B.5}$$

$\mathcal{P}_p : \mathbb{R}^{(N_x-1)\times N_y \times N_z} \times \mathbb{R}^{N_x \times (N_y-1) \times N_z} \times \mathbb{R}^{N_x \times N_y \times (N_z-1)} \to \mathbb{R}^{(N_x-1)\times N_y \times N_z} \times \mathbb{R}^{N_x \times (N_y-1) \times N_z} \times \mathbb{R}^{N_x \times N_y \times (N_z-1)}$**:** If we denote the input and output matrices by $(\mathbf{a}, \mathbf{b}, \mathbf{c})$ and $(\mathbf{d}, \mathbf{e}, \mathbf{f})$ respectively, we have

$$\begin{aligned}
[\mathbf{d}]_{n_x,n_y,n_z} &= \frac{[\mathbf{a}]_{n_x,n_y,n_z}}{\max\left\{1, \sqrt{[\mathbf{a}]^2_{n_x,n_y,n_z} + [\mathbf{b}]^2_{n_x,n_y,n_z} + [\mathbf{c}]^2_{n_x,n_y,n_z}}\right\}} \\
[\mathbf{e}]_{n_x,n_y,n_z} &= \frac{[\mathbf{b}]_{n_x,n_y,n_z}}{\max\left\{1, \sqrt{[\mathbf{a}]^2_{n_x,n_y,n_z} + [\mathbf{b}]^2_{n_x,n_y,n_z} + [\mathbf{c}]^2_{n_x,n_y,n_z}}\right\}} \\
[\mathbf{f}]_{n_x,n_y,n_z} &= \frac{[\mathbf{c}]_{n_x,n_y,n_z}}{\max\left\{1, \sqrt{[\mathbf{a}]^2_{n_x,n_y,n_z} + [\mathbf{b}]^2_{n_x,n_y,n_z} + [\mathbf{c}]^2_{n_x,n_y,n_z}}\right\}},
\end{aligned} \tag{B.6}$$

where $n_x = 1, \cdots, N_x$, $n_y = 1, \cdots, N_y$, $n_z = 1, \cdots, N_z$, and we assume $[\mathbf{a}]_{0,n_y,n_z} = [\mathbf{a}]_{N_x,n_y,n_z} = [\mathbf{b}]_{n_x,0,n_z} = [\mathbf{b}]_{n_x,N_y,n_z} = [\mathbf{c}]_{n_x,n_y,0} = [\mathbf{c}]_{n_x,n_y,N_z} \equiv 0$.

Appendix C

Derivation of Equation (6.4)

The integrated data function $g(\mathbf{r}^s, t)$ in Eqn. (2.2), evaluated at the q-th transducer and the k-th time instance, can be expressed as:

$$g(\mathbf{r}_q^s, t)\Big|_{t=k\Delta_t} = \int_{|\mathbf{r}_q^s - \mathbf{r}| = kc_0\Delta_t} d\mathbf{r}\, A(\mathbf{r}), \tag{C.1}$$

where $\mathbf{r}_q^s$ denotes the location of the q-th point-like transducer. We defined a local coordinate system, distinguished by a superscript 'tr', centered at the q-th transducer with the z^{tr}-axis pointing to the origin of the global coordinate system as shown in Fig. 6.1-(b). Assuming the object function $A(\mathbf{r})$ is compactly supported in a sphere of radius R, the integral surface is symmetric about the z^{tr}-axis. Thus, the orientations of the x^{tr}- and y^{tr}-axes can be arbitrary within the $z^{\text{tr}} = 0$ plane. Representing the right-hand side of Eqn. (C.1) in the local spherical coordinate system, one obtains

$$g(\mathbf{r}_q^s, t)\Big|_{t=k\Delta_t} = (kc_0\Delta_t)^2 \int_0^{\theta_{\max}^{\text{tr}}} d\theta^{\text{tr}} \sin\theta^{\text{tr}} \int_0^{2\pi} d\phi^{\text{tr}}\, A(kc_0\Delta_t, \theta^{\text{tr}}, \phi^{\text{tr}}), \tag{C.2}$$

where $\theta_{\max}^{\text{tr}}$ is half of the apex angle of the cone that corresponds to the intersectional spherical cap as shown in Fig. 6.1-(b). The polar angle θ^{tr} and the azimuth angle ϕ^{tr} were discretized with intervals $\Delta_{\theta^{\text{tr}}}$ that satisfied

$$kc_0\Delta_t\Delta_{\theta^{\text{tr}}} = kc_0\Delta_t \sin\theta^{\text{tr}}\Delta_{\phi^{\text{tr}}} = \Delta_s. \tag{C.3}$$

Therefore, Eqn. (C.2) can be approximated by

$$g(\mathbf{r}_q^s, t)\Big|_{t=k\Delta_t} \approx \Delta_s^2 \sum_{i=0}^{N_i-1} \sum_{j=0}^{N_j-1} A(kc_0\Delta_t, \theta_i^{\text{tr}}, \phi_j^{\text{tr}}), \tag{C.4}$$

where $N_i = \lfloor \theta_{\max}^{\text{tr}}/\Delta_{\theta^{\text{tr}}} \rfloor$, $N_j = \lfloor 2\pi/\Delta_{\phi^{\text{tr}}} \rfloor$, $\theta_i^{\text{tr}} = i\Delta_{\theta^{\text{tr}}}$, and $\phi_j^{\text{tr}} = j\Delta_{\phi^{\text{tr}}}$. We denoted by $\mathbf{r}_{k,i,j}$ the location in the global coordinate system corresponding to the location vector $(kc_0\Delta_t, \theta_i^{\text{tr}}, \phi_j^{\text{tr}})$ in the local coordinate system in Eqn. (C.4). On substitution from the finite-dimensional representation Eqn. (4.10) into Eqn. (C.4) with $\boldsymbol{\alpha}$ and $\boldsymbol{\psi}_n(\mathbf{r})$ defined by Eqns. (6.1) and (6.2), respectively, we obtained:

$$g(\mathbf{r}_q^s, t)\Big|_{t=k\Delta_t} \approx \Delta_s^2 \sum_{n=0}^{N-1} \left[\boldsymbol{\alpha}_{\text{int}}\right]_n \sum_{i=0}^{N_i-1} \sum_{j=0}^{N_j-1} \psi_n^{\text{int}}(\mathbf{r}_{k,i,j}) \equiv \left[\mathbf{g}\right]_{qK+k}. \tag{C.5}$$

References

[1] M.A Anastasio, J. Zhang, X. Pan, Y Zou, G. Keng, and L.V Wang. Half-time image reconstruction in thermoacoustic tomography. *IEEE Transactions on Medical Imaging*, 24:199–210, 2005.

[2] M.A. Anastasio, Jin Zhang, E.Y. Sidky, Yu Zou, D. Xia, and Xiaochuan Pan. Feasibility of half-data image reconstruction in 3-D reflectivity tomography with a spherical aperture. *Medical Imaging, IEEE Transactions on*, 24(9):1100 –1112, sept. 2005.

[3] Mark A. Anastasio, Kun Wang, Jin Zhang, Gabe A. Kruger, Daniel Reinecke, and Robert A. Kruger. Improving limited-view reconstruction in photoacoustic tomography by incorporating a priori boundary information. volume 6856, page 68561B. SPIE, 2008.

[4] M. A Anastasio and J. Zhang. Image reconstruction in photoacoustic tomography with truncated cylindrical measurement apertures. In *Proceedings of the SPIE Conference*, volume 6086, page 36, 2006.

[5] M. A Anastasio, J. Zhang, D. Modgil, and P. La Riviere. Application of inverse source concepts to photoacoustic tomography. *Inverse Problems*, 23:S21–S35, 2007.

[6] Valeri G. Andreev, Alexander A. Karabutov, Anatoliy E. Ponomaryov, and Alexander A. Oraevsky. Detection of optoacoustic transients with a rectangular transducer of finite dimensions. volume 4618, pages 153–162. SPIE, 2002.

[7] O Axelsson. *Iterative Solution Methods*. Cambridge University Press, Cambridge, UK, 1994.

[8] Sylvain Ballandras, Mikael Wilm, Paul-Francis Edoa, Abdelaziz Soufyane, Vincent Laude, William Steichen, and Raphael Lardat. Finite-element analysis of periodic piezoelectric transducers. *Journal of Applied Physics*, 93(1):702–711, 2003.

[9] H. Barrett and K. Myers. *Foundations of Image Science*. Wiley Series in Pure and Applied Optics, 2004.

[10] A. Beck and M. Teboulle. Fast gradient-based algorithms for constrained total variation image denoising and deblurring problems. *Image Processing, IEEE Transactions on*, 18(11):2419 –2434, nov. 2009.

[11] Amir Beck and Marc Teboulle. A fast iterative shrinkage-thresholding algorithm for linear inverse problems. *SIAM J. Img. Sci.*, 2(1):183–202, March 2009.

[12] Junguo Bian, Jeffrey H Siewerdsen, Xiao Han, Emil Y Sidky, Jerry L Prince, Charles A Pelizzari, and Xiaochuan Pan. Evaluation of sparse-view reconstruction from flat-panel-detector cone-beam ct. *Physics in Medicine and Biology*, 55(22):6575, 2010.

[13] Stephen Boyd, Neal Parikh, Eric Chu, Borja Peleato, and Jonathan Eckstein. Distributed optimization and statistical learning via the alternating direction method of multipliers. *Found. Trends Mach. Learn.*, 3(1):1–122, January 2011.

[14] Hans-Peter Brecht, Richard Su, Matt Fronheiser, Sergey A. Ermilov, Andre Conjusteau, Anton Liopo, Massoud Motamedi, and Alexander A. Oraevsky. Optoacoustic 3d whole-body tomography: experiments in nude mice. volume 7177, page 71770E. SPIE, 2009.

[15] Hans-Peter Brecht, Richard Su, Matthew Fronheiser, Sergey A. Ermilov, Andre Conjusteau, and Alexander A. Oraevsky. Whole-body three-dimensional optoacoustic tomography system for small animals. *Journal of Biomedical Optics*, 14(6):064007, 2009.

[16] Shuhui Bu, Zhenbao Liu, T. Shiina, K. Kondo, M. Yamakawa, K. Fukutani, Y. Someda, and Y. Asao. Model-based reconstruction integrated with fluence compensation for photoacoustic tomography. *Biomedical Engineering, IEEE Transactions on*, 59(5):1354 –1363, may 2012.

[17] Andreas Buehler, Amir Rosenthal, Thomas Jetzfellner, Alexander Dima, Daniel Razansky, and Vasilis Ntziachristos. Model-based optoacoustic inversions with incomplete projection data. *Medical Physics*, 38(3):1694–1704, 2011.

[18] P. Burgholzer, C. Hofer, G. Paltauf, M. Haltmeier, and O. Scherzer. Thermoacoustic tomography with integrating area and line detectors. *Ultrasonics, Ferroelectrics and Frequency Control, IEEE Transactions on*, 52(9):1577 –1583, sept. 2005.

[19] Peter Burgholzer, Gebhard J. Matt, Markus Haltmeier, and Günther Paltauf. Exact and approximative imaging methods for photoacoustic tomography using an arbitrary detection surface. *Phys. Rev. E*, 75:046706, Apr 2007.

[20] Cheng-Ying Chou, Yi-Yen Chuo, Yukai Hung, and Weichung Wang. A fast forward projection using multithreads for multirays on GPUs in medical image reconstruction. *Medical Physics*, 38(7):4052–4065, 2011.

[21] J. F. Claerbout. *Earth Sounding Analysis: Processing Versus Inversion*. Blackwell Scientific Publications, Cambridge, MA, 1992.

[22] Andre Conjusteau, Sergey A. Ermilov, Richard Su, Hans-Peter Brecht, Matthew P. Fronheiser, and Alexander A. Oraevsky. Measurement of the spectral directivity of optoacoustic and ultrasonic transducers with a laser ultrasonic source. *Review of Scientific Instruments*, 80(9):093708 –093708–5, sep 2009.

[23] B T Cox, S R Arridge, and P C Beard. Photoacoustic tomography with a limited-aperture planar sensor and a reverberant cavity. *Inverse Problems*, 23(6):S95, 2007.

[24] B. T. Cox and P. C. Beard. Fast calculation of pulsed photoacoustic fields in fluids using k-space methods. *The Journal of the Acoustical Society of America*, 117(6):3616–3627, 2005.

[25] B. T. Cox and B. E. Treeby. Effect of sensor directionality on photoacoustic imaging: a study using the k-wave toolbox. volume 7564, page 75640I. SPIE, 2010.

[26] Peter Elbau, Otmar Scherzer, and Rainer Schulze. Reconstruction formulas for photoacoustic sectional imaging. *Inverse Problems*, 28(4):045004, 2012.

[27] Pinhas Ephrat, Lynn Keenliside, Adam Seabrook, Frank S. Prato, and Jeffrey J. L. Carson. Three-dimensional photoacoustic imaging by sparse-array detection and iterative image reconstruction. *Journal of Biomedical Optics*, 13(5):054052, 2008.

[28] Pinhas Ephrat, Lynn Keenliside, Adam Seabrook, Frank S. Prato, and Jeffrey J. L. Carson. Three-dimensional photoacoustic imaging by sparse-array detection and iterative image reconstruction. *Journal of Biomedical Optics*, 13(5):054052, 2008.

[29] Sergey A. Ermilov, Matthew P. Fronheiser, Hans-Peter Brecht, Richard Su, Andre Conjusteau, Ketan Mehta, Pamela Otto, and Alexander A. Oraevsky. Development of laser optoacoustic and ultrasonic imaging system for breast cancer utilizing handheld array probes. volume 7177, page 717703. SPIE, 2009.

[30] R. O Esenaliev, A. A Karabutov, and A. A Oraevsky. Sensitivity of laser opto-acoustic imaging in detection of small deeply embedded tumors. *IEEE Journal of Selected Topics in Quantum Electronics*, 5:981–988, 1999.

[31] J A Fessler. Penalized weighted least-squares reconstruction for positron emission tomography. *IEEE Transactions on Medical Imaging*, 13:290–300, 1994.

[32] J A Fessler and W. L. Rogers. Spatial resolution properties of penalized-likelihood image reconstruction methods: Space-invariant tomographs. *IEEE Transactions on Image Processing*, 5(9):1346–1358, 1996.

[33] J.A. Fessler and S.D. Booth. Conjugate-gradient preconditioning methods for shift-variant PET image reconstruction. *Image Processing, IEEE Transactions on*, 8(5):688 –699, may 1999.

[34] D. Finch, S. Patch, and Rakesh. Determining a function from its mean values over a family of spheres. *SIAM Journal of Mathematical Analysis*, 35:1213–1240, 2004.

[35] David Finch, Markus Haltmeier, and Rakesh. Inversion of spherical means and the wave equation in even dimensions. *SIAM Journal on Applied Mathematics*, 68(2):392–412, 2007.

[36] Daniel Gallego and Horacio Lamela. High-sensitivity ultrasound interferometric single-mode polymer optical fiber sensors for biomedical applications. *Opt. Lett.*, 34(12):1807–1809, Jun 2009.

[37] Zijian Guo, Changhui Li, Liang Song, and Lihong V. Wang. Compressed sensing in photoacoustic tomography in vivo. *Journal of Biomedical Optics*, 15(2):021311, 2010.

[38] M Haltmeier, O Scherzer, P Burgholzer, and G Paltauf. Thermoacoustic computed tomography with large planar receivers. *Inverse Problems*, 20(5):1663–1673, 2004.

[39] Xiao Han, Junguo Bian, D.R. Eaker, T.L. Kline, E.Y. Sidky, E.L. Ritman, and Xiaochuan Pan. Algorithm-enabled low-dose micro-ct imaging. *Medical Imaging, IEEE Transactions on*, 30(3):606 –620, march 2011.

[40] Gerald R. Harris. Review of transient field theory for a baffled planar piston. *The Journal of the Acoustical Society of America*, 70(1):10–20, 1981.

[41] Yulia Hristova, Peter Kuchment, and Linh Nguyen. Reconstruction and time reversal in thermoacoustic tomography in acoustically homogeneous and inhomogeneous media. *Inverse Problems*, 24(5):055006, 2008.

[42] Chao Huang, Liming Nie, Robert W. Schoonover, Zijian Guo, Carsten O. Schirra, Mark A. Anastasio, and Lihong V. Wang. Aberration correction for transcranial photoacoustic tomography of primates employing adjunct image data. *Journal of Biomedical Optics*, 17(6):066016, 2012.

[43] Chao Huang, Liming Nie, Robert W. Schoonover, Lihong V. Wang, and Mark A. Anastasio. Photoacoustic computed tomography correcting for heterogeneity and attenuation. *Journal of Biomedical Optics*, 17(6):061211, 2012.

[44] Chao Huang, Alexander A. Oraevsky, and Mark A. Anastasio. Investigation of limited-view image reconstruction in optoacoustic tomography employing a priori structural information. volume 7800, page 780004. SPIE, 2010.

[45] J.A. Jensen and N.B. Svendsen. Calculation of pressure fields from arbitrarily shaped, apodized, and excited ultrasound transducers. *Ultrasonics, Ferroelectrics and Frequency Control, IEEE Transactions on*, 39(2):262 –267, mar 1992.

[46] A C Kak and M Slaney. *Principles of Computerized Tomographic Imaging*. IEEE Press, 1988.

[47] Tatiana D. Khokhlova, Ivan M. Pelivanov, Victor V. Kozhushko, Alexei N. Zharinov, Vladimir S. Solomatin, and Alexander A. Karabutov. Optoacoustic imaging of absorbing objects in a turbid medium: ultimate sensitivity and application to breast cancer diagnostics. *Appl. Opt.*, 46(2):262–272, 2007.

[48] K P. Köstli and P. C Beard. Two-dimensional photoacoustic imaging by use of fourier-transform image reconstruction and a detector with an anisotropic response. *Appl. Opt.*, 42(10):1899–1908, 2003.

[49] R. Krimholtz, D.A. Leedom, and G.L. Matthaei. New equivalent circuits for elementary piezoelectric transducers. *Electronics Letters*, 6(13):398 –399, 25 1970.

[50] R. Kruger, P. Liu, R. Fang, and C. Appledorn. Photoacoustic ultrasound (PAUS) reconstruction tomography. *Medical Physics*, 22:1605–1609, 1995.

[51] R. Kruger, D. Reinecke, and G. Kruger. Thermoacoustic computed tomography- technical considerations. *Medical Physics*, 26:1832–1837, 1999.

[52] Robert A. Kruger, Richard B. Lam, Daniel R. Reinecke, Stephen P. Del Rio, and Ryan P. Doyle. Photoacoustic angiography of the breast. *Medical Physics*, 37(11):6096–6100, 2010.

[53] Robert A. Kruger, Jr. William L. Kiser, Daniel R. Reinecke, and Gabe A. Kruger. Thermoacoustic computed tomography using a conventional linear transducer array. *Medical Physics*, 30(5):856–860, 2003.

[54] G. Ku, B. D Fornage, X. Jin, M. Xu, K. K Hunt, and L. V Wang. Thermoacoustic and photoacoustic tomography of thick biological tissues toward breast imaging. *Technology in Cancer Research and Treatment*, 4:559–566, 2005.

[55] L A Kunyansky. Explicit inversion formulae for the spherical mean Radon transform. *Inverse Problems*, 23:373–383, 2007.

[56] L A Kunyansky. Fast reconstruction algorithms for the thermoacoustic tomography in certain domains with cylindrical or spherical symmetries. *Inverse Problems and Imaging*, 6(1):111–131, 2012.

[57] R. Lerch. Finite element analysis of piezoelectric transducers. In *Ultrasonics Symposium, 1988. Proceedings., IEEE 1988*, pages 643 –654 vol.2, oct 1988.

[58] R M Lewitt. Alternatives to voxels for image representation in iterative reconstruction algorithms. *Physics in Medicine and Biology*, 37(3):705–716, 1992.

[59] Changhui Li and Lihong V. Wang. High-numerical-aperture-based virtual point detectors for photoacoustic tomography. *Applied Physics Letters*, 93(3):033902, 2008.

[60] Meng-Lin Li and Chung-Chih Cheng. Reconstruction of photoacoustic tomography with finite-aperture detectors: deconvolution of the spatial impulse response. volume 7564, page 75642S. SPIE, 2010.

[61] Meng-Lin Li, Hao F. Zhang, Konstantin Maslov, George Stoica, and Lihong V. Wang. Improved in vivo photoacoustic microscopy based on a virtual-detector concept. *Opt. Lett.*, 31(4):474–476, 2006.

[62] E. Lindholm, J. Nickolls, S. Oberman, and J. Montrym. Nvidia tesla: A unified graphics and computing architecture. *Micro, IEEE*, 28(2):39 –55, march-april 2008.

[63] J. C. Lockwood and J. G. Willette. High-speed method for computing the exact solution for the pressure variations in the nearfield of a baffled piston. *The Journal of the Acoustical Society of America*, 53(3):735–741, 1973.

[64] S. Manohar, R. G. H. Willemink, F. van der Heijden, C. H. Slump, and T. G. van Leeuwen. Concomitant speed-of-sound tomography in photoacoustic imaging. *Applied Physics Letters*, 91:131911, 2007.

[65] K Maslov and L V. Wang. Photoacoustic imaging of biological tissue with intensity-modulated continuous-wave laser. *Journal of Biomedical Optics*, 13(2):024006, 2008.

[66] Konstantin Maslov, Gheorghe Stoica, and Lihong V. Wang. In vivo dark-field reflection-mode photoacoustic microscopy. *Opt. Lett.*, 30(6):625–627, Mar 2005.

[67] W. P. Mason. *Electromechanical Transducers and Wave Filters*. D. Van Nostrand Company, Inc., Princeton, N.J., 1984.

[68] A. A. Oraevsky and A. A. Karabutov. Optoacoustic tomography. In Tuan Vo-Dinh, editor, *Biomedical Photonics Handbook*. CRC Press LLC, 2003.

[69] M. N. Wernick and J. N. Aarsvold. *Emission Tomography, the Fundamentals of PET and SPECT*. Elsevier Academic Press, San Diego, California, 2004.

[70] Xu M. and L. V. Wang. Analytic explanation of spatial resolution related to bandwidth and detector aperture size in thermoacoustic or photoacoustic reconstruction. *Physical Review E*, 67(056605), 2003.

[71] Jing Meng, Lihong V. Wang, Leslie Ying, Dong Liang, and Liang Song. Compressed-sensing photoacoustic computed tomography in vivo with partially known support. *Opt. Express*, 20(15):16510–16523, Jul 2012.

[72] Dimple Modgil, Mark A. Anastasio, and Patrick J. La Rivire. Image reconstruction in photoacoustic tomography with variable speed of sound using a higher-order geometrical acoustics approximation. *Journal of Biomedical Optics*, 15(2):021308–021308–9, 2010.

[73] K. W. Morton and D. F. Mayers. *Numerical Solution of Partial Differential Equations: An Introduction*. Cambridge University Press, New York, NY, USA, 2005.

[74] Stephen Norton. Reconstruction of a two-dimensional reflecting medium over a circular domain: Exact solution. *Journal of the Acoustical Society of America*, 67(4):1266–1273, 1980.

[75] Stephen Norton and Melvin Linzer. Ultrasonic reflectivity imaging in three dimensions: Exact inverse scattering solutions for plane, cylindrical, and spherical apertures. *IEEE Transactions on Biomedical Engineering*, 28:202–220, 1981.

[76] NVIDIA. *NVIDIA CUDA Programming Guide 2.0*. 2008.

[77] Morten Wollert Nygren. *Finite Element Modeling of Piezoelectric Ultrasonic Transducers*. Institutt for elektronikk og telekommunikasjon, 2011.

[78] Yusuke Okitsu, Fumihiko Ino, and Kenichi Hagihara. High-performance cone beam reconstruction using CUDA compatible GPUs. *Parallel Computing*, 36(23):129 – 141, 2010.

[79] A. A Oraevsky, S. L Jacques, and F. K Tittel. Measurement of tissue optical properties by time-resolved detection of laser-induced transient stress. *Applied Optics*, 36:402–415, 1997.

[80] A. A Oraevsky and A. A Karabutov. Ultimate sensitivity of time-resolved optoacoustic detection. volume 3916, pages 228–239. SPIE, 2000.

[81] G. Paltauf, R. Nuster, and P. Burgholzer. Characterization of integrating ultrasound detectors for photoacoustic tomography. *Journal of Applied Physics*, 105(10):102026, 2009.

[82] G. Paltauf and H. Schmidt-Kloiber. Measurement of laser-induced acoustic waves with a calibrated optical transducer. *Journal of Applied Physics*, 82(4):1525–1531, 1997.

[83] G. Paltauf, H. Schmidt-Kloiber, and H. Guss. Light distribution measurements in absorbing materials by optical detection of laser-induced stress waves. *Applied Physics Letters*, 69(11):1526–1528, 1996.

[84] G. Paltauf, J. A. Viator, S. A. Prahl, and S. L. Jacques. Iterative reconstruction algorithm for optoacoustic imaging. *The Journal of the Acoustical Society of America*, 112(4):1536–1544, 2002.

[85] Guenther Paltauf, Robert Nuster, Markus Haltmeier, and Peter Burgholzer. Photoacoustic tomography using a mach-zehnder interferometer as an acoustic line detector. *Appl. Opt.*, 46(16):3352–3358, Jun 2007.

[86] X. Pan, Y. Zou, and M. A Anastasio. Data redundancy and reduced-scan reconstruction in reflectivity tomography. *IEEE Transactions on Image Processing*, 12:784–795, 2003.

[87] Xiaochuan Pan, Emil Y Sidky, and Michael Vannier. Why do commercial CT scanners still employ traditional, filtered back-projection for image reconstruction? *Inverse Problems*, 25(12):123009, 2009.

[88] B. Piwakowski and K. Sbai. A new approach to calculate the field radiated from arbitrarily structured transducer arrays. *Ultrasonics, Ferroelectrics and Frequency Control, IEEE Transactions on*, 46(2):422 –440, mar 1999.

[89] J. Provost and F. Lesage. The application of compressed sensing for photo-acoustic tomography. *Medical Imaging, IEEE Transactions on*, 28(4):585 –594, april 2009.

[90] M. Redwood. Transient performance of a piezoelectric transducer. *The Journal of the Acoustical Society of America*, 33(4):527–536, 1961.

[91] D. Robinson, S. Lees, and L. Bess. Near field transient radiation patterns for circular pistons. *Acoustics, Speech and Signal Processing, IEEE Transactions on*, 22(6):395 – 403, dec 1974.

[92] A. Rosenthal, D. Razansky, and V. Ntziachristos. Fast semi-analytical model-based acoustic inversion for quantitative optoacoustic tomography. *Medical Imaging, IEEE Transactions on*, 29(6):1275 –1285, june 2010.

[93] Antoine Rosset, Luca Spadola, and Osman Ratib. Osirix: An open-source software for navigating in multidimensional dicom images. *J. Digital Imaging*, 17(3):205–216, 2004.

[94] S. M. Akramus Salehin and Thushara D. Abhayapala. Frequency-radial duality based photoacoustic image reconstruction. *The Journal of the Acoustical Society of America*, 132(1):150–161, 2012.

[95] Robert W. Schoonover and Mark A. Anastasio. Compensation of shear waves in photoacoustic tomography with layered acoustic media. *J. Opt. Soc. Am. A*, 28(10):2091–2099, Oct 2011.

[96] Jonathan R Shewchuk. An introduction to the conjugate gradient method without the agonizing pain. Technical report, Pittsburgh, PA, USA, 1994.

[97] Peter R. Stepanishen. Transient radiation from pistons in an infinite planar baffle. *The Journal of the Acoustical Society of America*, 49(5B):1629–1638, 1971.

[98] S.S. Stone, J.P. Haldar, S.C. Tsao, W. m.W. Hwu, B.P. Sutton, and Z.-P. Liang. Accelerating advanced MRI reconstructions on GPUs. *Journal of Parallel and Distributed Computing*, 68(10):1307 – 1318, 2008.

[99] Sergey Telenkov and Andreas Mandelis. Signal-to-noise analysis of biomedical photoacoustic measurements in time and frequency domains. *Review of Scientific Instruments*, 81(12):124901, 2010.

[100] Tat-Jin Teo. An improved approximation for the spatial impulse response of a rectangular transducer. *Ultrasonics, Ferroelectrics and Frequency Control, IEEE Transactions on*, 45(1):76 –83, jan. 1998.

[101] Bradley E. Treeby and B. T. Cox. k-wave: Matlab toolbox for the simulation and reconstruction of photoacoustic wave fields. *Journal of Biomedical Optics*, 15(2):021314, 2010.

[102] G. E. Tupholme. Generation of acoustic pulses by baffled plane pistons. *Mathematika*, 16(02):209–224, 1969.

[103] David C. Wang, Robert Joseph Tamburo, and George D. Stetten. Cumulative gaussian curve fitter for boundary parameterization. *Technical report in special MICCAI 2005 Workshop on Open-Source Software issue of The Insight Journal*, August 2005.

[104] K. Wang and M. A. Anastasio. Photoacoustic and thermoacoustic tomography: image formation principles. In Otmar Scherzer, editor, *Handbook of Mathematical Methods in Imaging*. Springer, 2011.

[105] K. Wang, S. A. Ermilov, R. Su, H.-P. Brecht, A. A. Oraevsky, and M. A. Anastasio. An imaging model incorporating ultrasonic transducer properties for three-dimensional optoacoustic tomography. *Medical Imaging, IEEE Transactions on*, 30(2):203 –214, feb. 2011.

[106] Kun Wang and Mark A Anastasio. A simple fourier transform-based reconstruction formula for photoacoustic computed tomography with a circular or spherical measurement geometry. *Physics in Medicine and Biology*, 57(23):N493, 2012.

[107] Kun Wang, Mark A. Anastasio, Sergey A. Ermilov, Hans-Peter Brecht, Richard Su, and Alexander A. Oraevsky. Compensation for transducer effects in optoacoustic tomography. volume 7564, pages 75640P–75640P–6. SPIE, 2010.

[108] Kun Wang, Emil Y. Sidky, Mark A. Anastasio, Alexander A. Oraevsky, and Xiaochuan Pan. Limited data image reconstruction in optoacoustic tomography by constrained total variation minimization. volume 7899, page 78993U. SPIE, 2011.

[109] Kun Wang, Richard Su, Alexander A. Oraevsky, and Mark A. Anastasio. Investigation of iterative image reconstruction in optoacoustic tomography. volume 8223, page 82231Y. SPIE, 2012.

[110] Kun Wang, Richard Su, Alexander A Oraevsky, and Mark A Anastasio. Investigation of iterative image reconstruction in three-dimensional optoacoustic tomography. *Physics in Medicine and Biology*, 57(17):5399, 2012.

[111] Kun Wang, Richard Su, Alexander A. Oraevsky, and Mark A. Anastasio. Sparsity regularized data-space restoration in optoacoustic tomography. pages 822322–822322–7, 2012.

[112] L. V Wang. Tutorial on photoacoustic microscopy and computed tomography. *IEEE Journal of Selected Topics in Quantum Electronics*, 14:171–179, 2008.

[113] L. V Wang and H-I Wu. *Biomedical Optics, Principles and Imaging*. Wiley, Hoboken, N.J., 2007.

[114] L V Wang, X M Zhao, H. T Sun, and G Ku. Microwave-induced acoustic imaging of biological tissues. *Review of Scientific Instruments*, 70:3744–3748, 1999.

[115] X. WANG. Noninvasive laser-induced photoacoustic tomography for structural and functional in vivo imaging of the brain. *Nature Biotechnol.*, 21:803–806, 2003.

[116] J. P. Weight. Ultrasonic beam structures in fluid media. *The Journal of the Acoustical Society of America*, 76(4):1184–1191, 1984.

[117] M. Willatzen. Ultrasound transducer modeling-general theory and applications to ultrasound reciprocal systems. *Ultrasonics, Ferroelectrics and Frequency Control, IEEE Transactions on*, 48(1):100 –112, jan. 2001.

[118] Ping Wu and T. Stepinski. Spatial impulse response method for predicting pulse-echo fields from a linear array with cylindrically concave surface. *Ultrasonics, Ferroelectrics and Frequency Control, IEEE Transactions on*, 46(5):1283 –1297, sept. 1999.

[119] M. Xu and L. V. Wang. Photoacoustic imaging in biomedicine. *Review of Scientific Instruments*, 77(041101), 2006.

[120] M. Xu and L.V Wang. Time-domain reconstruction for thermoacoustic tomography in a spherical geometry. *IEEE Transactions on Medical Imaging*, 21:814–822, 2002.

[121] Y. Xu, D. Feng, and L. V. Wang. Exact frequency-domain reconstruction for thermoacoustic tomography: I. Planar geometry. *IEEE Transactions on Medical Imaging*, 21:823–828, 2002.

[122] Y Xu and L. V. Wang. Universal back-projection algorithm for photoacoustic computed tomography. *Physical Review E*, 71(016706), 2005.

[123] Zhun Xu, Changhui Li, and Lihong V. Wang. Photoacoustic tomography of water in phantoms and tissue. *Journal of Biomedical Optics*, 15(3):036019, 2010.

[124] Zhun Xu, Quing Zhu, and Lihong V. Wang. In vivo photoacoustic tomography of mouse cerebral edema induced by cold injury. *Journal of Biomedical Optics*, 16(6):066020, 2011.

[125] Xinmai Yang, Meng-Lin Li, and Lihong V. Wang. Ring-based ultrasonic virtual point detector with applications to photoacoustic tomography. *Applied Physics Letters*, 90(25):251103, 2007.

[126] Lei Yao and Huabei Jiang. Enhancing finite element-based photoacoustic tomography using total variation minimization. *Appl. Opt.*, 50(25):5031–5041, Sep 2011.

[127] Zhen Yuan and Huabei Jiang. Three-dimensional finite-element-based photoacoustic tomography: Reconstruction algorithm and simulations. *Medical Physics*, 34(2):538–546, 2007.

[128] Gerhard Zangerl, Otmar Scherzer, and Markus Haltmeier. Exact series reconstruction in photoacoustic tomography with circular integrating detectors. *Commun. Math. Sci.*, 7(3):665–678, 2009.

[129] G.L. Zeng and G.T. Gullberg. Unmatched projector/backprojector pairs in an iterative reconstruction algorithm. *Medical Imaging, IEEE Transactions on*, 19(5):548 –555, may 2000.

[130] Y. Zeng, D. Xing, Y. Wang, B. Yin, and Q. Chen. Photoacoustic and ultrasonic coimage with a linear transducer array. *Optics Letters*, 29:1760–1762, 2004.

[131] Hao F. Zhang, Konstantin Maslov, Gheorghe Stoica, and Lihong V. Wang. Functional photoacoustic microscopy for high-resolution and noninvasive in vivo imaging. *Nature Biotechnology*, 24(7):848–851, June 2006.

[132] J. Zhang, M. A Anastasio, X. Pan, and L. V Wang. Weighted expectation maximization reconstruction algorithms for thermoacoustic tomography. *IEEE transactions on medical imaging*, 24:817–820, 2005.

[133] Jin Zhang, M.A. Anastasio, P.J. La Riviere, and L.V. Wang. Effects of different imaging models on least-squares image reconstruction accuracy in photoacoustic tomography. *Medical Imaging, IEEE Transactions on*, 28(11):1781 –1790, nov. 2009.

[134] Xing Zhao, Jing-Jing Hu, and Peng Zhang. GPU-based 3D cone-beam CT image reconstruction for large data volume. *Journal of Biomedical Imaging*, 2009:8:1–8:8, January 2009.

Photoacoustic Computed Tomography, Wang, Ph.D. 2012